Development of microneedles on flexible skin patch with functional components for transdermal drug delivery applications

Hao Wang

(*B.Eng, UESTC***)**

A THESIS SUBMITTED

FOR THE DEGREE OF DOCTOR OF PHILOSOPHY

DEPARTMENT OF ELECTRICAL AND COMPUTER ENGINEERING

NATIONAL UNIVERSITY OF SINGAPORE

2015

DECLARATION

I hereby declare that this thesis is my original work and it has been written by me in its entirety. I have duly acknowledged all the sources of information which have been used in the thesis.

This thesis has also not been submitted for any degree in any university previously.

_____

Wang Hao

15 Jan 2016

Acknowledgement

First and foremost, I would like to express my sincere gratitude to my supervisor Prof. Chengkuo Lee for his consistent supports, encouragement and instructions during my Ph.D study. I appreciate all his contributions of time, ideas and funding to make my Ph.D experience in NUS passionate and fruitful. The concentration and enthusiasm he has inspired me to become a better researcher in the last four years. Without his insightful enlightenment, I would not be able to work through all the challenges in this dissertation.

Besides, I would like to thank Prof. Giorgia Pastorin for their valuable suggestions on the animal testing of our devices. Their generous contribution helped me to explore unknown scientific problems beyond the developed engineering technologies.

Meanwhile, I would like to thank Prof. Weileun Fang, National Tsing Hua University, for the preparation of CNTs sample. His generous contribution helped me explore the application of CNTs in microneedles.

In addition, I must express my sincere gratitude to all my colleagues and friends in CICFAR lab: Mr. Xiang Zhuolin, Dr. Songsong Zhang, Prof. Huicong Liu, Dr. Liang Lou, Dr. Kah How Koh, Dr. Bo Li, Dr. Nan Wang, Dr. You Qian, Dr. Woon Soon Bo, Dr. Huchuan Zhou, Mr. Pitchappa Prakash, Mr. Chongpei Ho, Mr. Lokesh Dhakar, Mr. Tao Wang, Mr. Sanghoon Lee, Mr. Qiongfeng Shi, Mr. Dihan Hasan, Miss. Nan Chen, Miss. Jiahui Wang, Miss. Karen Shih and so on. I would also like to thank Mrs. Chiow Mooi Ho and Mr. Chee Keong Koo for their continuous technical supports.

Last but not the least, I would like to express my genuine appreciation to my family. Their selfless love and unconditional support encouraged me all the time in my Ph.D study. I especially want to thank my mother, a housewife who has no idea about research, but teaches me optimism and persistence.

Contents

Summary

This work aims developing different kinds of microneedles with various configurations and functions for transdermal drug delivery applications. Although the microneedle technology has been developed for decades, limited by the process to realize the 3D sharp tip which is critical for skin penetration, it is not easy to merge microneedle technique with other functional components and systems to achieve more complex functions. Most of the studies only focus on changing the materials and geometries, evaluating the performance and finding new applications. Here we developed a very unique technology called drawing lithography for the assembly of SU-8 and maltose sharp tips at the final step of the fabrication process, which is compatible with most of the conventional thin film technology and allows us to explore more possibilities about integrating other functional components and sophisticated system with microneedles. A novel Carbon Nanotubes (CNTs) filter, which can be used for selective transport of bio-molecules, is integrated within the microneedles. Thus, haemagglutinin, single-stranded DNA, glucose and insulin can be selectively delivered depending on their different physical dimensions, shapes and polarities by controlling the pressure and electric bias applied. We also integrated microneedles with a complex system to make a self-powered, flexible microneedle skin patch which is suitable for self-administrated insulin delivery. A pneumatic pump and check-valves are designed for manually controlled drug loading and delivery. In order to have a precise dose control required by insulin delivery, a delivery volume sensor based on triboelectric mechanism is designed and optimized. For powering other functional components to be integrated in the future, a low cost power source, which leverages the stacked layer triboelectric energy harvester design, is characterized to achieve 33μw output power. Moreover, in order to make the device truly wearable, dry adhesive technique is further applied to make the device able to be attached onto any part of the body.

List of Figures

List of tables

List of Acronyms

T_g	Glass transition temperature
T_m	Melting temperature
V	Output voltage of Triboelectric energy harvester
S	Contact surface area of Triboelectric energy harvester
$E_{dielectric}$	Electric field though the dielectric layer
E_{air}	Electric field though the spacing between the top surface of TEH and contact surface
d	Thickness of the dielectric layer
R_{opt}	Inner impedance of the Triboelectric energy harvester
d_0	Thickness of the PDMS layer
x_{max}	Maximum height to be lifted up for TEH patch
v	Speed of the TEH to be lifted up
ε_0	Dielectric constant of air

List of Symbols

MEMS	Microelectromechanical systems
CNTs	Carbon Nanotubes
MN	Microneedles
PDMS	Polydimethylsiloxane
3D	Three-dimensional
PET	Polyethylene Terephthalate
FITC	Fluorescein isothiocyanate
DI	Deionized
Al	Aluminium
PBS	Phosphate buffered saline
SC	Stratum cornuem
NaCl	Sodium Chloride
LCD	Liquid-crystal display
TEH	Triboelectric energy harvester
LoC	Lab on a chip
ss-DNA	Single stranded DNA
PLA	Polylactic acid
PMMA	Polymethylmeth-acrylate
HEM	Hybrid electro-microneedle
UHAR	Ultra-high aspect ratio

Chapter 1 Introduction of microneedle

Drug delivery research has extensively pursed on how to transport proteins, DNA, genes, antibodies and vaccines efficiently and safely to human bodies in recent years. The conventional drug delivery approaches, such as oral administration and hypodermic injection, have their own limitations because a drug may be inactive through phase I metabolism during oral delivery [1], while the hypodermic injection requires trained personnel [2]. In order to overcome these drawbacks, transdermal drug delivery has been taken as a safe, easily accessible and patient friendly approach [3]. The normal biomolecules, however, cannot passively diffuse through the dermal layers of skin due to their unfavorable hydrophilicity and macro size [4]. With the help of microneedles which can create microchannels on the skin surface by penetrating the outmost layer, i.e. *stratum cornuem* (SC), biomolecules can permeate into the tissue under the skin locally [5]. Since these microneedles are only a few hundred micrometers in length, the penetration depth is superficial enough not to touch nerve receptors in the lower reticular dermis, which leads the whole administration to be painless [6]. It is promising that this microneedle-based transdermal delivery approach will offer a self-management, patient-friendly and efficient administration route for drug delivery.

Since the first papers were published on drug delivery using microneedles in the late 1990's, research activity has grown exponentially (**Figure 1.1**), which has led to published clinical trials, approved products and an active community of academic and industry researchers in the field today. [7]

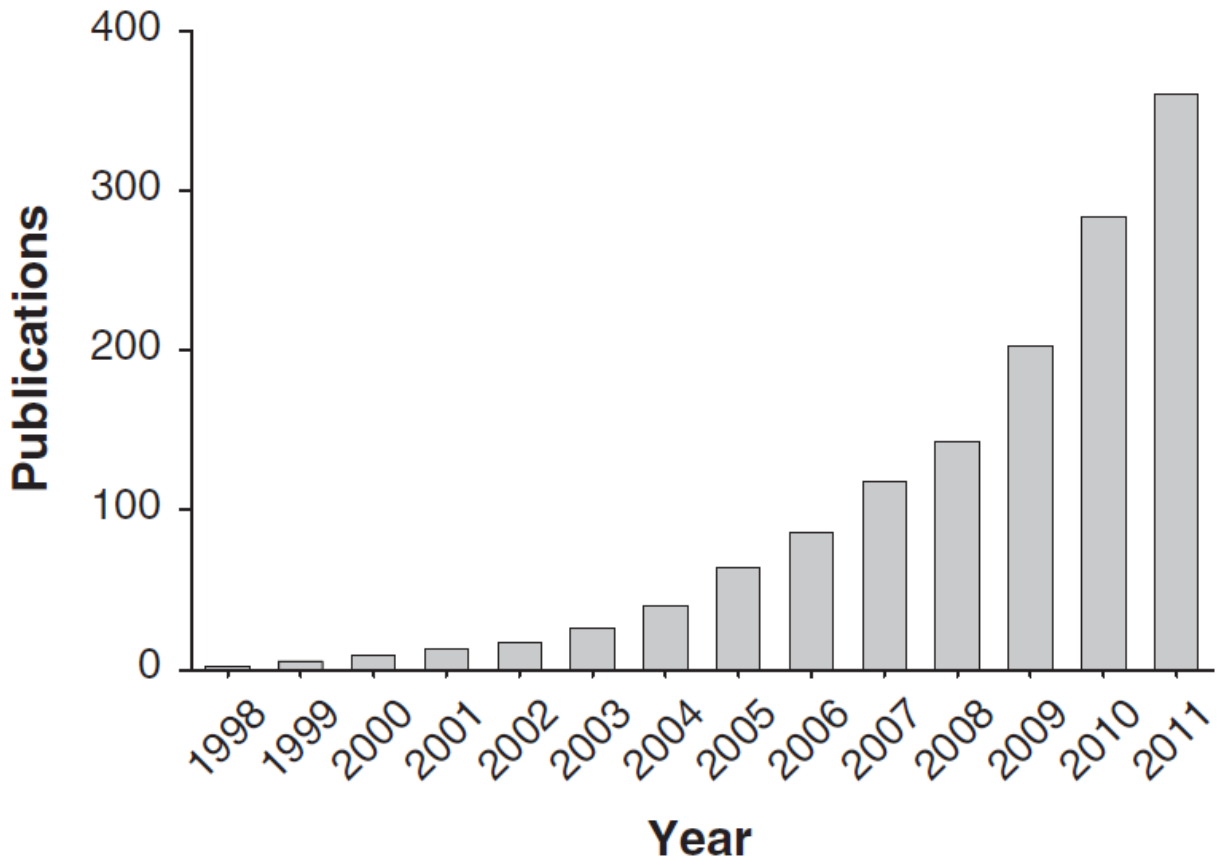

Figure 1.1 Cumulative number of publications on microneedles. The number of publications was determined by searching the PubMed database (http://www.ncbi.nlm.nih.gov/pubmed/) and Web of Science (http://apps.webofknowledge.com) on 25 November 2011 using the search terms "microneedle", "microfabricated needle", and "nanopatch". Conference proceedings were excluded.

1.1 Conventional microneedles with different structures and configurations

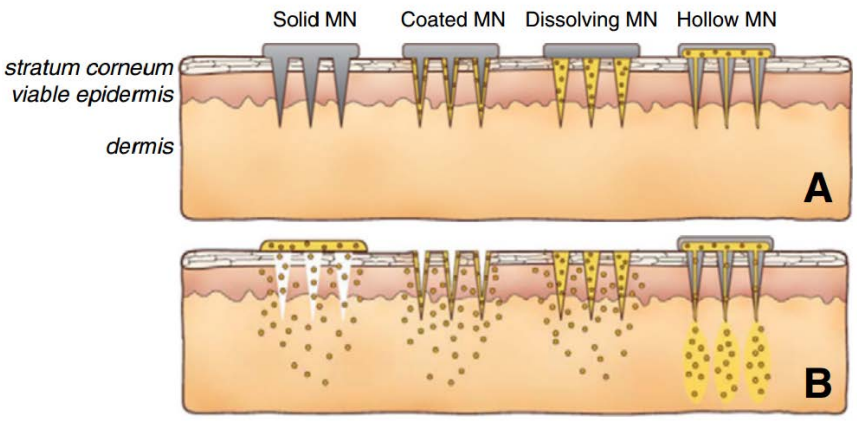

Figure 1.2 Methods of drug delivery to the skin using microneedles (MN). [8]

For an optimized delivery effect, microneedle chips are particularly desired to remain in the precise location and maintain the fluid communication with the tissues beneath the SC layer for an extended period. However, the skin is contoured and deformable. Conventional microneedle patches with a rigid and planar substrate which is made by silicon, stainless steel or nickel may encounter a difficulty to be attached tightly on the skin surface. Flexible microneedle patch has been developed to integrate polymer microneedles on a on a flexible substrate to solve this problem. Since fabricating tapered shape is not a standard process in the conventional MEMS technology, microneedles fabrication becomes the most critical part in the flexible microneedle patch. In general, these microneedles can be categorized as solid microneedles for tissue pretreatment, drug-coated microneedles, dissolving microneedles and hollow microneedles. As shown in schematically in **Figure 1.2**, each of these microneedles enable drug delivery by different mechanisms.

1.1.1 Solid Microneedles

Solid microneedles are patterned into sharp geometry which can be used to create microchannel on the skin. The drug is usually loaded into a flexible substrate under the microneedle array. When the flexible skin patch is applied on the skin, the microneedles penetrate into the skin and drugs

can be used either for local effect or uptake by capillaries for systemic treatment. The development of polymer microneedles has focused on providing sufficient mechanical strength through different materials, including polylactic acid (PLA) [9], polymethylmeth-acrylate (PMMA)[10], SU-8 [11] and maltose [12].

Solid polymer microneedles are normally patterned with unconventional process due to their tapered 3-dimensional structures. The most common way for this tapered structure fabrication is inclined ultraviolet (UV) exposure technology [13]. When a photomask and a negative thick photoresist coated substrate are fixed together, its holding stage is tilted and rotated to a UV source. The reflected UV at the interface between the resist and the substrate is exploited as well as the incident UV. With the control of tilted degree and exposure dosage, the polymer photoresist can be patterned into sharp tips. Except UV source, deep X-ray exposure is also deployed to fabricate the microneedle structures, known as the lithography, electroplating and molding (LIGA) technique [14]. It can be used to fabricate polymer microneedles as tall as a few millimeters with a high aspect ratio using standard contact lithography equipment, which is a challenging in the UV rage due to the low optical absorption rate of the polymers. Moreover, a two-photon-initiated polymerization method is utilized to fabricate microneedles structure. A near-infrared ultrashort-pulsed laser is focused into a photocurable resin to form three-dimensional (3D) microstructures using a sequential layer-by-layer fabrication technique [15] (**Figure 1.3**).

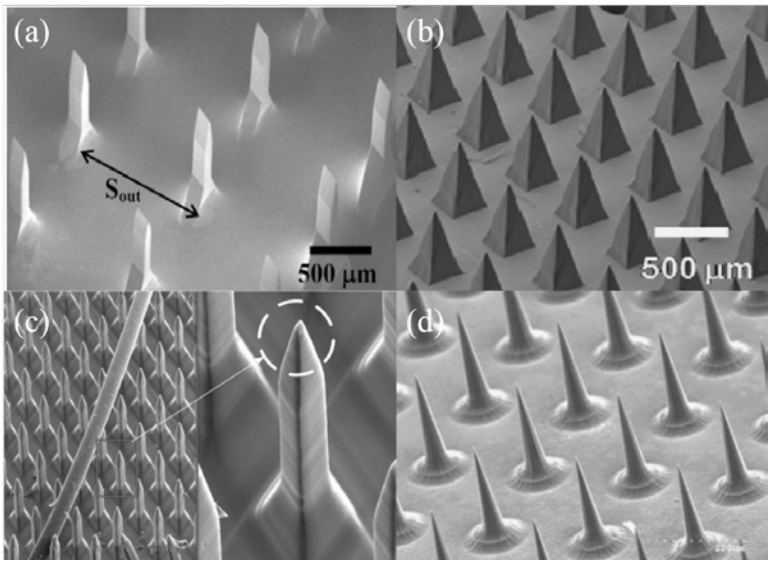

Figure 1. 3 (a) Out-of-plane polycarbonate microneedle sheets produced by the hot embossing process [16]. (b)Array of polylactic acid microneedles made by thermal molding[17]. (c) PMMA microneedle fabricated by deep X-ray exposure[10]. (d) SU-8 microneedle fabricated by RIE etching[18].

1.1.2 Coated Microneedles

Microneedles not only can be used for penetration purpose, but also as vehicles to carry and deposit drug within the skin or other tissue. Drugs can be coated on the microneedle surface and subsequently diffuse into tissues. In this way, the desired dose of drugs is delivered into tissue quickly upon insertion of the microneedles. Microneedles have been coated by a variety of processes. The most common way is dipping or spraying the microneedles using an aqueous solution often has increased viscosity to retain more of the formulation on the microneedles [19]. It can be achieved by dipping microneedles once or repeal into a large reservoir [20] or microcells [21] of coating solutions. Layer-by-layer coating techniques have also been applied into microneedle coating [22]. DNA or protein are demonstrated to be coated onto microneedles by alternately dipping into two solutions containing oppositely charged solutes. The negatively charged DNA and positively charged polymer can form a polyelectrolyte multi-layer. In addition to optimizing coating formulations, microneedle design and its advanced fabrication technique are also critical

to facilitate coated microneedle performance. For example, 3D groove-embedded microneedle has been reported to increase coating formulation amounts [23]. Microneedles with pocketed structure are demonstrated to facilitate better drug targeting in skin and to administer liquid coatings [24].

1.1.3 Dissolving Microneedles

Compared with coated microneedles, polymer microneedles also have been developed to completely dissolve in the skin and thereby leave behind no biohazardous sharps waste after usage. Biocompatible and water-soluble materials, such as sugars, are used to fabricate these dissolvable microneedles. Except that the dissolvable microneedles can penetrate skin surface as solid microneedles, drugs also can be mixed with the microneedle fabrication materials or encapsulated inside the microneedles to release into the skin.

Dissolving microneedles usually are fabricated by micro-molds. Micro-molds with specified tapered structure are filled with melted polymers. After these polymers are solidified or polymerization in the mold, microneedles with sharp tips are integrated with drug formulations. Various materials including carboxymethylcellulose (CMC) [25], chondroitin sulfate [26], polyvinylpyrrolidone (PVP) [27], polylactic acid co-polymers (PLGA) [28], and fibroin [29] have been deployed to fill into the mold cavities to form microneedles. Since the microneedles may not be entirely inserted into the skin, the drug is desired to be only encapsulated into the tip part for higher efficiency. It can be achieved by a particle-based molding method [30], forming multiple-layered microneedles [31] or adding an air bubble at the microneedle base [32].

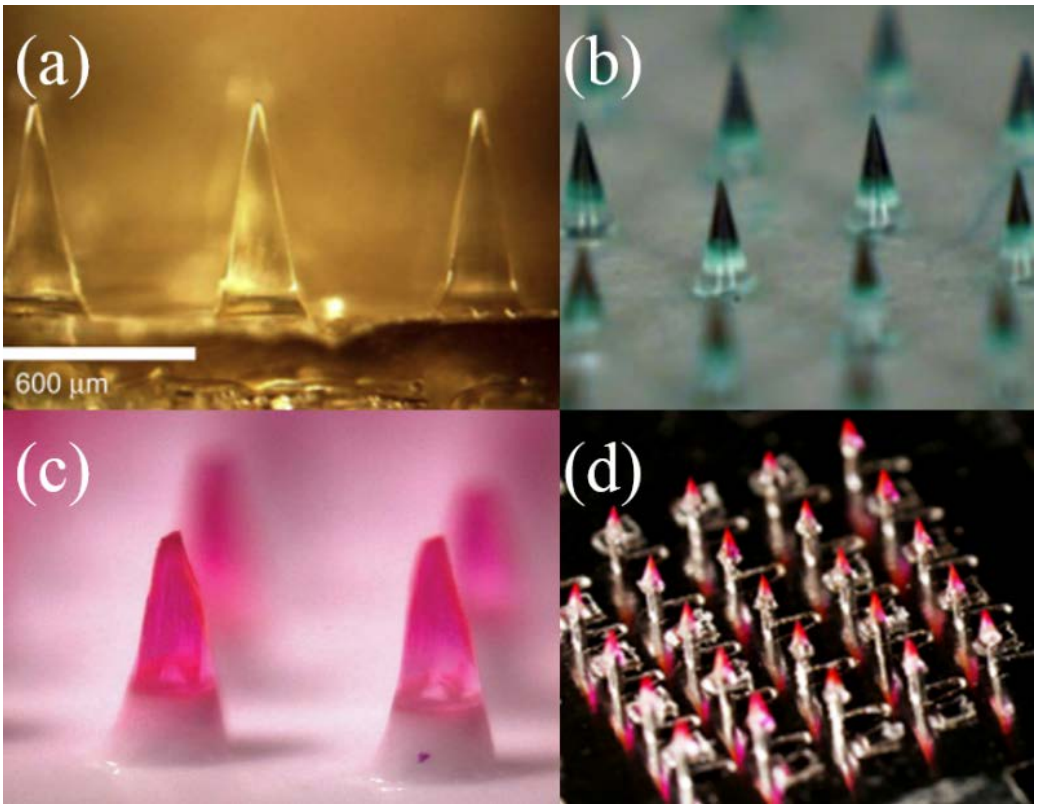

Figure 1.4 Dissolving microneedles made by (a) bovine serum albumin [33](b) chondroitin sulfate[31] (c) polyvinylpyrrolidone [34](d) polyvinyl alcohol [35].

1.1.4 Hollow Microneedles

Hollow microneedles provide a conduit for drug delivery into the skin or other tissues. The most obvious advantage of hollow microneedles is that it allows pressure driven-flow of large dosage solution. Similar to conventional hypodermic injections, the pressure applied to hollow microneedles can modulate drug flow rate. It enables a rapid bolus injection, a slow infusion or a time-varying delivery rate with a single flexible microneedle patch. Generally there are two types of hollow microneedle designs. One of them mimics the traditional hypodermic needle with a single microneedle [36]. The other type is an array of multiple hollow microneedles [37]. The advantage for hollow microneedle array device is that it can deliver liquid formulation to a wide area, which even enables a quicker delivery than subcutaneous injection [38].

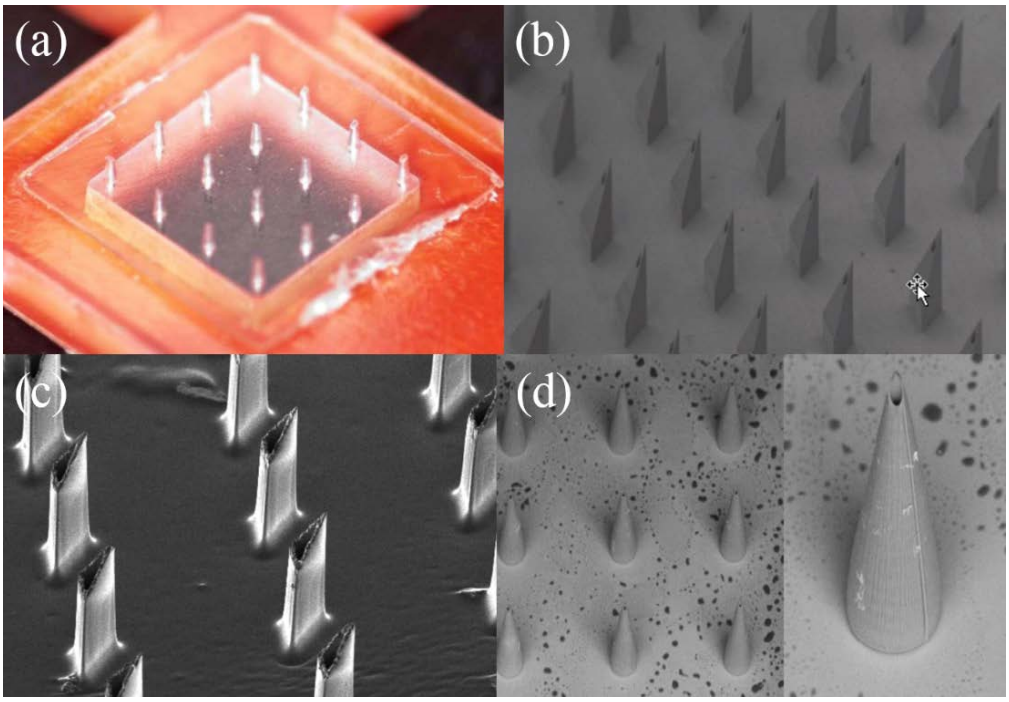

Figure1. 5 Hollow microneedle fabricated by microinjection molding [39], X-ray exposure [40], UV lithography [41] and two photon polymerization [42].

Even though hollow microneedles have been fabricated directly from a rigid substrate using standard MEMS techniques including deep reactive ion etching [43], wet chemical etching [44] and laser micromachining [37], innovative fabrication methods are developed to make polymer hollow microneedles for flexible devices. Polyphenylsulfone polymer is shown to be drilled and milled to create beveled tip shape and hollow structure [45]. A digital micro mirror stereo lithography instrument is used to fabricate hollow polymer microneedles by polymerization of liquid resin [46]. The LIGA technique is utilized to form hollow microneedles by exposing X-ray through a mask onto PMMA [47]. Direct tow-photon polymerization in a laser based rapid prototyping system is also used to form hollow polymer microneedles [48] (**Figure 1.5**).

1.2 Microneedle made by drawing lithography process

1.2.1 Theory of drawing lithography

Drawing lithography technology is based on the viscous property of a polymer in the glass transition to realize a 3D structure. The glass transition is a kinetic process between a solid state and liquid state of any amorphous polymer material. When a melted liquid polymer cools down to T_g, the amorphous portion of the polymer gradually becomes a more viscous and glassy liquid because thermal molecular motions decrease. As temperature decreases below T_g, the glassy liquid turns into a solid state because of the structural rearrangements with little relative mobility.

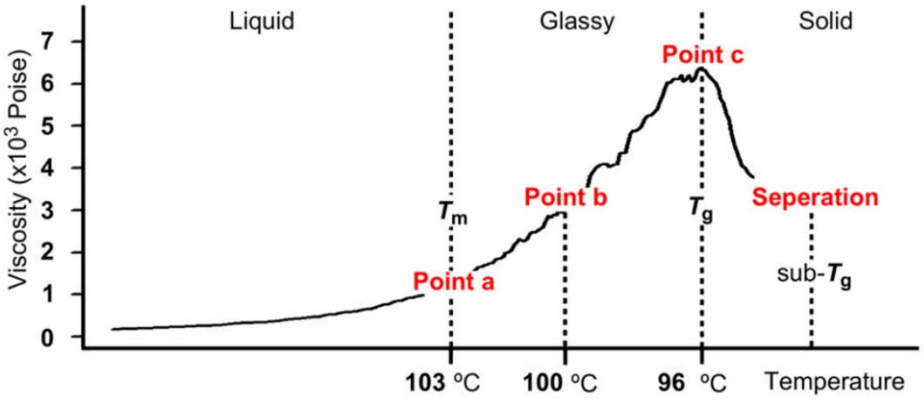

Figure 1. 6 Viscosity change with temperature and drawing point [49].

When a drawing plate is induced to form microneedles structure, drawing lithography is characterized by an elastic deformation of polymer materials in the glassy transition. Initially, a polymer material with glassy state is placed between a substrate and drawing plate. A liquid-plate interfacial adhesion is initiated when the drawing plate contact the glassy liquid on the substrate. Subsequently, the polymer with glassy state is elongated by drawing the plate. A glassy structure is generated between the substrate and substrate. Since the gravitational force and inertial force are negligible, the geometry of the glassy structure is mainly modulated by the extensional strain force from the drawing plate and the fixed coating plate (**Figure 1.7**). This glassy structure is stretched by the drawing plate and fixed coating plate from opposite directions. Since the contact area with coating plate is much larger than the contact area with drawing plate, the stretching force is

stronger from the fixed coating plate. As the drawing plate rise up, the glassy structure under the stretching force will extensional deform. The radius in the top curvature near the drawing plate is smaller than that near the fixed coating plate, which induces a wasp-waist-shape bridge. As a result of the temperature gradient through the glassy structure and change of drawing speed, the difference of stretching force in the opposite directions become so large that the extension deformation cannot remain a steady-state. The breakage of the glassy structure will form a tapered microneedle.

Previously, this drawing lithography process has been applied to fabricate 3 types of microneedles: continuous drawing for an ultra-high aspect ratio (UHAR) hollow microneedle, stepwise controlled drawing for a dissolving microneedle and drawing with antidromic isolation for a hybrid electro-microneedle (HEM).

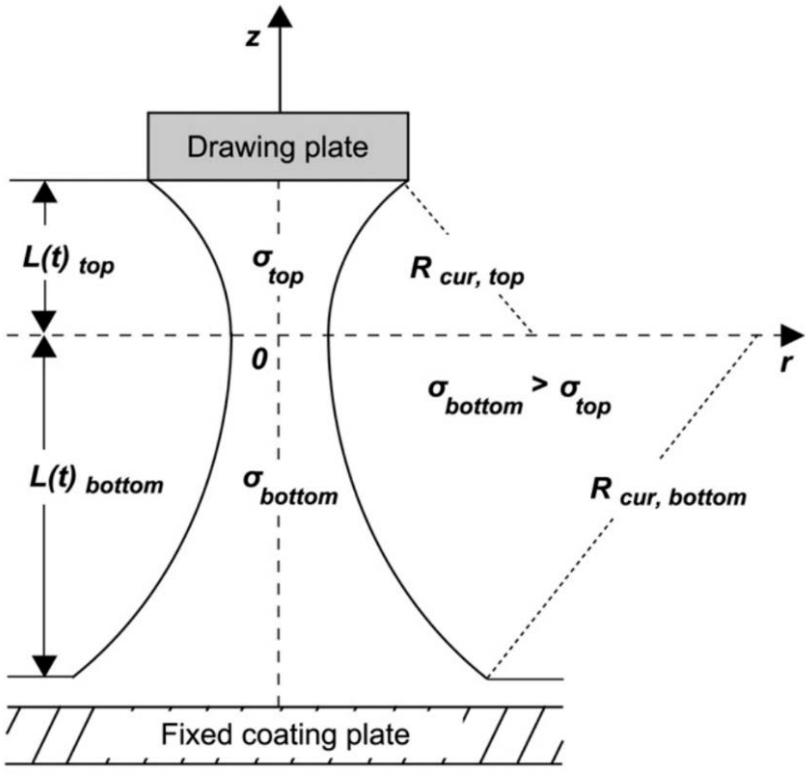

Figure 1. 7 Extensional deformation from the fixed coating surface in the glass transition. The

position of narrow necking is situated in the upper part of the intermediate liquid bridge by the axial difference of surface tension [50].

1.2.2 UHAR hollow microneedle

The UHAR hollow microneedle can be fabricated from a SU-8 based drawing lithography process as shown in **Figure 1.8**. SU-8 polymer is used as the drawing material because its viscosity was easily controlled by temperature. The non-exposed SU-8 has a T_g of 50-55℃[51] showing significant increase of viscosity by the temperature cooling down to T_g from high temperature(**Figure1.8**). SU-8 presents a possibility as a drawing substrate, and a hollow microneedle was fabricated by drawing lithography in the glass transition.

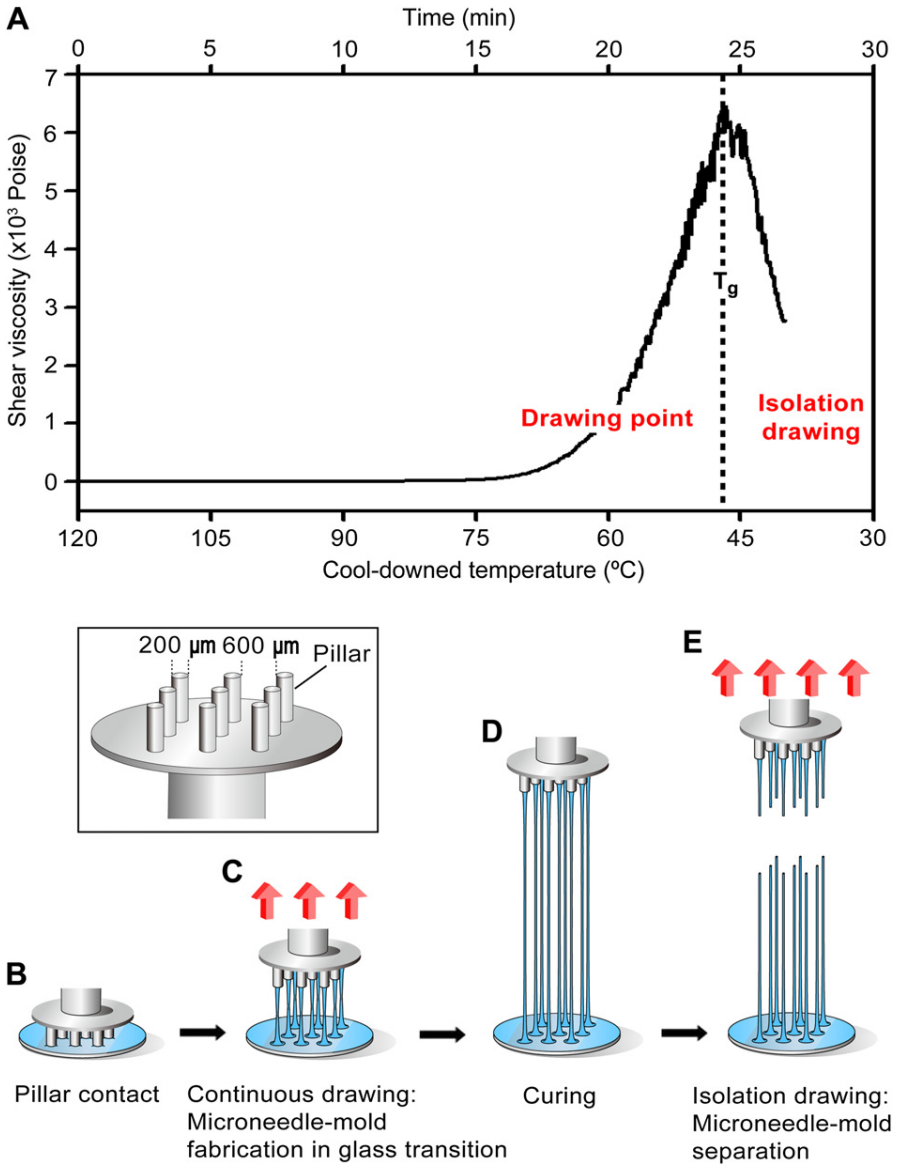

Figure 1. 8 Continuous drawing to produce a 3D UHAR microneedle mold. (A) The glass transition history of the SU-8 polymer in the cooled-down temperature. The inset shows a drawing system with patterned pillars for drawing lithography. (B) After the SU-8 contacted the patterned pillar, drawing lithography was performed. (C) Drawing caused the appearance of an extended conical-shaped bridge between the plate and pillar in the glass transition. (D) The desired liquid bridge was cured to generate a rigid structure. (E) The separation of the 3D microstructure bridge at the narrow necking position by isolation drawing produced the UHAR solid microneedle molds.

The hollow metallic microneedle is produced by nickel electroplating using the fabricated 3D microneedle mold, thus, its geometry depends on the shape of the mold. For nickel electroplating, a seed layer was deposited in the microneedle mold using Tollens' reaction (**Figure 1.9**(A)) [52,53]. The upper end of the mold was subsequently protected using enamel as a

metalplating resistor (**Figure 1.9(**B), see inset). The nickel electroplating was performed until the desired wall thickness was obtained by controlling the plating time (**Figure 1.9(**C)). Next, the SU-8 microneedle mold and enamel were eliminated using an SU-8 remover (**Figure 1.9(**D)), producing a hollow metallic microneedle array. Although negative photoresist substances such as SU-8 are typically difficult to remove after UV irradiation due to chemical changes [54], in drawing lithography, the non-exposed SU-8 is easily eliminated by SU-8 removal.

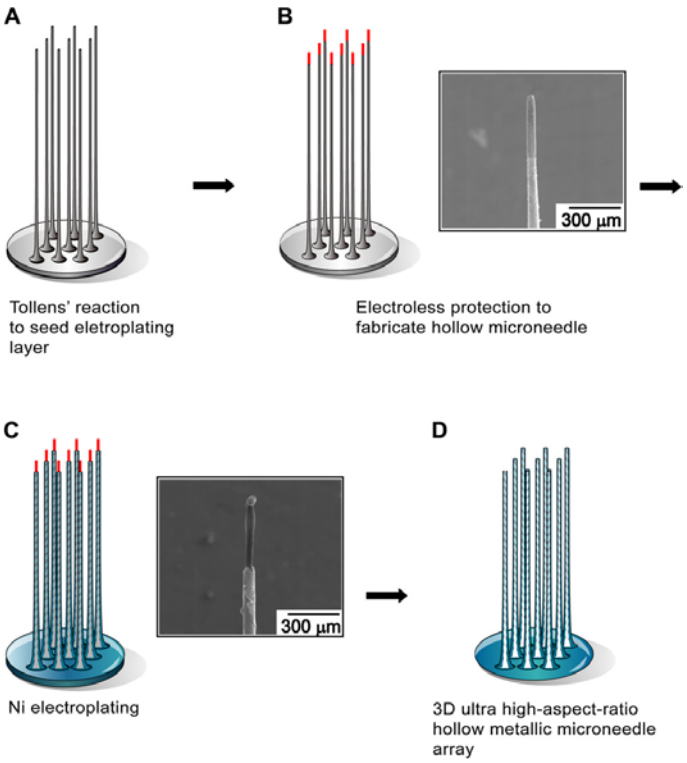

Figure 1. 9 The fabrication of hollow metallic microneedles from solid microneedle molds. (A) Chemical deposition on the solid microneedle molds. (B) The upper portion of the microneedle mold was coated with an electroless material using a drawing system. The inset shows the tip protection with enamel. (C) Nickel electroplating on conducted solid microneedle molds. The inset shows specific nickel electroplating on the conductive seed layer. (D) The hollow metallic microneedle array was created upon elimination of the electroless protection and the SU-8 microneedle mold.

Scanning electron microscopy revealed the microneedle mold had a tapered conical shape with a 20 µm flat tip diameter and a 300 µm base, yielding an aspect ratio over 100 (**Figure 1.10(A)**). The size of the hole in the hollow microneedle corresponded to the diameter of the mold

at the top. A 20 μm needle diameter is large enough to allow passage of molecules such as target drugs while minimizing skin damage. Furthermore, the conical shape of the 300 μm base provides support for penetration of the skin barrier. Although the hollow metallic microneedle was shorter than the mold due to the enamel coating of the mold which occupied 200 μm of the mold, the UHAR hollow microneedles had a length of 2 mm (**Figure 1.10(**B)).

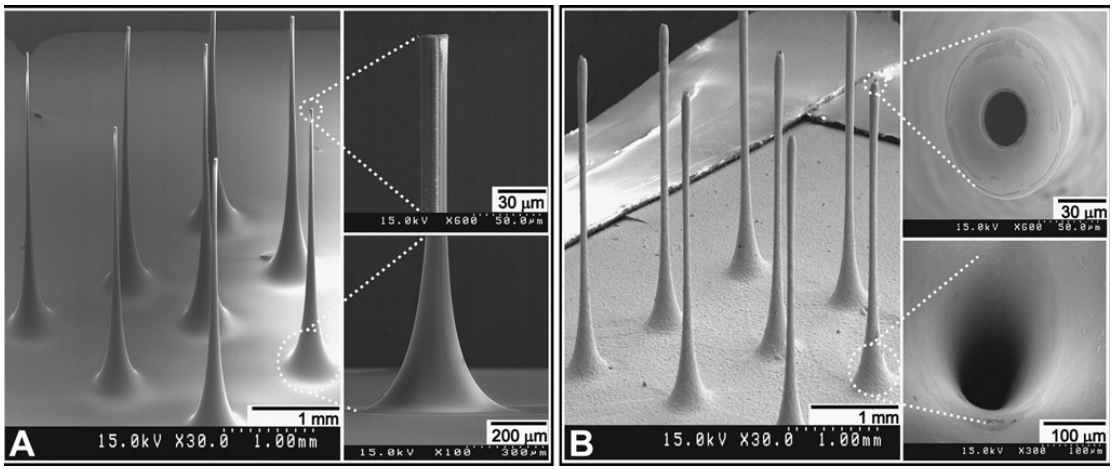

Figure 1. 10 UHAR solid microneedle molds and hollow metallic microneedles. (A) The microneedle mold had a tapered conical shape with a 20 μm flat tip diameter, a 300 μm base, and an aspect ratio over 100. (B) A 3 by 3 array of hollow UHAR microneedles with a length of 2000 μm and an inner diameter of 20 μm.

1.2.3 Stepwise controlled drawing for a dissolving microneedle

Maltose has been widely used as a safe polymer for the encapsulation of biomolecules[55], and is dissolved easily by the hydrolytic cleavage of maltose-glucoamylase in the skin [56]. In particular, maltose can be used as a structural material for the fabrication of dissolving microneedles because the glass transition of the maltose, thus the viscosity, was easily regulated by manipulating temperature during drawing. Maltose became liquid at temperatures over its T_m (102~103℃), and the viscosity of the liquid maltose progressively increased with cooling until T_g (95±4℃) [57,58] and then further cooling past the T_g induced a solid state. The viscosity change in the maltose glass transition provided the conditions for the drawing lithography.

The maltose, however, showed a dramatic change of viscosity in the glass transition in a short temperature range as shown in **Figure 1.11**(A) and the continuous drawing of maltose showed the different shapes of the dissolving microneedle depended on the maltose viscosity. When the drawing was performed at T_m, a 3D structure was not produced even at a low drawing rate, resulting in drawing failure, because the surface tension was more than the tensile stress of the extending maltose during drawing. Although drawing at a slightly lower temperature approximating T_m can elongate a glassy maltose quickly, the temporary extensional deformation can become a capillary break-up by quick self-thinning.

This break-up can be prevented when drawing is applied between T_m and T_g at drawing point b due to increase in the shear viscosity which increased the initial planar extensional viscosity of maltose, and axial drawing of 400 μm/s for 3 s created a bat shape (**Figure 1.11**(B)). The general position of narrow necking from a coated polymer in a glass transition is settled into the upper part of the intermediate liquid bridge because surface tension in the bottom region is bigger than in the top region. However, extensional deformation in the short glass transition of maltose showed an entirely different aspect from the normal extensional deformation model. The short-term of the glass transition induced a relatively fast alteration to the solid at the top region of the liquid bridge, and strain-hardening of the top region had no direct influence from surface tension. Consequently, the bottom region near the fixed coating surface presented a local surface tension within the total extensional structure, resulting in the lower narrow necking position than the intermediate liquid bridge. Local surface tension in the bottom region led to irregular bat-shaped extensional deformation. Therefore, the fabrication yield of the bat shape was low due to the breakage at the narrow necking near the bottom during isolation drawing.

As another approach, extensional deformation in drawing point c produced a cylinder shape with a blunt tip of 200 μm diameter, which is the same as the pillar diameter shown in **Figure 1.11**(C). The surface tension at T_g is suddenly reduced as the fluid like response above T_g transitions to solid-like response below T_g. As a result, the drawing at T_g formed a cylinder column without narrow necking by homogeneous extensional flow without direct influence from surface tension as an ideal extensional deformation model. Although continuous drawing lithography suggested the possibility of the direct fabrication of a dissolving microneedle from maltose, a blunt cylinder was not applicable as a microneedle for transdermal drug delivery because the shape rendered skin penetration difficult; precise control of the drawing was required for the fabrication of a sharp microneedle capable of penetrating the skin.

Finally, stepwise controlled drawing lithography was designed to shape a particular sharp-conical microneedle by combining the above 2 continuous drawings (**Figure 1.11**(D)). The primary drawing of 400 μm/s for 1 s produced a wasp-waist bridge with a bat shape between the pillar and the maltose surface with a diameter of 60 μm at drawing point b by the irregular extensional deformation model. Because the main drawing (400 μm/s speed for 3 s) was performed at drawing point c after the wasp-waist bridge was produced, the wasp-waist bridge behaved like a pillar resulting in a sharp cylinder column with a total height of 1500 μm. After curing the structure, the upper site of narrow necking in the bridge structure was separated from the sharp-conical cone microneedle by isolation drawing. Using this stepwise controlled drawing, the bat and cylinder shape, which were not suitable as a microneedle structure, were avoided and a sharp conical cone shape was produced from the drawn 3D wasp-waist bridge (**Figure 1.11**(D)) with 1200 μm length, and 60 μm flat tip diameter. Additionally, the authors' proposed stepwise controlled drawing technique can flexibly change the length of a dissolving microneedle by

controlling the drawing rate and time. This length flexibility of a microneedle can facilitate the local delivery of a drug to the specific clinical point of skin [59-60], and thus overcome the limitation of the micro-casting method that restricted the free modification of length.

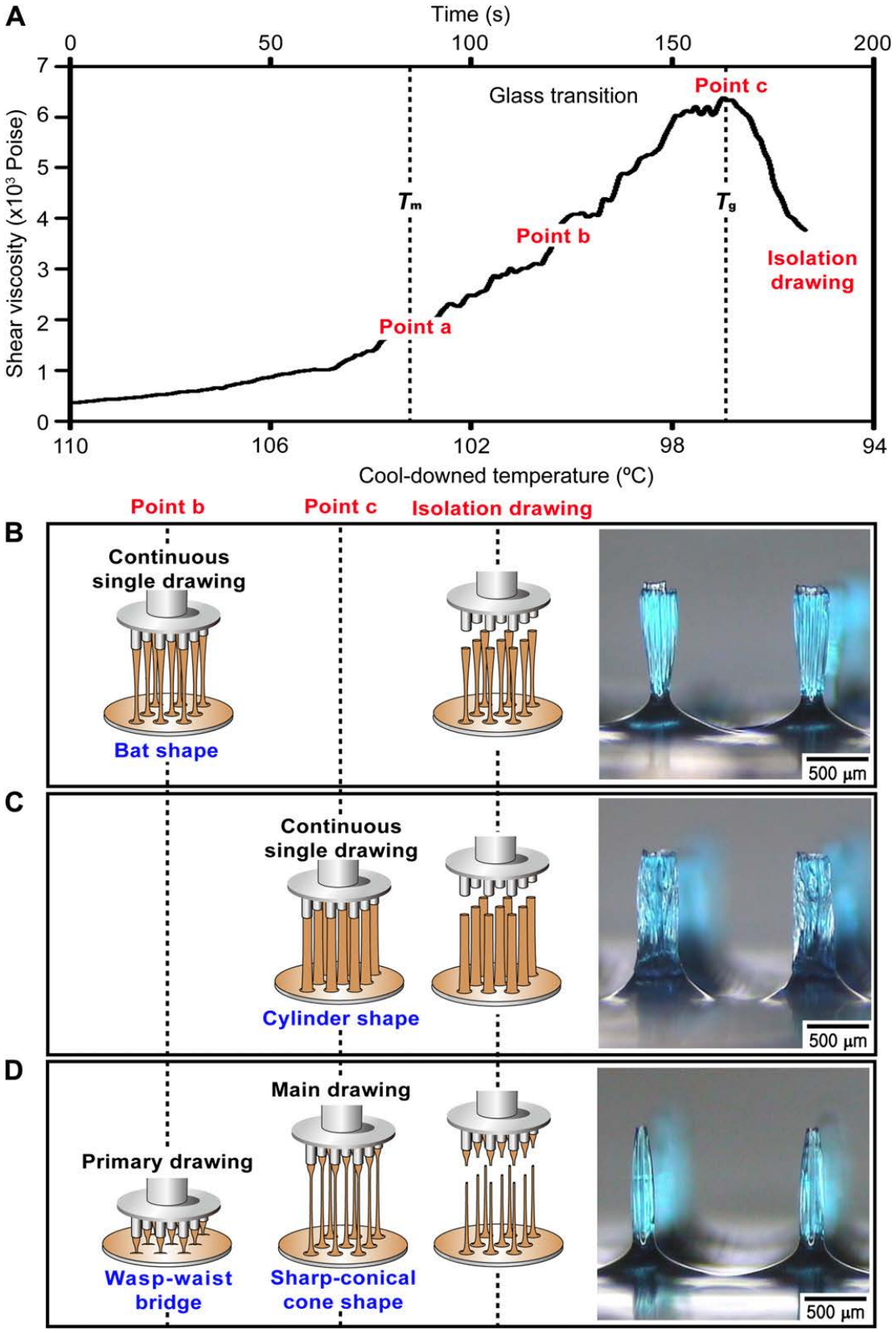
A
Time (s)
0
50
100
150
200
7
6
5
4
3
2
1
0
Shear viscosity (x10³ Poise)
Glass transition
Point c
T_m
T_g
Point b
Isolation drawing
Point a
110
106
102
98
94
Cool-downed temperature (ºC)
Point b
Point c
Isolation drawing
B
Continuous single drawing
Bat shape
500 µm
C
Continuous single drawing
Cylinder shape
500 µm
D
Main drawing
Primary drawing
Wasp-waist bridge
Sharp-conical cone shape
500 µm

Figure 1.11 The stepwise controlled drawing lithography for fabrication of a dissolving microneedle. (A) The viscosity change with temperature and drawing point in the glass transition history of maltose. Drawing point a at T_m, drawing point b at the middle of T_m and T_g, and drawing point c at T_g. After sub-T_g, elongated structures became cured solid. (B) Bat shapes were produced by continuous drawing at drawing point b. (C) Cylinder shapes were fabricated by continuous drawing at drawing point c. (D) Sharp-conical cone shapes were fabricated by stepwise controlled drawing, primary drawing at drawing point b and main drawing at drawing point c. After curing was completed, the fabricated 3D structures were separated from narrow necking by additional isolation drawing at sub-T_g.

1.2.4 Monolithic fabrication of a HEM

The monolithic fabrication of a HEM was possible by using an electrode as the pillar resulting in the integration of a dissolving microneedle on an electrode as shown in **Figure 1.12**(A). An electrode with a diameter of 300 μm, a lift-up of 300 μm, and a pitch of 1mm was made in a 5×5 array in a 1 cm circle from an aluminum plate using a computerized numerical control machine. The HEM electrode contacted the coated liquid maltose at a temperature greater than the T_m of maltose. Because the dramatic change in maltose viscosity in the glass transition (T_m ~ T_g) provides a critical condition for the successful elongation of dissolving microneedles by drawing lithography. Drawing of the electrode was performed at the middle of the glass transition to produce a 3D elongated structure with a bat shape by irregular extensional deformation (**Figure 1.12**(B)). These elongated bat-shape structures were cured by cooling the maltose to a temperature lower than the T_g (at 80℃), and liquid maltose perfectly became solid maltose (**Figure 1.12**(C)). Subsequently, the bottom of the cured bat-shape structures was isolated from the fixed coating surface by remelting the maltose coating at a temperature greater than the T_m. This antidromic technique with remelting created the bell-shaped dissolving microneedle with an ultra-sharp tip diameter, and facilitated the monolithic hybrid assembly of a dissolving microneedle on an electrode (**Figure 1.12**(D)). The dissolving microneedle of the HEM had a geometric bell shape with an ultra-sharp tip diameter of 5 μm and a length of 400 μm (**Figure 1.12**(E)). Dissolving

microneedles and electrodes were integrated into monolithic HEMs of a 5 × 5 array (**Figure 1.12**(F)).

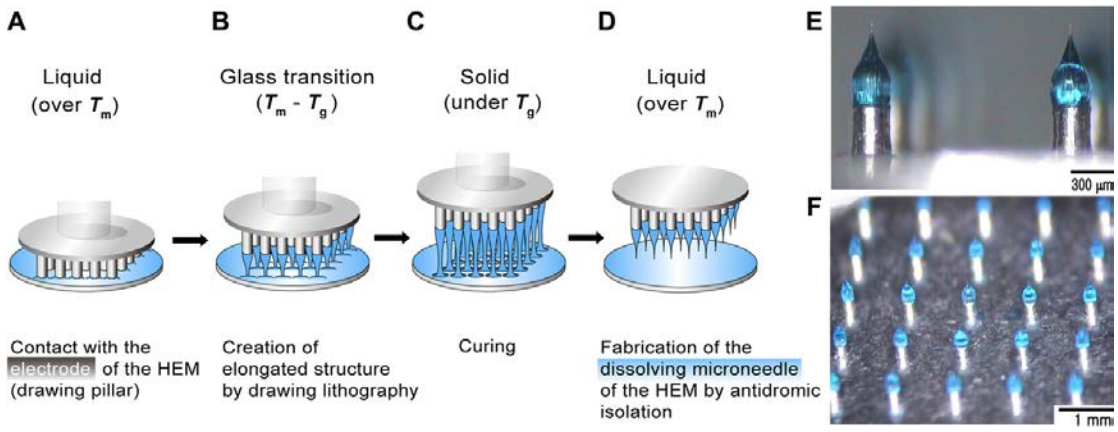

Figure 1. 12 The monolithic fabrication of the HEM by drawing lithography with antidromic isolation. (A) Liquid maltose, melted at a temperature greater than its T_m, was coated on a planar surface, and contacted with the 5 × 5 array electrodes of the HEMs as a drawing pillar. (B) The glassy maltose in glass transition between T_m and T_g was elongated by drawing of electrodes. (C) After lowering the temperature to sub-T_g, the elongated 3D structures were cured to a solid state. (D) The coating surface was melted at a temperature greater than T_m to isolate elongated 3D structures from the 2D coating surface and this antidromic isolation fabricated the dissolving microneedles of the HEMs. (E) A bell-shaped dissolving microneedle of the HEM had an ultra-sharp tip diameter of 5 μm and a length of 400 μm. A dissolving microneedle and an electrode were integrated into a monolithic HEM. (F) A 5 × 5 array of fabricated HEMs.

1.3 Motivation of integrate microneedles with functional components

In summary, microneedle device has been demonstrated with all kinds of materials and processes for different applications. For the conventional microneedles, the process to make the whole microneedle device is affected by the process to realize the sharp tip either by molding or etching. Because the process to realize the 3D sharp tip is normally not compatible with other thin film processes. Thus, it is difficult to integrate the microneedle with other functional components to realize other specific applications.

However, by leveraging the drawing lithography process, the sharp tip assembly can be the last

step of the microneedle device. It means that the compatibility of the process to make the sharp tip is not a main concern in the design of the microneedle device. Therefore, more functional components, such as microfluidic control system and nanofilters, are feasible to be integrated with microneedle.

Moreover, microneedle is just a key component for a wearable medical device which is suitable for self-managed drug delivery. With the quickly increasing number of aging people all around the world, such one stop medical care solution, including disease detection and drug delivery, is desired more than ever. A complete wearable medical device should include the functions of skin penetration, fluidic control system for drug loading, drug delivery and volume control, disease symptom sensor for result feedback, energy source enabling self-powering and self-fixation onto skin. However, such integrated system is still uninvestigated. The challenge mainly comes from how to realize mechanical structure for the functions such as fluidic control, energy harvester by soft and bio-compatible materials required for medical application. Initiating the system-level integration of all the functional components is meaningful for the future development of wearable drug delivery skin patch.

In this thesis, we will explore the feasibility of integrating the microneedles by drawing lithography with other functional components to realize a drug delivery system for specific applications which are not demonstrated before. In Chapter 2, we will first improve the drawing lithography process and assemble both maltose and SU-8 sharp tips onto hollow micro-tubes to realize a continuous drug delivery. Based on the microneedle configuration with SU-8 sharp tips mentioned in Chapter 2, in Chapter 3, we integrated CNT nanofilters within to realize a selective drug delivery. Different drug molecules in the same solution can be delivered by applying different conditions. This technique will enable a programmable drug delivery by using microneedle device

in the future. To realize a wearable drug delivery device which is strongly desired, we plan to make a whole microneedle device flexible. However, the needle breakage during the skin penetration causes problems for the microneedle assembled onto soft substrates. To overcome this issue, in Chapter 4, a bendable microneedle is developed. This bendable microneedle can adapt the curvy skin surface and avoid the needle breakage during skin penetration. By using this bendable microneedle, we further realize a sophisticated skin patch in Chapter 5. In this skin patch, we add the triboelectric energy harvester (TEH) as a power source for the active component to be integrated in the future. Another major issue for the microneedle skin patch is that the volume of the drug delivered cannot be well controlled. Previously the delivery volume can be controlled by syringe pump. However, as a standalone device, a volume sensor is necessary to measure how much drug to be delivered, especially for the application of insulin delivery. In Chapter 6, we use the similar TEH demonstrated in Chapter 5 as a liquid volume sensor and integrate it within the skin patch to realize a manually controlled drug delivery.

Chapter 2 Drawing Lithography Technology for fabrication of bio-dissolvable and non-bio-dissolvable microneedles

Microneedles fabrication is the most critical part in the development of flexible microneedle patch. As we addressed in the chapter 1, conventional fabrication for microneedles are time consuming and expensive. Drawing lithography technology is an innovative maskless approach in which a 3D polymer structure is directly extended from 2D viscous polymer materials to form ultrahigh-aspect-ratio microneedles. The straightforward process does not need any special equipment and is compatible to the other MEMS fabrication procedures. It is a new technique to overcome the drawbacks in conventional fabrication technologies and able to develop microneedles with various materials on the flexible microneedle patch. In this chapter, we will introduce two different kinds of microneedles based on this drawing lithography process.

2.1 Drawing Lithography Technology for Making Flexible and Biodissolvable Microneedle patch

In transdermal drug delivery, the delivery performance strongly depends on the molecular size of the drug. Delivery of large molecular drugs such as insulin has been already found to encounter an efficiency problem [61]. Combining dissolvable microneedles with microfluidic components is a promising way since this method can apply pressure on the drug solution to facilitate the large molecular drug diffusion process. We will demonstrate a new method based on drawing lithography technology to achieve this purpose. In order to overcome the barrier of SC layer, sharp dissolvable maltose tips are created on top of SU-8 vertical microtubes. After the maltose tips

penetrate into the skin and are dissolved by body fluid, a large volume of the desired drug will be delivered through SU-8 microtubes.

2.1.1 Design and Fabrication

2.1.1.1 Design Considerations

In this flexible device, we leverage the unique features of maltose based microtips, i.e., high mechanical strength and biodissolvability, and validate the feasibility of integration of sharp maltose tips on top of SU-8 microtubes in the present study (**Figure 2.1**). After sharp maltose tips perforating the SC layer of the skin, maltose tips will be dissolved in the body fluid within a few minutes subsequently and drugs can be delivered through the SU-8 microtubes. Since the drugs are driven by pressure through microtubes in a continuous manner, the large molecular drug can also be delivered in an efficient way.

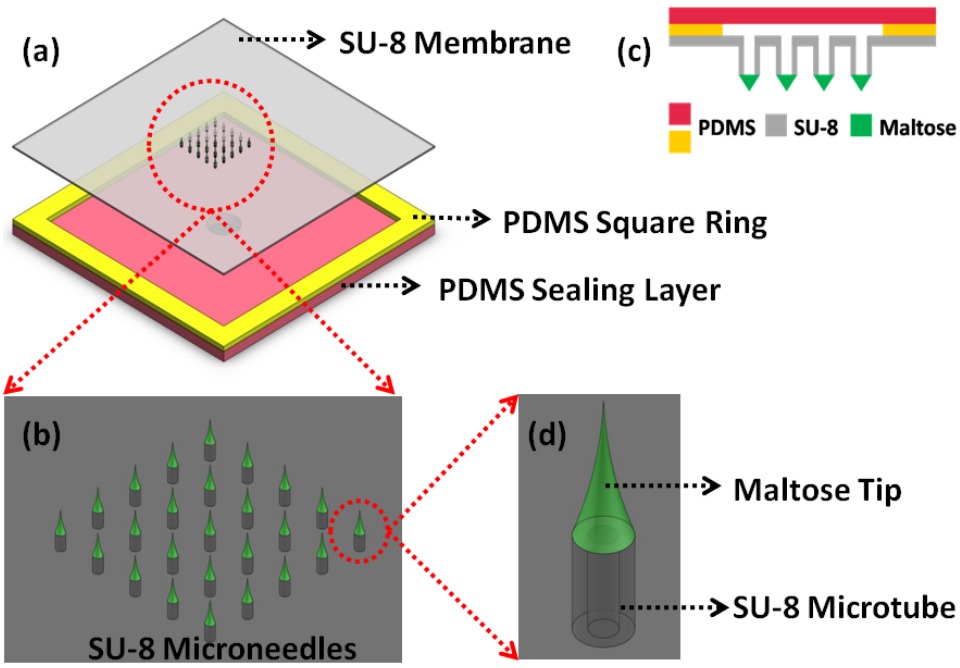

Figure 2.1 Schematic illustration of the SU-8 microneedles. (a) Top view of the device structure. (b) A 5×5 SU-8 microneedles array. (c) Cross section of the device structure. (d) Single microneedle structure.

An array of 5×5 SU-8 microtubes was patterned on a 140 μm thick, 2.5cm×2.5cm SU-8 membrane (**Figure 2.1** (a)). Each SU-8 microtube was 350 μm high. The inner diameter of the SU-8 microtube is 150 μm, while the outer diameter is 300 μm (**Figure 2.1** (d)). Maltose needles of 1000 μm height were integrated on the SU-8 microtubes to ensure the ability of transdermal perforation. Two PDMS layers and the 2.5cm×2.5cm SU-8 membrane were bonded together to form a sealed chamber for retaining drugs from the connection tube during delivery process. The 2.5cm×2.5cm size of the device was designed on purpose in order to conceptualize a flexible skin patch kind of drug delivery device. However, the critical area comprising the SU-8 microneedles at the center was only 6mm×6mm. The large marginal space offered sufficient area to achieve good bonding between SU-8 layer and PDMS layer, i.e., tolerating higher pressure to drive drugs into tissues during the delivery process.

2.1.1.2 SU-8 Microtubes Fabrication

As shown in **Figure 2.2**, SU-8 microtubes fabrication started from a layer of Polyethylene Terephthalate (PET, 3M USA) film pasted on the Si substrate by sticking the edge area with kapton tape (**Figure 2.2** (a)). The PET film, a kind of transparent film not sticky at the both side, was used as a sacrificial template to dry release the final device from the Si substrate because of the poor adhesion between PET film and SU-8. Before the dry releasing process, all the following SU-8 processes would not make the device fall apart from the PET layer. Although in the work presented by Fernández *et al* [62], only the kapton film was used for the release purpose, we found that when the SU-8 patterned area on the kapton film was large, tearing off the film from the kapton film without damaging the device required extreme delicacy. This was because both the patterned SU-8 layer and Si substrate were rigid layers. However, in our process, the sticky kapton film which just applied along the edges of samples could be easily removed after the device developed in SU-

8 developer. The PET film with the SU-8 layer was separated from the Si substrate. Then SU-8 layer could be dry released from the PET film just by slightly bending the PET film.

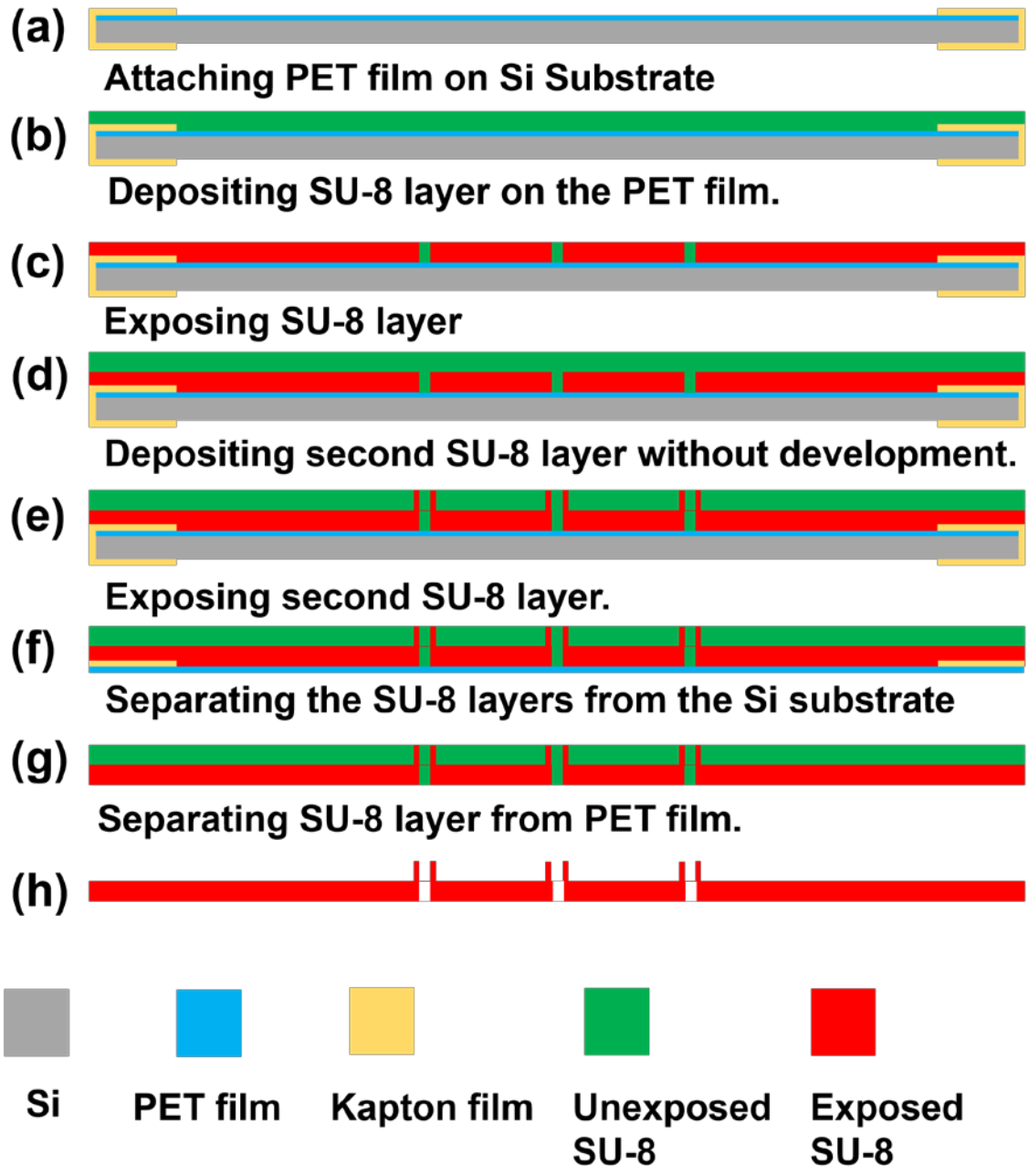

Figure 2.2 Fabrication process for SU-8 microtubes.

A 140 µm thick SU-8 layer was deposited on the fixed PET film (**Figure 2.2** (b)). To ensure a smooth SU-8 surface, this deposition was conducted in two steps of coating with 70 µm layer each.

In each step, SU-8 2050 was spun at 2000 rpm for 30 seconds, followed by prebaking steps at 65 °C for 10 minutes and 95 °C for 30 minutes. After the prebaking steps, this SU-8 layer was exposed under 450 mJ/cm^2 UV energy to define the membrane structure on this layer (**Figure 2.2** (c)). After exposure baking steps at 65 °C for 5 minutes and 95 °C for 15 minutes, another 350 μm SU-8 layer was directly deposited on this layer in two steps without development (**Figure 2.2** (d)). If the first layer was developed to get patterns, the surface would not be smooth enough to achieve a uniform second SU-8 layer on it. With careful alignment (alignment accuracy is 20μm), an exposure of 650 mJ/cm^2 energy was performed on the second layer to get the pattern of SU-8 microtubes, which were precisely above the holes patterned on the first layer (**Figure 2.2** (e)). After post exposure baking steps at 65 °C for 10 minutes and 95 °C for 30 minutes, then the SU-8 device with PET film were released from the silicon substrate by the same method described before (**Figure 2.2** (f, g)). After soaking in an ultrasonic cleaner for 30 minutes, the SU-8 microtubes array on the membrane was developed (**Figure 2.2** (h)).

2.1.1.3 PDMS Bonding

To bond the PDMS layer with SU-8, PDMS with mixing ratio of prepolymer base and curing agent in 10:1 was prepared firstly. After degassing, PDMS was cured and cut into small pieces. Then the first PDMS layer with square ring structure was treated with N_2 plasma to introduce amino groups on one side. When this PDMS surface was contacted with the bottom side of SU-8 surface having epoxy groups on surface, interfacial amine-epoxide chemical reaction took place at an elevated temperature. Therefore, after cured at 120 °C for 15 minutes, PDMS was permanently bonded with SU-8 layer.

After the SU-8 membrane was released from the PET film, it bent during the developing process (**Figure 2.3** (b)), due to residue stress gradients in SU-8 membrane. Here a homemade stage was

used to reduce this effect. As shown in **Figure 2.3** (a), two akryl plates were applied to clamp SU-8 membrane bonded with PDMS layer. Other two PDMS layers were used as soft buffer layers to protect the device. This stage offered a flat surface and uniform pressure on the SU-8 membrane. When put into the 120 °C oven, the SU-8 membrane will slightly deform because the bonded PDMS layer had a thermal expansion at this high temperature. Such effect relieved the previous bended layers and leads to a flatter surface (**Figure 2.3** (c)). This flat surface was critical for the following maltose tips drawing process. Then oxygen plasma was performed on the opposite side of the first PDMS layer and one side of the second PDMS layer. After attaching these two surfaces together, two PDMS layers were bonded firmly together to form a fluidic chamber for the drug to flow into microtubes.

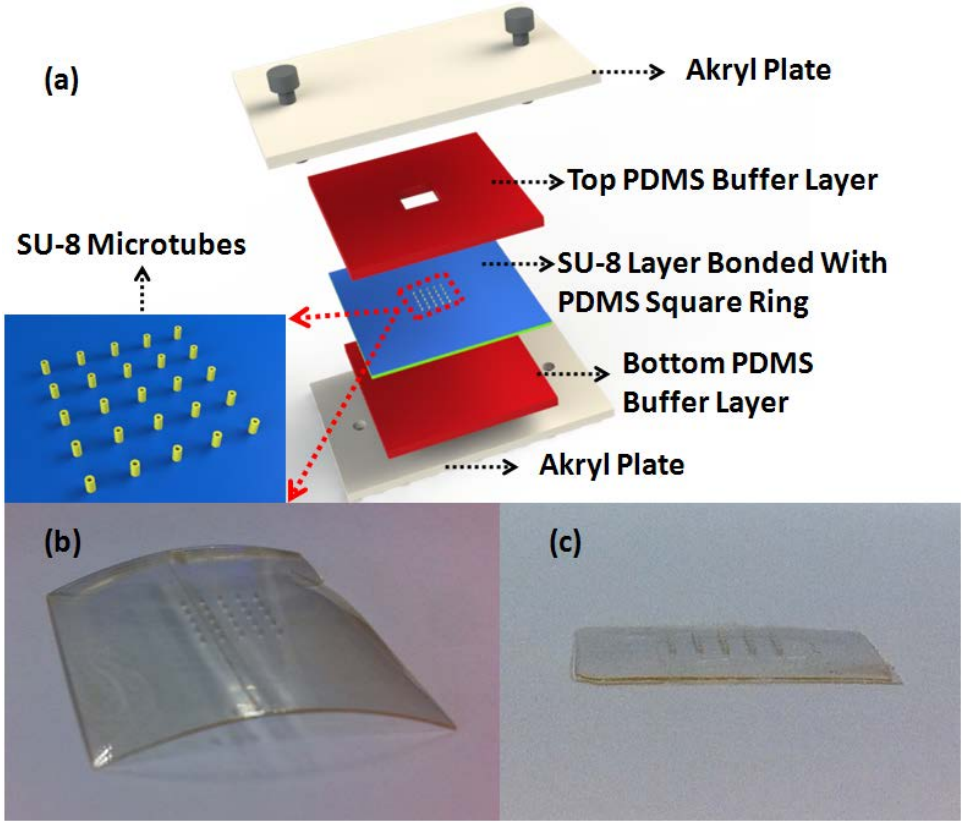

Figure 2.3 (a) Schematic illustration of the homemade stage to ensure flat SU-8 membrane surface. (b) SU-8 membrane bends after development. (c) After bonded with PDMS and clamped

in the stage, the membrane becomes flat.

2.1.1.4 Drawing Process of Maltose Tips

Maltose needles were integrated on the SU-8 microtubes by the drawing lithography technology. Lee *et al* encapsulated the drugs in maltose and patterned the maltose tips by drawing lithography[63]. Since the temperature in this method must be higher than 100 °C, a large group of drugs cannot stand at this temperature and will be degenerated. In our device, drugs will be delivered through SU-8 microtubes and the maltose is just used as sharp tips for skin penetration. Without facing the high temperature effect, our device is a generic platform to administer various kinds of drugs.

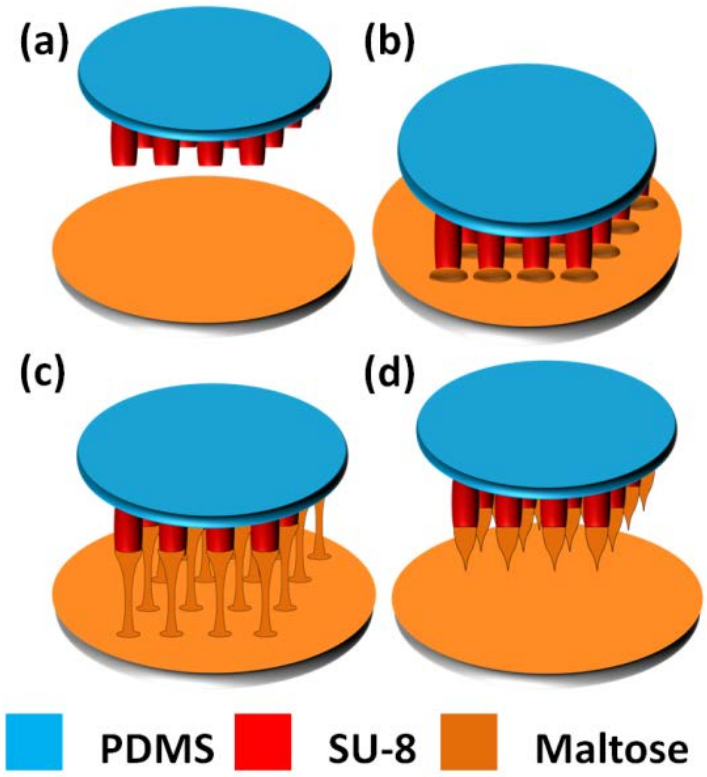

Figure 2.4 Fabrication process for maltose tips. (a) Expelling water at 140 °C. (b) Immersing microtubes into the maltose at 140 °C. (c) Drawing the tips at end of the microtubes when the temperature increases up to 160 °C. (d) Increasing drawing speed to form sharp tips.

As shown in **Figure 2.4**, fabrication of maltose tips on top of SU-8 microtubes was divided into four steps. First, concentrated maltose solution containing Methylene blue, which was used for a better inspection during penetration process, was dripped on a glass slide. The slide was kept at 140 °C on the hotplate until the water inside maltose solution completely vaporizes and maltose becomes liquid state (**Figure 2.4** (a)). Secondly, device of SU-8 microtubes was fixed on a precision stage which can control the position of SU-8 microtubes in three-dimension. Then we immersed the SU-8 microtubes into the liquid maltose at 140 °C and maltose liquid coated on the SU-8 microtubes' surface (**Figure 2.4** (b)). Thirdly, we gradually increased the temperature of liquid maltose and start drawing SU-8 microtubes away from interface of the liquid maltose and air (**Figure 2.4** (c)). Finally, when the temperature rise up to 160 °C the drawing speed was increased. Since the maltose liquid was less viscous at higher temperature, the connection between the SU-8 microtubes and surface of the liquid maltose became individual maltose bridge and shrunk gradually, and then broke. The end of shrunk maltose bridge formed a sharp tip on top of each SU-8 microtube when the connection was collapsed (**Figure 2.4** (d)). **Figure 2.5** showed the final drug delivery device containing SU-8 microtubes integrated with maltose tips and microfluidics, e.g. channels and the chamber formed by PDMS.

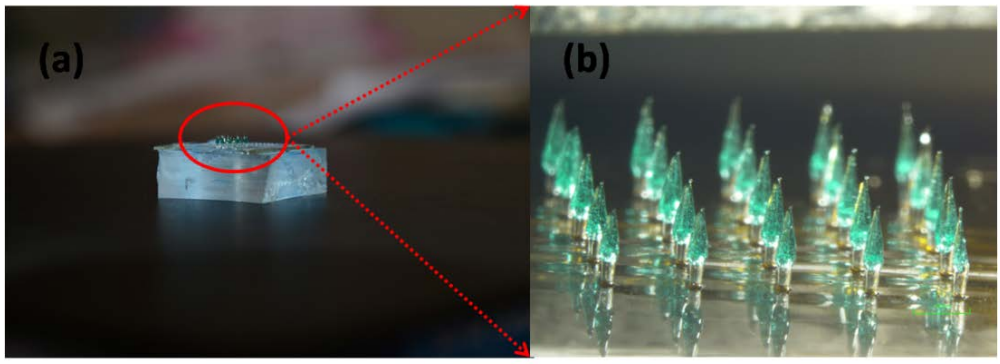

Figure 2.5 Optical image for the finished SU-8 microneedles. (b) Detailed illustration image for the microneedles array.

2.1.2 Results and Discussion

2.1.2.1 Optimization of Spacing Between Maltose Tips

To ensure the stronger and shorter maltose tips of a mircroneedle array for an easier skin penetration, experiments are conducted to optimize parameters in the drawing process. Temperature of melted maltose during drawing step and drawing speed are identified as the key parameters to get up to 1000 μm tall maltose sharp tips on the SU-8 microtubes. Although the maltose tip can be easily and routinely formed on top of SU-8 microtubes at 140 °C and optimized drawing speed, the formation of uniform maltose tips array also depends on the spacing between two adjacent SU-8 microtubes.

Table 1.1 Ratio of individual maltose tips to clustered maltose tips among a 5x5 microneedles array

Height of Microtubes	Spacing Between two SU-8 Microtubes			
	300μm	**600μm**	**600μm**	**1200μm**
150μm	0/25	5/20	15/10	25/0
250μm	0/25	13/12	21/4	25/0
350μm	0/25	17/8	25/0	25/0

When the maltose melted at 140 °C, the planar extensional viscosity in maltose easily leads adjacent maltose tips to clusters. We have investigated various spacing between two adjacent maltose tips to get the minimum spacing. The height of microtubes changed from 150μm to 350 μm with the interval of 100μm while the spacing changed from 300μm to 1200μm with the interval of 300μm. There were in total 12 different dimensions. Four chips were tested for each dimension as a group and the total trails were 48. Since there were 25 microneedles on each chip, there were in total 100 microneedles on 4 chips in each group. After the drawing process, the results for each

group were counted and converted as the ratio on a single 5×5 array for an average. **Table 2.1** showed the observed data about the ratio of formed individual maltose tips over the formed clustered tips in these 48 samples. We concluded that individual maltose tips were successfully derived from samples of microtubes with the height beyond 350μm and the spacing larger than 900μm. As a result, we prepared many samples of SU-8 microtubes of 350μm height and 1000μm spacing for further maltose integration experiment in our study.

2.1.2.2 Mechanical Strength of the Microneedles

To ensure both the adequate adhesion property between the maltose tip and SU-8 microtubes, and the sufficient stiffness of the SU-8 microtubes for successful penetration, the mechanical strength of microneedles was studied. As shown in **Figure 2.6** (a), Instron Microtester 5848 (Instron, USA) was used for the stiffness testing. A typical result was shown in **Figure 2.6** (b). During the testing, the breakage of microneedles only occurred at the interface when the exerting load was larger than the threshold value. However, the SU-8 microtubes were strong enough to stand the pressure. After characterization of 20 samples, the average threshold value was 7.36±0.48N for the microneedles (300μm at microneedle base and 1000μm high). Since the minimal force required for a successful penetration was reported to be less than 1 N with the similar microneedle dimension[64], the device was reliable during the penetration process.

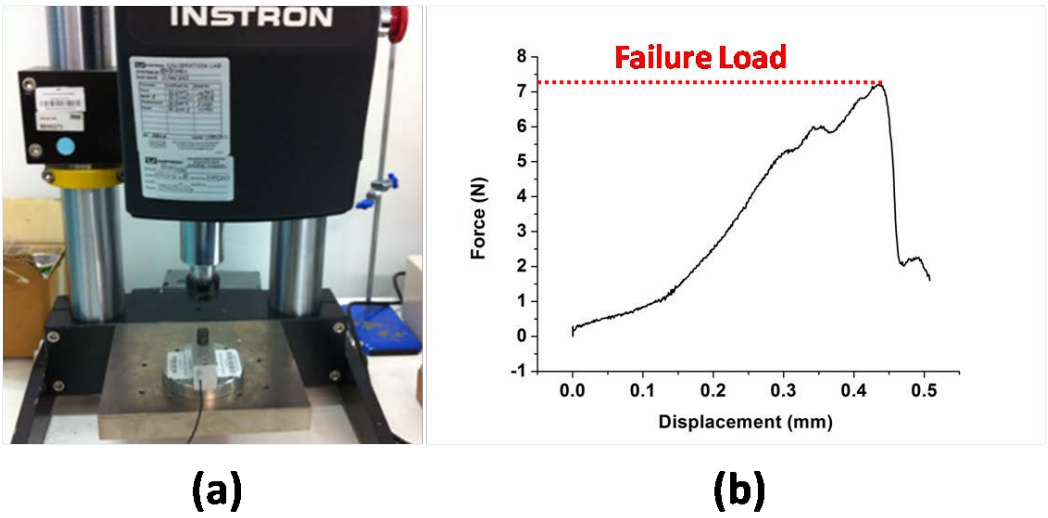

Figure 2.6 (a) Testing setup for the microneedle mechanical testing. (b) A typical microneedle stiffness testing result

2.1.2.3 Characterization of Penetration

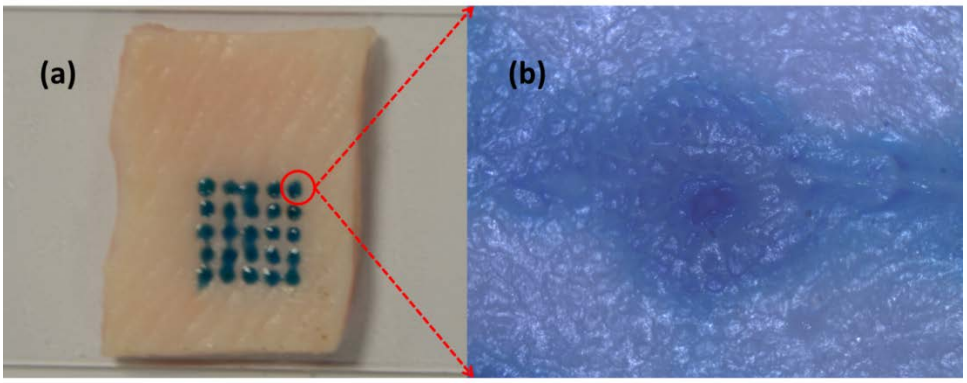

Figure 2.7 Penetration testing results on the porcine cadaver skin.

Figure 2.7 (a) shows the insertion result of a 5×5 microneedles array into a porcine cadaver skin. After the insertion, maltose tips were rapidly dissolved once inserted in the tissue. Methylene blue was added into the maltose for inspection purpose. Ten minutes after insertion, 25 blue traces were easily found, which matched the pattern of the microneedle array. The optical microscope image in **Figure 2.7** (b) showed a hole perforated in the skin after we cleaned the dissolved maltose mixed with Methylene blue from the skin surface. During the insertion experiment, we had to avoid the shear force influence caused by deformed skin surface on the individual maltose tip in

order to get successful microneedle penetration for the whole array. We used precision stages to hold the microneedle device substrate and control the relative position of device substrate and skin sample.

2.1.2.4 Dissolving of Maltose Tips and Demonstration of Injection via SU-8 Microtubes

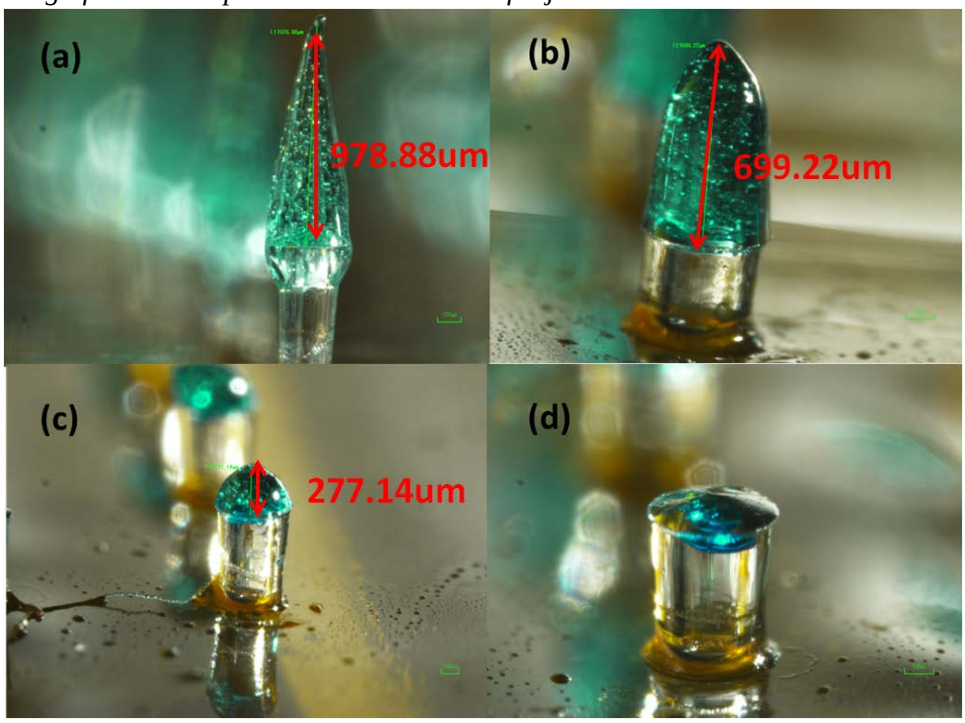

Figure 2.8 Maltose tips dissolving process. (a) The original sharp maltose tip. (b) Maltose tip after inserted into skin for 3minutes(c) 6minutes and (d) 9minutes.

In order to check whether the maltose tips could be dissolved once inserted in the tissue, four chips with the same maltose tips height were inserted into the skin and taken out one by one with 3 minutes interval. Maltose tips were gradually dissolved versus increased time as shown in **Figure 2.8**. After 9 minutes, the maltose tips were totally dissolved and the lumens of SU-8 microtubes were observed from the top view. Different from the traditional dissolvable needles which encapsulated drugs into the needles, this microneedle array was expected to allow large volume of drugs to pass through via the remaining SU-8 microtubes inside the skin.

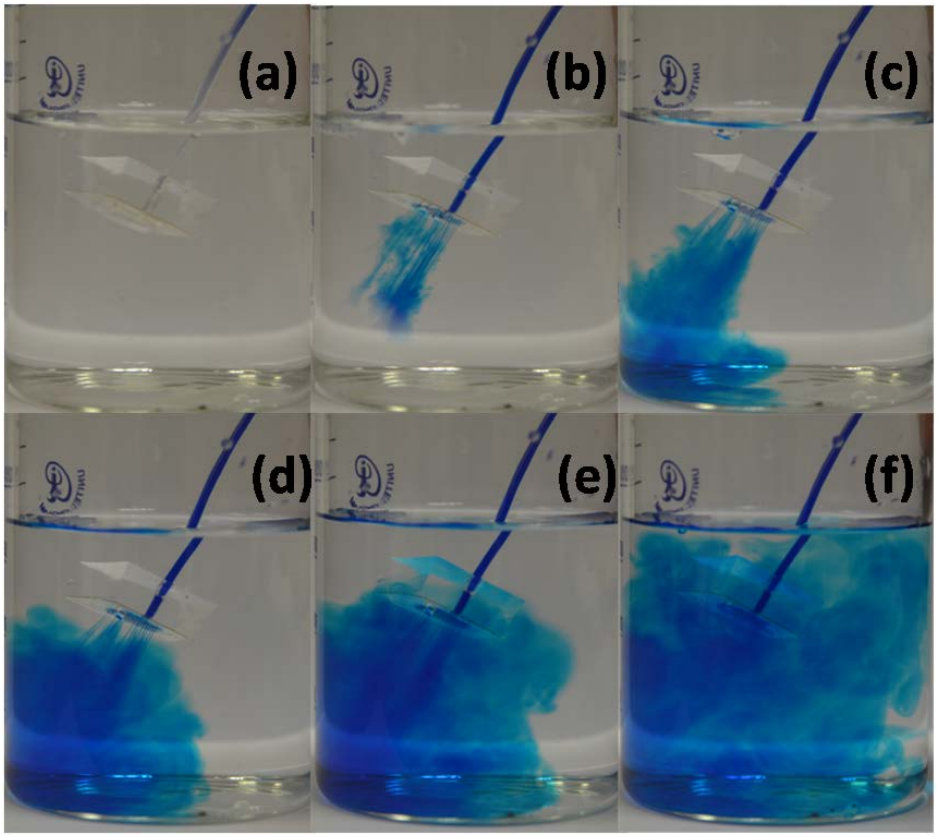

Figure 2.9 Microfluidic testing for SU-8 microtubes.

Moreover, blue dyed water was ejected through the lumens in SU-8 microtubes to the beaker containing fresh water such that we could demonstrate the hollow tubes formed in individual microtube during the fabrication process. This microfluidic testing was performed in fresh water as shown in **Figure 2.9**. Visual inspection of the ejection proved that there was no blockage inside the microtubes. Because of the good bonding quality between each layer, there was no obvious damage on the device in this experiment even though the syringe pump was increased to its maximum speed at 3.3mL/min for 6mL syringe.

2.1.2.5 Injection Florescent Solution into Skin Sample

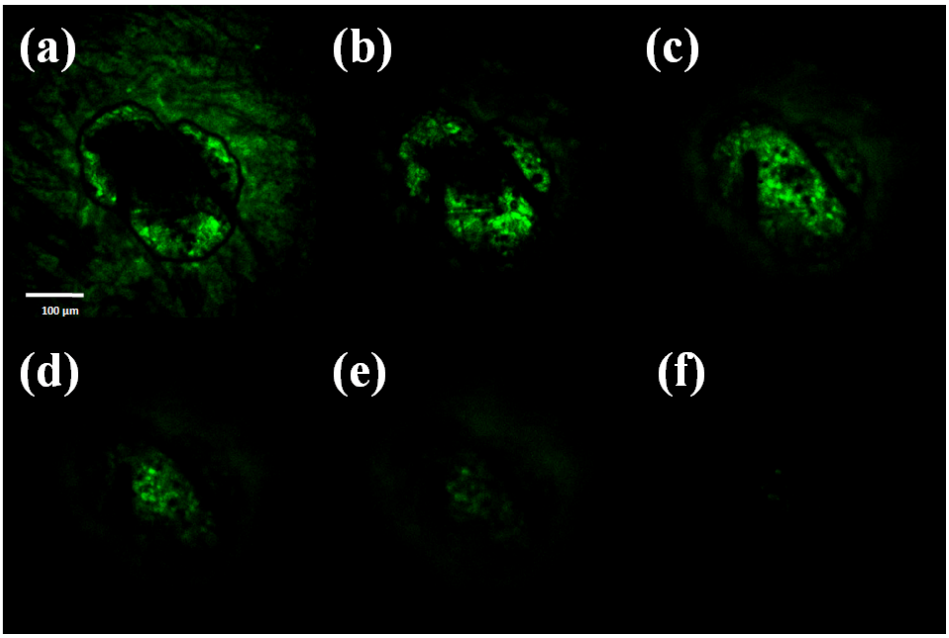

Figure 2.10 Images of confocal microscopy of the site where one microneedle inserted shows that the fluorescent solution is delivered into the tissue underneath the skin surface. Optical section depths are (a) 30µm, (b) 60µm, (c) 90µm, (d) 120µm, (e) 150 µm, (f) 180µm below the skin surface.

To verify that the drug solution can be delivered into tissue, a fluorescent solution was delivered through the SU-8 microtubes after the pure maltose tips were dissolved. The representative results were then investigated via a confocal microscopy (**Figure 2.10**). The permeation pattern of the solution along the microchannel confirms the solution delivery results. The black area served as a control area without any diffused solution. In contrast, the tissues stained by fluorescence illustrated the diffused area. The focus depth was up to 180µm with the interval of 30µm. Since the microchannel was created by the conical maltose tips, the diameter of the microchannel decreased as the focus depth increases. The following diffusion area was dependent on the microchannel dimension and also decreased accordingly.

2.2 Double Drawing Lithography Technology for Making Flexible Microneedle Patch with Lower Breakage Risk

Even though the microneedles device with dissolving tips enables a large volume delivery of big molecular drugs, in practical experiments it is found that the planar shear force induced by skin deformation may break the microneedles device from the interface between SU-8 microtubes and maltose tips. In order to solve this problem, we propose an optimized design for the microneedles strucutre. The SU-8 microtubes are fabricated into beam stuctures. Gaps between these beams act as anchors to reinforce the mechanical strength of the interfaces, which avoids microneedles beakage under planar shear force. The standard drawing lithography technology demonstrated before requires that the drawing frames need to be regular cylinders, which is not proper for our devices. To solve the problem, the optimized double drawing lithography is developed to create sharp SU-8 tips on the top of four SU-8 pillars for penetration purpose. Drugs can flow through the sidewall gaps between the pillars and enter into the tissues.

2.2.1 Design and Fabrication

An array of 3×3 SU-8 supporting structures was patterned on a 140 μm thick, 6mm×6mm SU-8 membrane (**Figure 2.11** (a)). Each SU-8 supporting structure included four SU-8 pillars and was 350 μm high. The four pillars were patterned into a tube like shape on the membrane (**Figure 2.11** (b)). The inner diameter of the tube was 150 μm, while the outer diameter was 300 μm. SU-8 needles of 700 μm height were created on the top of SU-8 supporting structures to ensure the ability of transdermal perforation. Two PDMS layers were bonded with SU-8 membrane to form a sealed chamber for storing drugs from the connection tube. Once the microneedles penetrated into the tissue, drugs could be delivered into the body through the sidewall gaps between the pillars (**Figure 2.11** (c)).

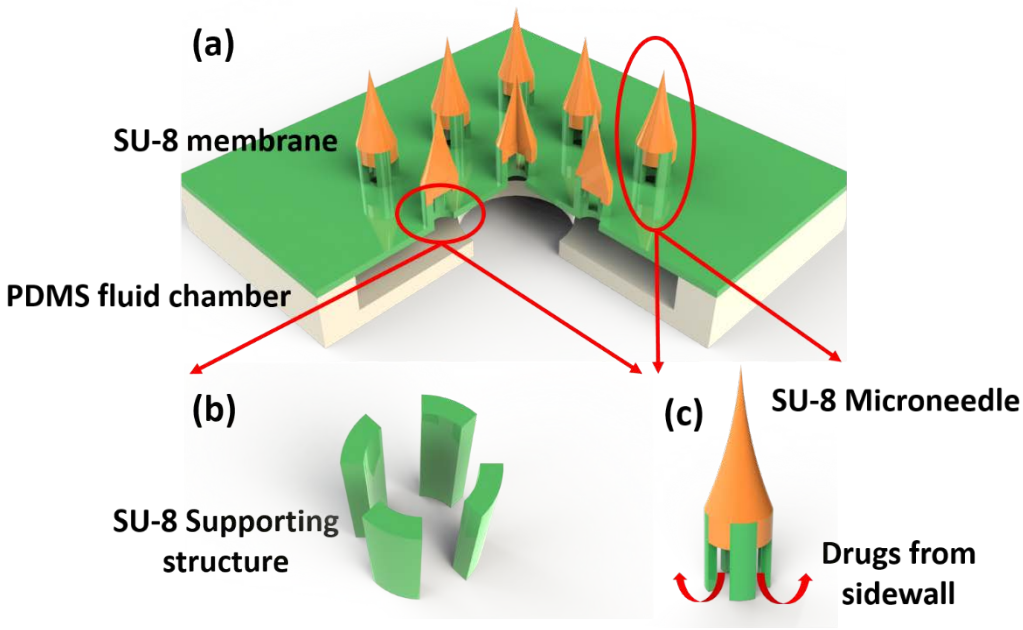

Figure 2.11 Schematic illustration of the SU-8 microneedles. (a) Overview of the whole device; (b) SU-8 supporting structures made of 4 SU-8 pillars; (c) Enlarged view of a single SU-8 microneedle.

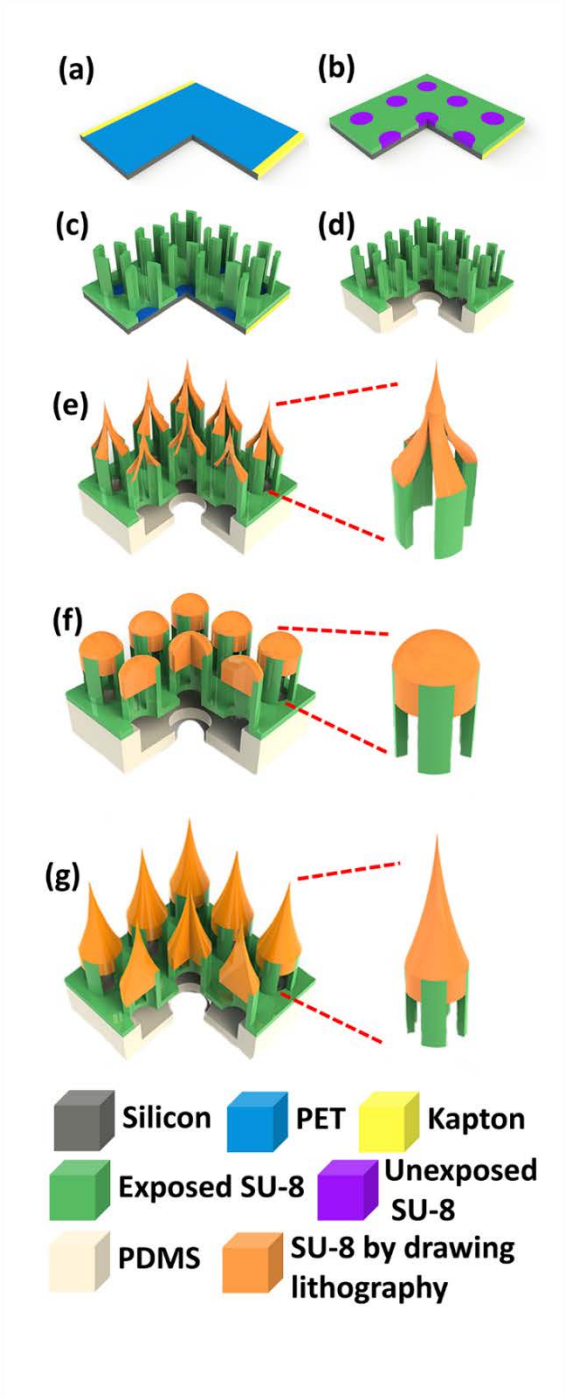

Figure 2.12 Fabrication process for SU-8 microtubes. (a) Attaching a PET film on the Si substrate; (b) Exposing the first layer of SU-8 membrane without development; (c) Depositing and patterning two continuous SU-8 layers as sidewall pillars; (d) Releasing the SU-8 structure from the substrate and bonding it with PDMS; (e) Drawing hollowed microneedles on the top of supporting structures; (f) Baking and melting the hollowed microneedles to allow the SU-8 flow in the gaps between pillars; (g) Drawing second time on the top of the melted SU-8 flat surface to get microneedls.

The fabrication process of SU-8 microneedles is shown in **Figure 2.12**. The SU-8 supporting structure is fabricated as the same method of SU-8 microtubes fabrication shown before (**Figure 2.12** (a)-(c)). However, since the frame used to conduct drawing process in present study is a four-pillars structure rather than a microtube, the conventional drawing process can only make a hollowed tip but not a solid tip structure (**Figure 2.13**). This kind of tip was fragile and could not penetrate skin in practical testing process. To solve the problem, we developed an innovative double drawing lithography process. After bonding released SU-8 structure with PDMS layers (**Figure 2.12** (d)), we used it to conduct first time stepwise controlled drawing lithography and got hollowed tips (**Figure 2.12** (e)). After the hollowed tips were formed in the first step drawing process, the whole device was baked on the hotplate to melt the hollowed SU-8 tips. Melted SU-8 reflowed into the gaps between four pillars and the tips became domes (**F Figure 2.12** (f)).

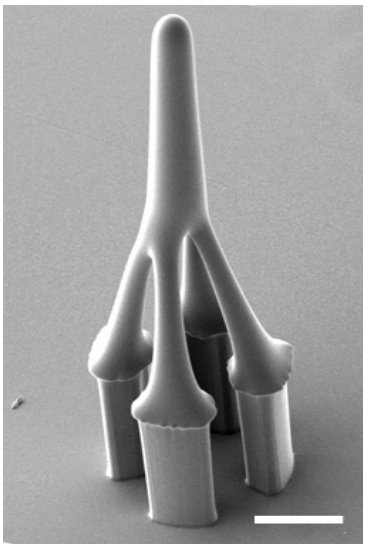

Figure 2.13 A hollowed SU-8 microneedle fabricated by single drawing lithography technology (Scale bar is 100 μm).

Then a second drawing process was conducted on the top of melted SU-8 to form sharp and solid tips (**Figure 2.12** (g)). The final fabricated device is shown in **Figure 2.14**.

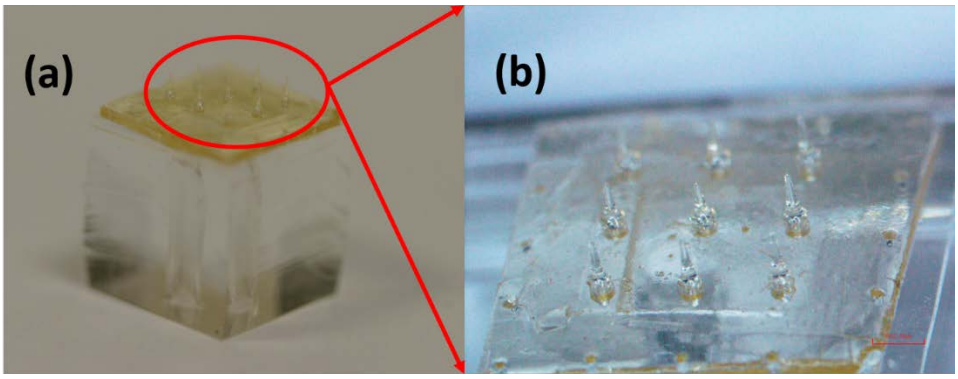

Figure 2.14 Optical images for the SU-8 microneedle patch.

2.2.2 Characterization for Microneedles Fabricated by Double Drawing Lithography Technology

During the double drawing process, as long as the heated time and temperature were controlled, the SU-8 flow-in speed of SU-8 inside the gaps could be precisely determined. The relationship between baking temperature and flow-in speed was studied. As shown in **Figure 2.15**, the flow-in speed is positive related to the baking temperature. The explanation for this phenomena is that the SU-8's viscosity decreases when the baking temperature increases. When the baking temperature is larger than 120 °C, the flow-in speed will increase sharply. But if the baking temperature is higher, the SU-8 will reflow in the gaps too fast, which makes the flow-in depth hard to be controlled. There is a high chance that the whole gaps will be blocked and no drugs can flow through these gaps any more. Considering that the total SU-8 supporting structure is only 350 μm high, we choose 125 °C as baking temperature for proper SU-8 flow-in speed and easier SU-8 flow-in depth control.

To ensure the adequate stiffness of the SU-8 microneedles in vertical direction, mechanical testing was conducted as described before. As shown in **Figure 2.16**, the vertical buckling force was as much as 8.1N, which was much larger than the reported minimal required penetration force. However, in previous practical testing experiments, even though the microneedles were strong enough in vertical direction, the planar shear force induced by skin deformation might also break

the interface between SU-8 pillars and top tips. In our new device with four pillars supporting structure, the SU-8 could flow inside the sidewall gaps between the pillars to form anchors. These anchors could enhance microneedles' mechanical strength and overcome the planar shear force problems. Moreover, the anchors strength could be improved by controlling the SU-8 flow-in depth. **Figure 2.17** shows that the flow-in depth increases when the baking time increases as the baking time increases at 125 °C. The corresponding planar buckling force can be improved to be larger than 1 N by increasing flow-in depth (**Figure 2.16** (b)). Some spacing in sidewall gaps at bottom is kept on purpose for drugs flow, hence the flow-in depth is chosen as 200 μm.

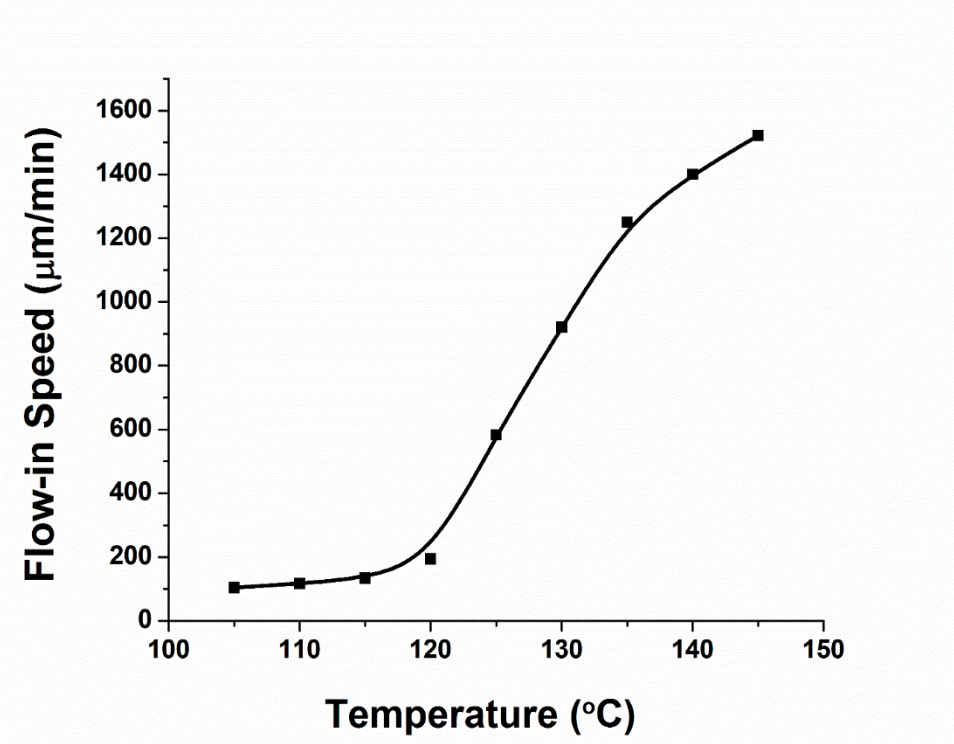

Figure 2.15 The relationship between flow-in speed and baking temperature.

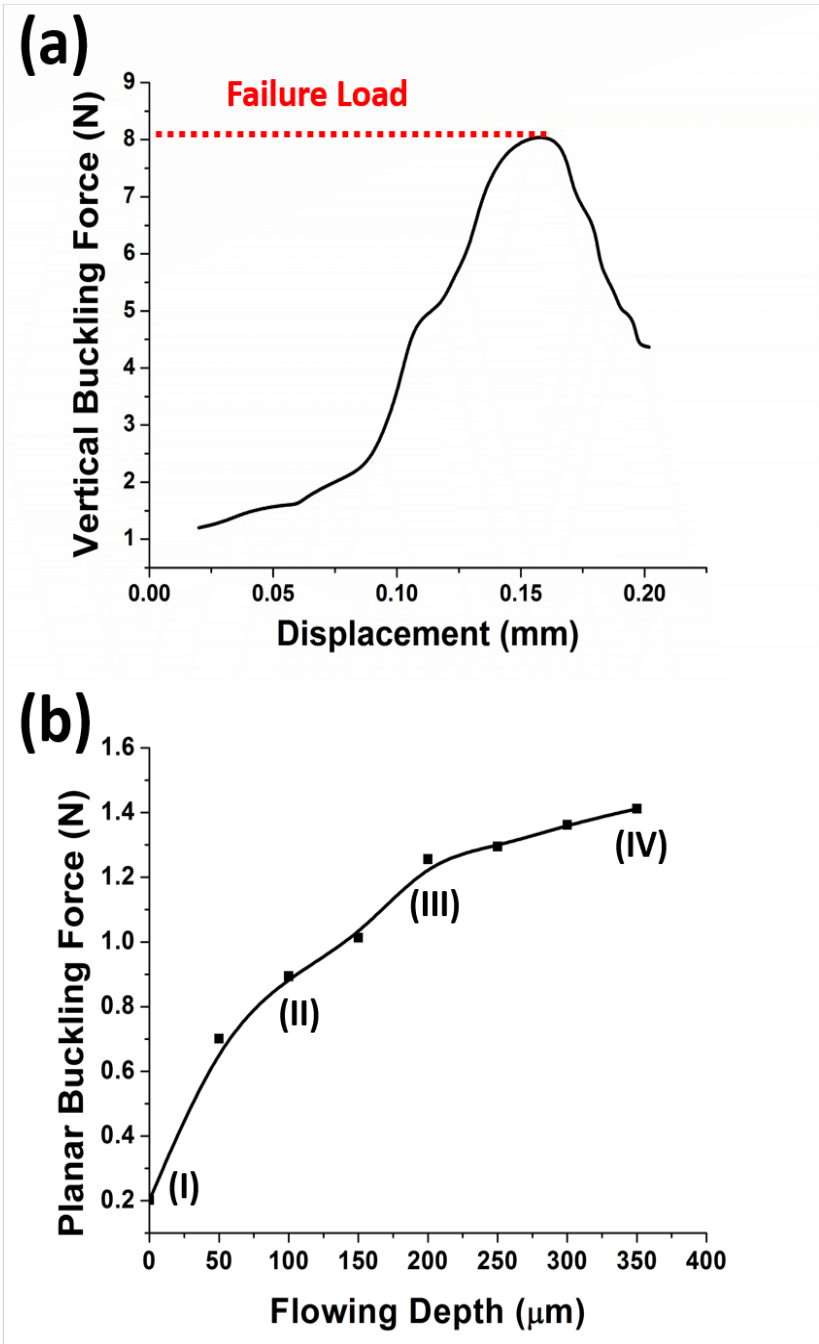

Figure 2.16 (a) Measurement of the vertical buckling force. (b) The planar buckling force varies under different flow-in depth (I, II, III, IV corresponding to the certain images in **Figure 2.17**).

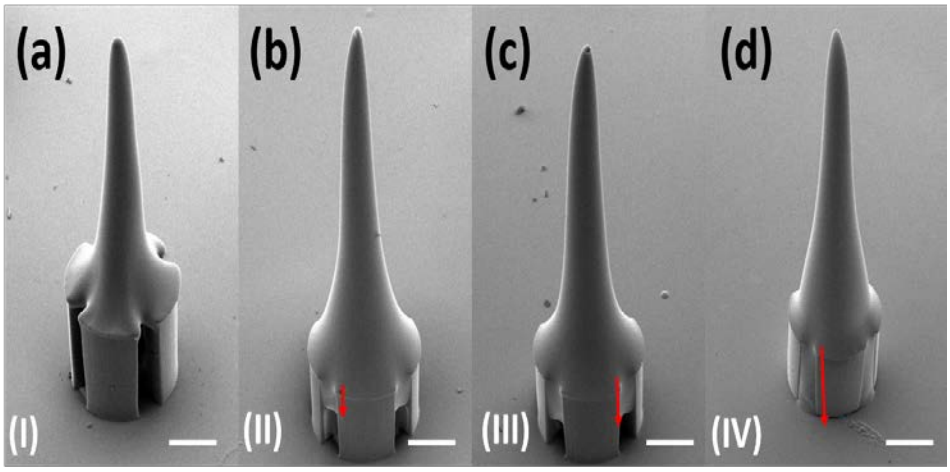

Figure 2.17 Different flow-in depth inside the gaps between SU-8 pillars. (a) 0 µm; (b) 100 µm; (c) 200 µm; (d) 350 µm (Scale bar is 100 µm).

The penetration capability of the SU-8 microneedles is also characterized by conducting the insertion experiment at porcine cadaver skin. 10 microneedles devices were tested and all of them were strong enough to be inserted into the tissue without any breakage. Histology images of the skin at the site of one microneedle penetration were derived to prove that the sharp conical tip was not broken during the insertion process (**Figure 2.18**). It also shows penetration evidence because the shape of the microchannel is the same as the sharp conical tip.

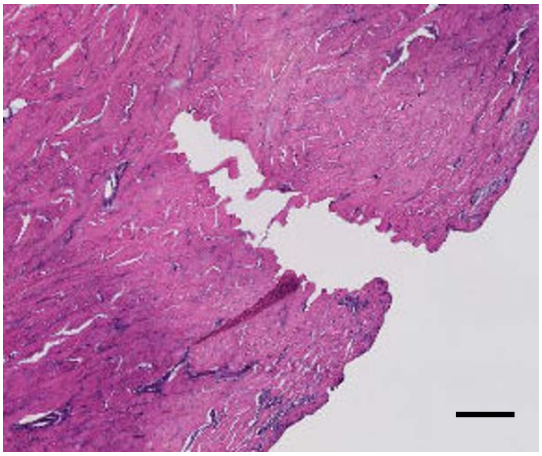

Figure 2.18 Histology image of individual microneedle penetration (Scale bar is 100 µm).

Due to the uneven surface of deformed skin, there is always tiny gap happened between tips of some microneedles and local surface skin. The microneedles could not be entirely inserted into the tissue. Drugs might leak to the skin surface through the sidewall gaps under certain driven pressure. Hydrogel absorption experiment was conducted to quantify the delivery rate (i.e., the ratio of solution delivered into tissues in the total delivered volume) and to optimize the delivery speed. Gelatin hydrogel was prepared by boiling 70 mL DI (Deionized) water and mixing it with 7g of Knox^{TM} original unflavored gelatin powder. The solution was poured into petri dish to 1cm high. Then the petri dish was put into a fridge for half an hour. Gelatin solution became collagen slabs. The collagen slabs were cut into 6mm×6mm sections. A piece of fully stretched Parafilm (Parafilm M, USA) was tightly mounted on the surface of the collagen slabs. This parafilm was used here to block the leaked solution further diffused into the collagen slab in the delivery process. Then the microneedles were penetrated the parafilm and went into the collagen slab. Controlled by a syringe pump, 0.1 mL 0.5mg/mL glucose solution was delivered into the collagen slab under different speeds. Methylene Blue (Sigma Aldrich, Singapore) was mixed into the solution for better inspection purpose (**Figure 2.19** (a)). Then the collagen slabs were digested in 1mg/mL collagenase (Sigma Aldrich, Singapore) at room temperature (**Figure 2.19** (b)). It took around 1h that all the collagen slabs could be fully digested (**Figure 2.19** (d)). The solution was collected to measure the glucose concentration with Glucose Detection kit (Abcam, Singapore). Briefly, both diluted glucose standard solution and the collected glucose solution were added into a series of wells in a well plate. Glucose assay buffer, glucose enzyme and glucose substrate were mixed with these samples in the wells. After incubation for 30 minutes, their absorbance were examined by using a microplate reader at a wavelength of 450nm. By comparing the readings with the measured concentration standard curve (**Figure 2.20** (a)), the

glucose concentration in the hydrogel, the glucose absorption rate in the hydrogel and the solution delivery rate by microneedles could be measured and calculated. As shown in **Figure 2.20** (b), when the delivering speed for a single microneedle increased from 0.0001mL/min to 0.002mL/min, the glucose absorption rate also increased. Most of the glucose solution from microneedles could go into the hydrogel. The delivered rate could be as high as 71%. The rest solution leaked from sidewall gaps and blocked by parafilm. However, when the delivered speed for a single microneedle was larger than 0.002mL/min, the hydrogel absorption rate was saturated. More and more solution could not go into the hydrogel but leak from the sidewall gaps. Then the delivered rate decreased. Therefore, 0.002ml/min was chosen as the optimized delivery speed for the microneedle. However, due to the nature of transdermal drug delivery which the drug is not directly injected into the vein, the absorption rate of skin will has a certain limitation. Currently the maximum skin absorption rate by microneedle is 16mg/day[143] by a microneedle array of 480 microneedles. Thus the maximum delivery rate of each microneedle should be around 33μg/day. Considering the density of the drug solution will be quite close to the density of water, thus the maximum delivery rate for an individual microneedle should be 0.023μL/min. Thus the maximum deliver rate of the microneedle we fabricated is far more than the maximum absorption rate of skin. It means in real application, only a very low deliver rate is required.

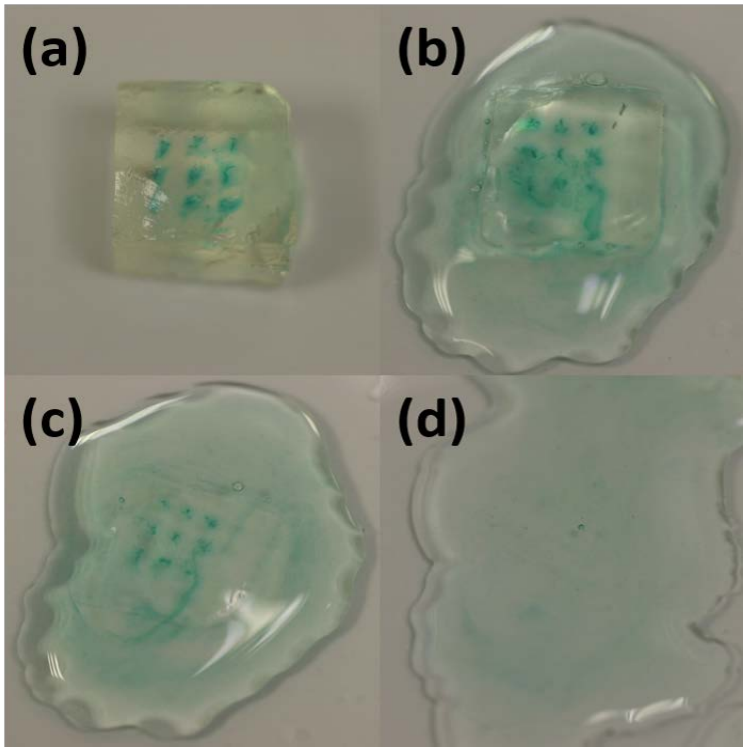

Figure 2.19 Glucose solution could be delivered into the hydrogel and the collagen stabs were dissolved by collagenase.

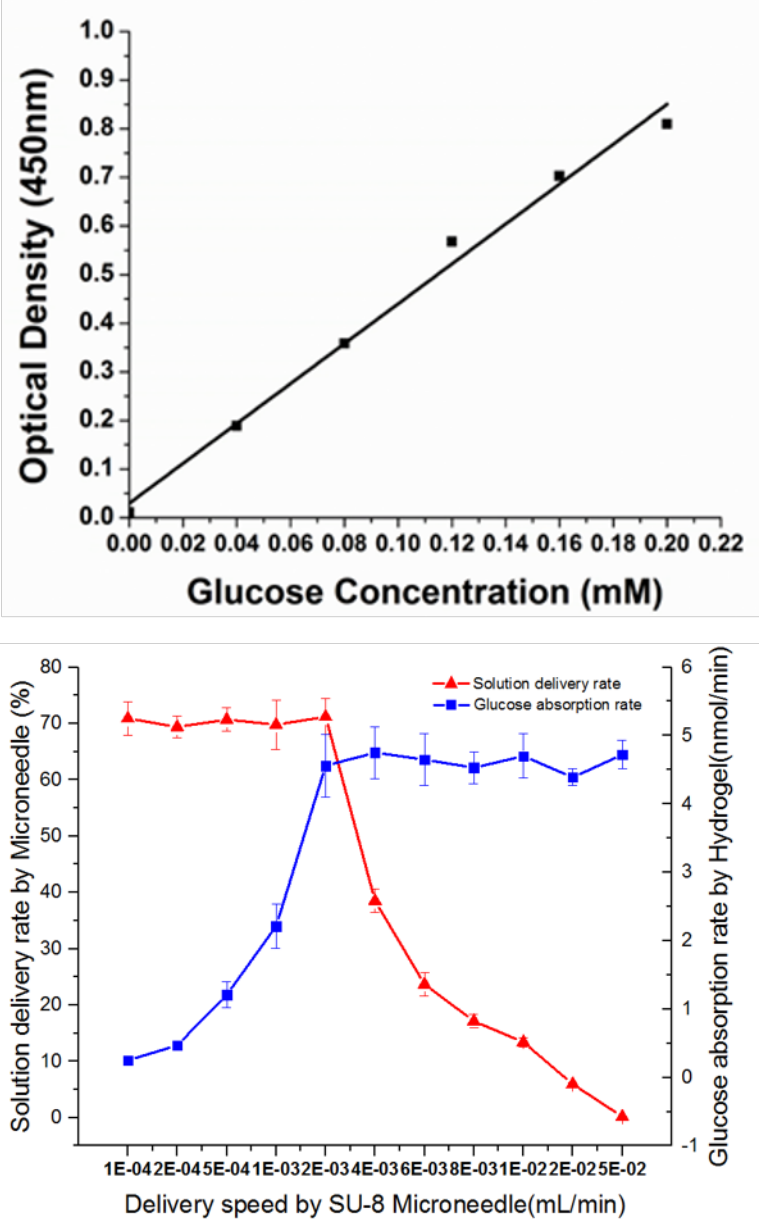

Figure 2.20 (a) Standard curve for glucose detection; (b) Glucose absorption rate and solution delivery rate in a single needle corresponding to different delivery speed.

2.3 Conclusion

Based on the drawing lithography technology, we designed and developed two different kinds of flexible microneedle patches. Both of them are hollow microneedles which can be used for the delivery of drugs with big molecules. The flexible microneedle patch with dissolvable sharp tips is able to deliver drugs with large volume while four beams structure with SU-8 tips enhance the

microneedle stiffness. The proposed fabrication process is scalable, reproducible and inexpensive. Penetration testing and diffusion testing prove their function to deliver drugs to the tissues under the skin. In the hydrogel absorption experiment, by controlling the delivery speed under 0.002mL/min per microneedle, the delivery rate provided the microneedle is as high as 71%.

Chapter 3 Polymer Microneedle Array Integrated with CNT Nanofilter for Selective Drug Delivery

Currently none of microneedles developed have integrated functions for controlled drug release with mechanical valves such as CNT nanofilters. However, such a drug control releasing function is desirable for long term drug delivery and could expand the applications of microneedles. In this chapter, a unique process which utilizes a membrane based vertically grown carbon nanotubes (CNTs) as nanofilters for mass transport study is presented first. By leveraging the double drawing lithography process, the CNT nanofilters are integrated with the SU-8 microneedles. With the CNTs nanofilters, the delivery of drugs of different molecular dimensions could be controlled by pressure and an electric field.

The design of the microneedle array integrated with CNT nanofilters is shown in **Figure 3.1**. An array of SU-8 microneedles was patterned above a SU-8 membrane(**Figure 3.1** (a)). Every SU-8 microneedle has two parts: four-beam sidewalls at the bottom and a sharp tip at top as shown in **Figure 3.1** (c). The four-beam sidewalls (brown parts in **Figure 3.1** (a)) are patterned by photo lithography. The gaps along the sidewalls are the outlets of the microneedles. The sharp tips above the four-beam structure (green parts in **Figure 3.1** (a)) are assembled and patterned by double drawing lithography. Above them, a layer of gold surface electrode was deposited onto the whole surface. This surface electrode allows us to apply an electric field in the test. Inside the four-beam structures, vertical grown CNT bundles (black parts in **Figure 3.1** (a)) were embedded in the SU-8 membrane to form the CNT nanofilters. Fig. 1(d) shows the SEM image of one CNT bundle.

Underneath the SU-8 membrane, there a SU-8 chamber layer to support the SU-8 membrane layer and form a solution chamber. PDMS layers (the blue part in **Figure 3.1** (a)) are bonded to the SU-8 chamber layer for tube connection in the test. Solution could be loaded in the chamber under the CNT bundles, pass through the CNT bundles and finally through the SU-8 microneedles into the tissue. The optical image of the microneedle array with the gold surface electrode is shown in **Figure 3.1** (b). For applying the electric field across the CNT nanofilters in the test, one electrode will be bonded onto the surface electrode and another electrode will be inserted into the PDMS chamber as shown in **Figure 3.2**. When the solution is loaded in the drug reservoir and flow through the CNT nanofilters, two electrodes would be connected by the solution and an electric field is generated across the CNT nanofilters.

Before the integration of microneedle with CNT nanofilters, we made a detailed study and characterization of the CNT nanofilters first.

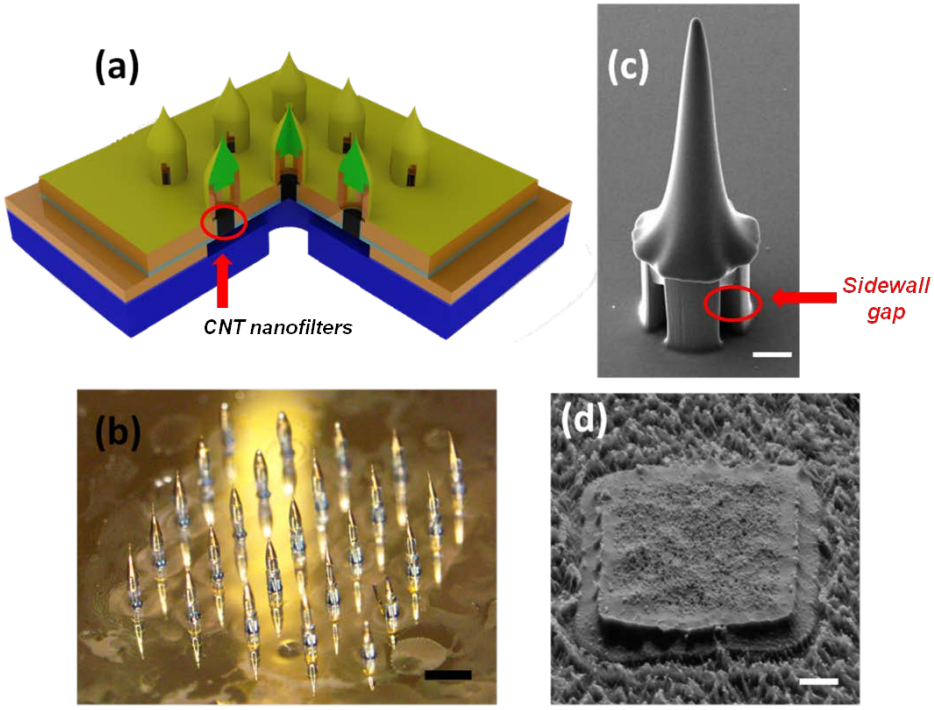

Figure 3.1 (a) 3D schematic drawing of the microneedle device integrated with CNT nanofilters; (b) Optical image of the microneedle array with gold surface electrode, scale bar is 1000μm; (c) SEM image of single SU-8 microneedle with four-beam sidewalls and a sharp tip, scale bar is 80μm; (d) SEM picture of a CNT bundle embedded inside the microneedle, scale bar is 10μm.

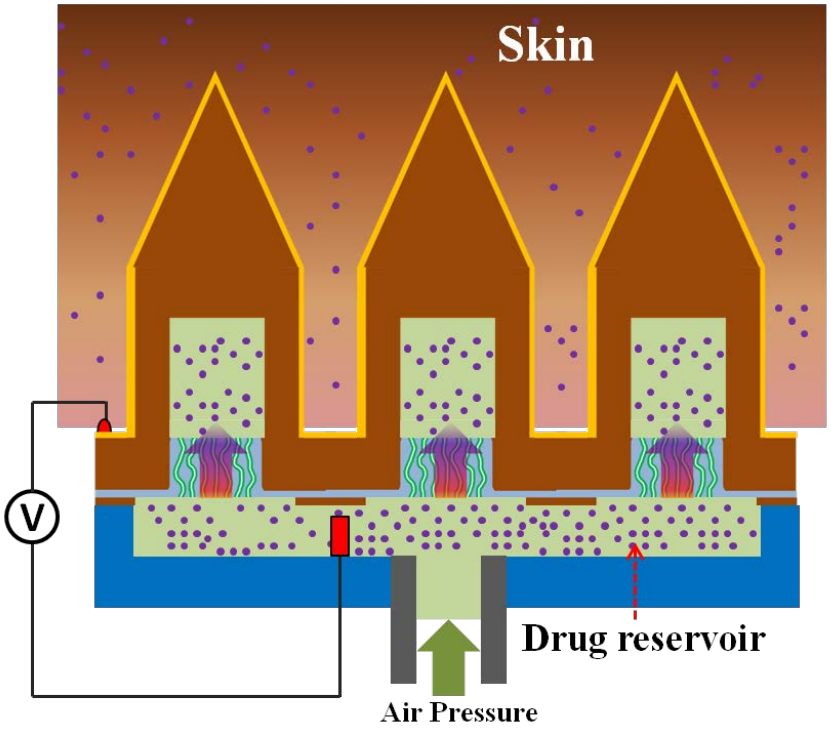

Figure 3.2 Working principle of the microneedle array integrated with CNT nanofilters for transdermal drug delivery.

3.1 Development of CNTs Nanofilters Using Patterned Array of Vertically Grown Carbon Nanotubes

3.1.1 Structure and fabrication process of the CNTs nanofilters

Figure 3.4 shows the experimental steps for the fabrication of membrane based nanofilters shown in **Figure 3.3** using patterned CNT bundles. A substrate with arrays of vertically aligned CNTs patterns (**Figure 3.5** (a)) is first reinforced by CVD grown parylene (Scheme 1,step 1) so that parylene molecules are infiltrated into the intertube space (**Figure 3.5** (b)). The parylene layer together with patterned CNTs array is then peeled off from the substrate and the catalyst layer on the backside is etched off by oxygen plasma (Scheme 1, step 2). The backside catalyst layer is shown in **Figure 3.5** (c). After oxygen plasma, the catalyst layer is etched away (**Figure 3.5** (d)). The released parylene layer is then attached to a prebaked SU-8 substrate. The Su-8 substrate is baked and cooled to achieve the bonding with parylene (**Figure 3.4**, step 3). Vertical microfluidic

channels under CNTs bundles shown in **Figure 3.5** (b) are patterned by stand lithography (**Figure 3.4**, step 4). The bottom side of the CNTs bundle is open. The top side of the CNTs bundles are open by oxygen plasma etching (**Figure 3.4**, step 5). **Figure 3.4** (d) shows the CNTs bundle with top open. **Figure 3.4** (e) shows the 3D schematic drawing of the open CNTs bundle for a better understanding. The whole parylene layer is etched off due to no mask in the etching process. The parylene sidewall is remained due to the anisotropic property of plasma etching. These parylene sidewalls provide the bonding which make the CNTs bundles be fixed onto SU-8 substrate. Two PDMS layers are further bonded at the bottom of the device for tubing and tests (**Figure 3.4** (a) and (b)). The detailed fabrication process can be found in Appendix 1.

The bonding strength between parylene and SU-8 is very strong. The detachment between parylene and substrate[1] will not occur here. Because of that we use CNT bundles of small patterns instead of whole CNT forests of large area, the CNT forests will not break by applying pressure. These two differences make our device could stand high pressure.

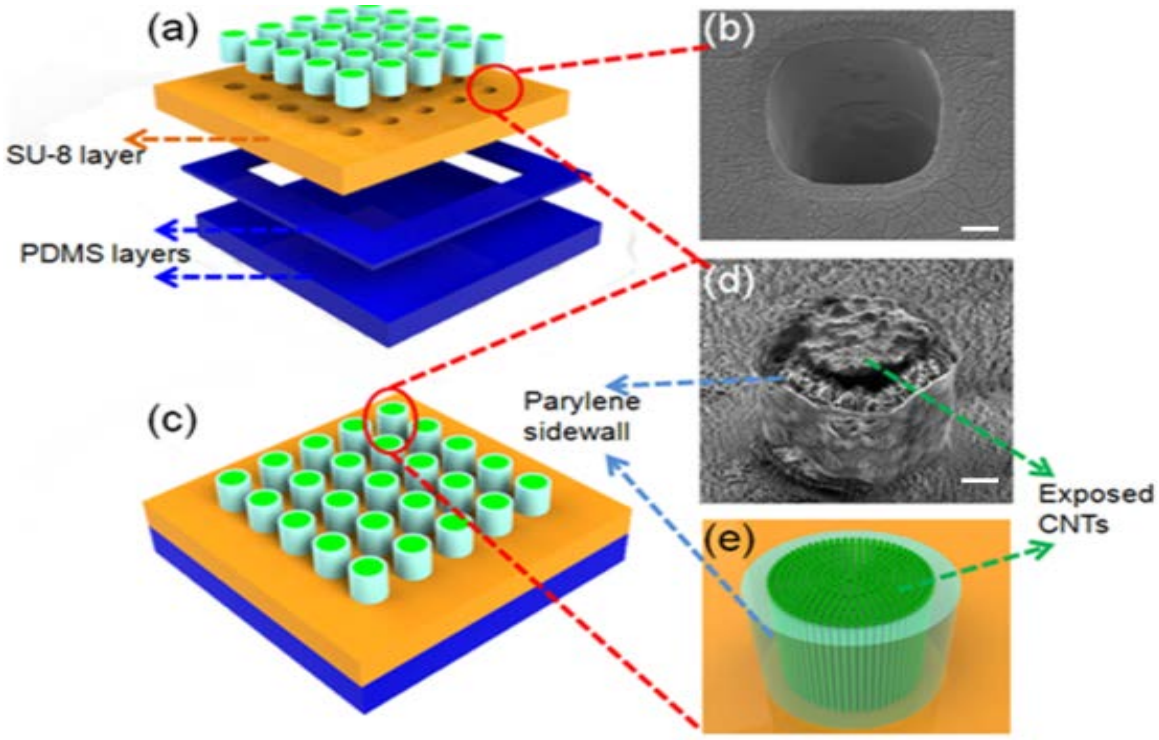

Figure 3.3 (a) 3D schematic drawing of detailed layer structure of the devices.; (b) SEM picture taken from the back side of the SU-8 layer showing a hole under a CNTs bundle on SU-8 layer. (c) 3D Schematic drawing of the device (d). SEM picture of the CNTs bundle with top end open; (e) 3D schematic drawing of the CNTs bundle with top end open. The scale bars for (b) and (d) are 10 um.

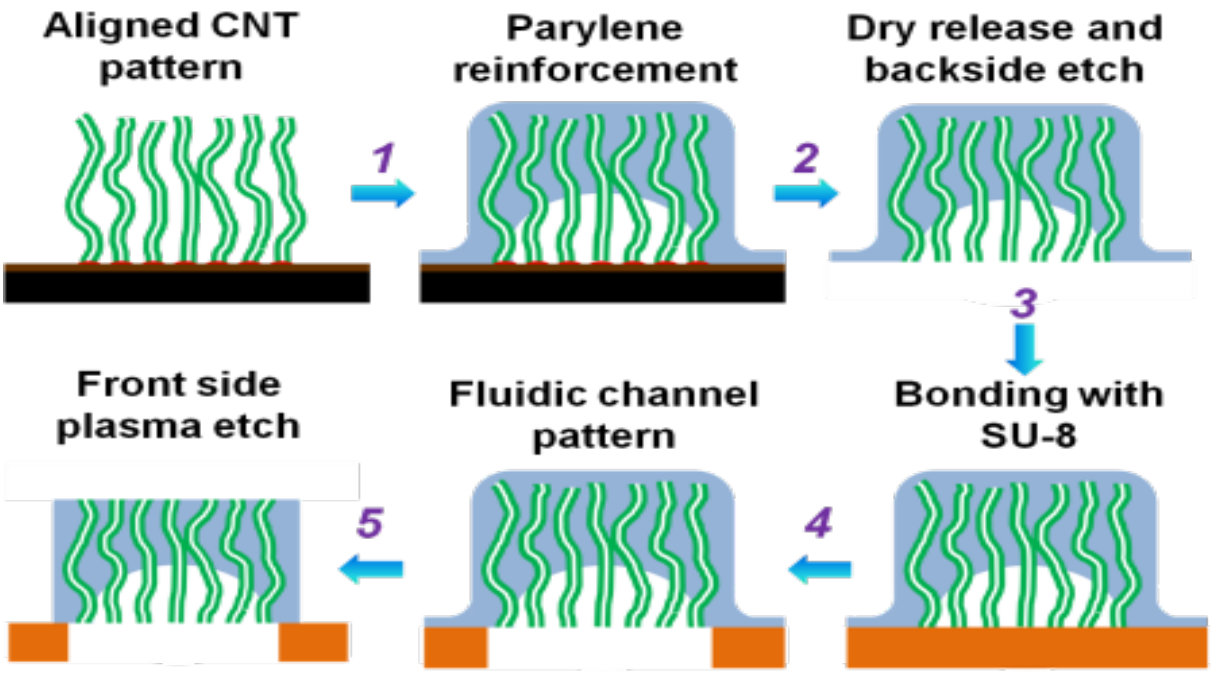

Figure 3.4 Schematic representation of the experimental steps showing the fabrication of membrane based nanofilters.

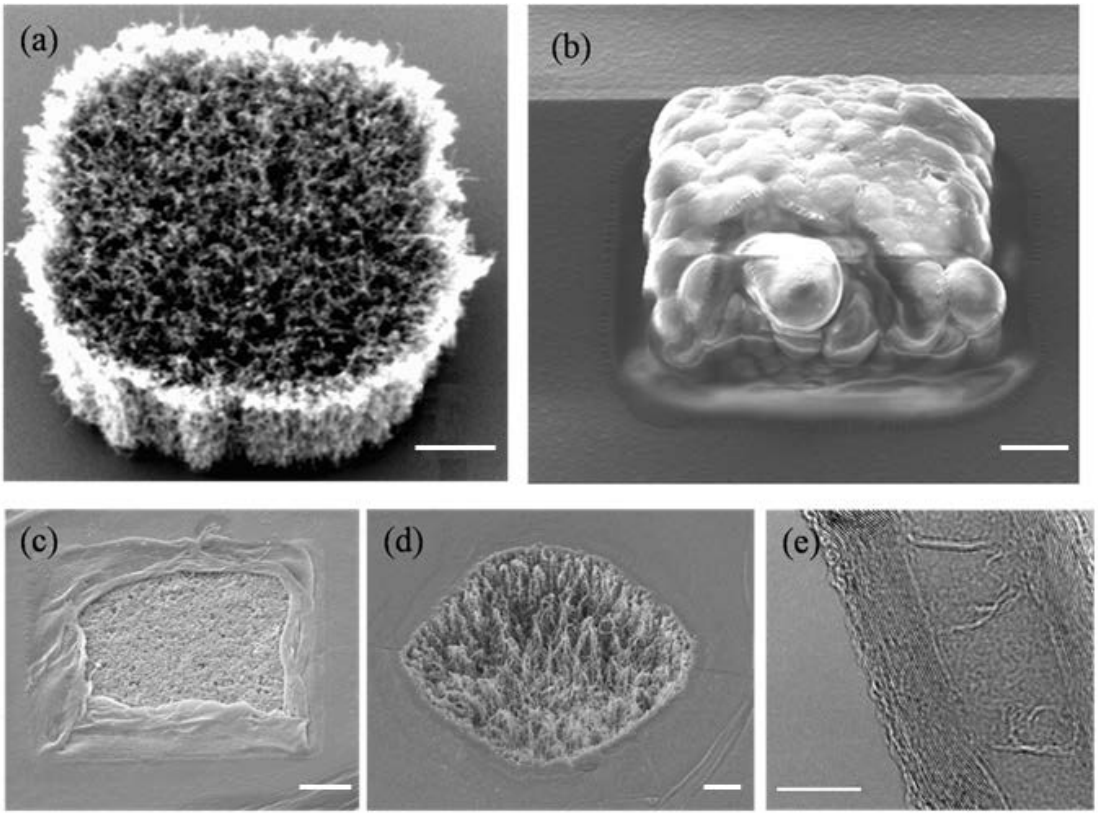

Figure 3.5 (a) An individual CNTs bundle grows from catalyst layer, the diameter of the CNTs bundle is 50 μm, the height of the CNTs bundle is 50 μm; (b) An individual CNTs bundle reinforced

by parylene, the thickness of the parylene layer is 10 μm; (c) catalyst layer seals the bottom of the CNTs bundle; (d) The catalyst layer is etched by oxygen plasma; (e) TEM picture showing the inner diameter of the CNTs is 10 nm; the scale bars for (a) to (d) are 10 um and the scale bar for (e) is 10nm.

3.1.2 Characterization of CNTs nanofilters

3.1.2.1 Ions transport test

The mass transport of ions and biomolecules of nanofilter samples of different dimension is measured by applying electric field and pressure based on the test setup in **Figure 3.6** (a).

A Ti electrode penetrated the PDMS layer and connected the solution inside the PDMS chamber. Bias could be applied via this electrode. Test solution of very small volume was pre-loaded in the device chamber and part of the tube. This preloading is necessary to get rid of the air in the device chamber and make the solution in touch with the surface of CNTs bundles. The tube connected the device with a syringe and a pressure sensor. The syringe could be driven by a syringe pump to give air pressure and the air pressure is calibrated by the pressure senor.

Based on our observation, the CNTs nanofilters are able to sustain under a pressure level of 40kPa, but for some samples, leakage between the interface of PDMS and SU-8 was detected at a pressure level higher than 25kPa. Thus, the pressure level was limited within 25kPa in our experiments. The device was loaded in the beaker. The liquid surface in the beaker should be kept lower than the exposed part of the electrode inserted in PDMS. This was to avoid the two electrodes being shorted by the solution connection. Another Ti electrode was immersed in the solution in the beaker.

The two electrodes were connected to a semiconductor characterization system (KEITHLEY 4200) which could apply bias and measure the current simultaneously. Resultant solution was sampled from the solution inside the beaker.

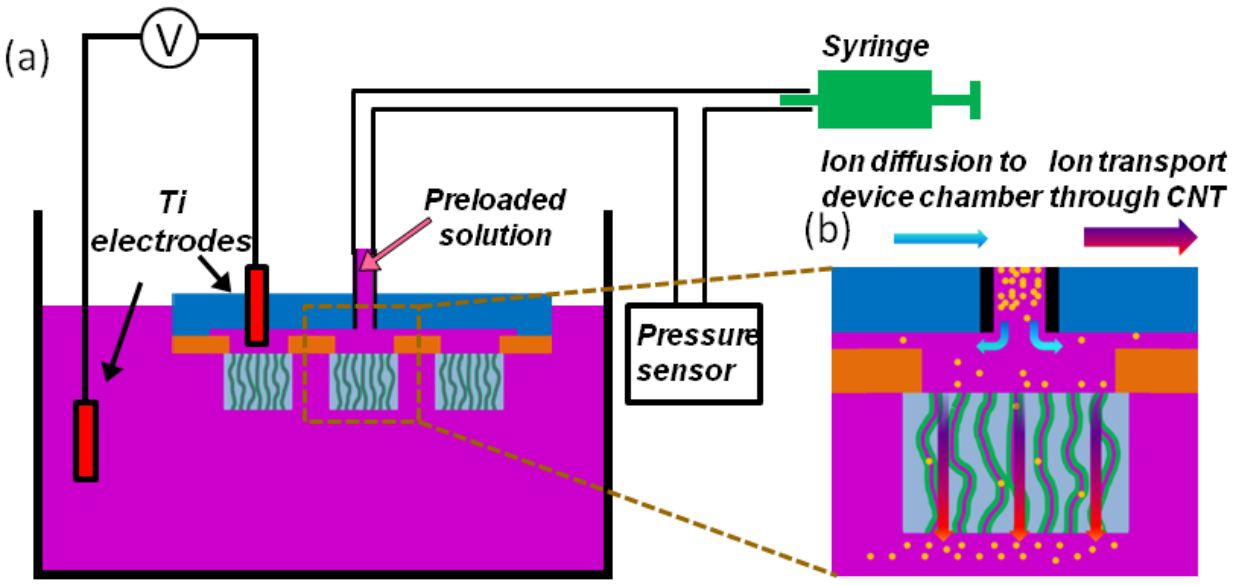

Figure 3.6 Test setup for applying electric field and pressure; (b) Schematic drawing of the ion diffusion and ion depletion in the device chamber.

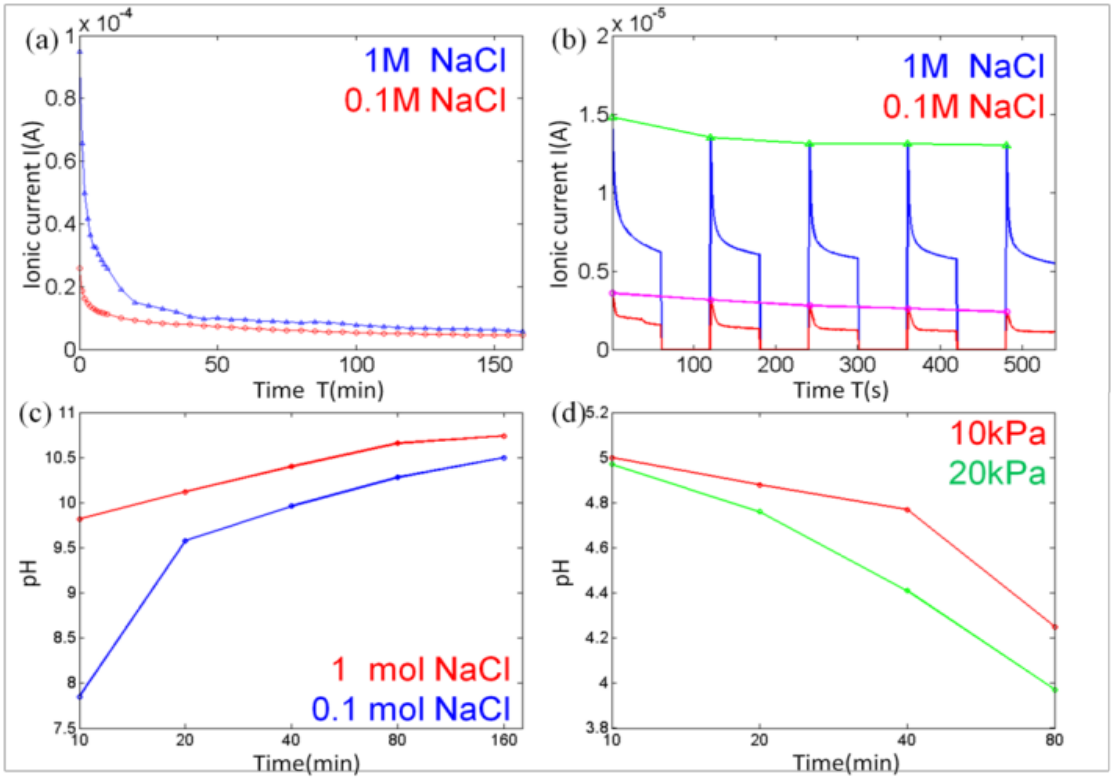

Figure 3.7 (a) The ionic current through the CNTs membranes as a function of time in different NaCl concentrations; (b) The ionic current as a function of time under square wave bias in different NaCl concentrations . The green line and pink line indicate the difference between peak values of ionic current. (c) The pH value of the NaCl solution with different concentrations as a function of time; (d) The pH value of the HCl solution under different driving pressure as a function of time.

In the study of driving ions by electric field, NaCl solution was loaded in both the beaker and the tube. The solution volume in the beaker was 60 ml and in the tube was about 0.2 ml. A bias of 5 V was applied between the two Ti electrodes for 160 min. The electrode in the beaker was grounded and the electrode in the tube was positively biased. No air pressure is applied. No obvious electrolysis of water is observed. Two concentrations of NaCl solution, 1mol/L and 0.1mol/L, were employed to study the relation between the ion concentration and ionic current. The experiments were carried out at room temperature (~26ºC). The solution in beaker was sampled for pH measurement at 10, 20, 40, 80 and 160 min. The change of ionic current was recorded as shown in **Figure 3.7** (a). The ionic current quick dropped down as a function of time. The peak values of the ionic current of NaCl concentration 0.1 mol/L and 1mol/L were 9.5×10^{-5}A and 2.4×10^{-5}A. The large peak value difference suggests that the main transport mechanism under electric field is electrophoresis[66]. The drop of the ionic current may due to two possible reasons. First, the change of pH value altered the property of the CNTs inner wall surface which enhanced the interaction between ions and CNTs inner wall surface. This pH value change was caused by electrolysis of NaCl solution. The reaction in beaker is :

$2NaCl+2H_2O+2e^-\rightarrow 2NaOH + H_2\uparrow+2Cl^-$;

so the solution will be alkaline and pH value will rise. And the reaction in the tube is:

$2NaCl+2H_2O\rightarrow 2Na^+ +HCl+HOCl+2e^-$;

so the solution will be acidic and pH value will drop. The change of the pH value is shown in **Figure 3.7** (c). The NaCl solution of higher concentration had a higher pH value which means a faster reaction rate. And the difference of pH value inside the beaker and tube increased with time. However, according to **Figure 3.7** (a), the ionic current tends to stabilize with time. So the change of the pH value should not be the reason for the drop of ionic current. It is also reported that the

pH value of the solution does not significantly affect the ionic current and the conductance of CNTs[65]. The second possible reason is the depletion of the ions at the PDMS chamber. The high peak values of the ionic currents stand for fast ion transport. This fast ion transport may cause depletions which cannot be compensated by the ion diffusion from other regions. As shown in **Figure 3.6** (b), the geometry of device chamber connecting to the CNTs bundles is very limited. One possible reason is that ions cannot efficiently diffuse from other places to this region when ions at this region quickly pass through the CNTs bundles. Then the depletion of the ion in the DPMS chamber causes the drop of the ionic current. We carried out an experiment to prove it. The 5 V bias was applied in a square wave mode with duty cycle of 1 min on and 1 min off. This square wave mode bias was applied for several cycles and the recorded ionic current is shown in **Figure 3.7** (b). The ionic current dropped when bias was on. When bias was not off, the solution in the device chamber got replenishment of ions by the diffusion from other regions. Thus, when bias was on again, the peak value of ionic current recovered to a certain level. But due to 1 min time duration was insufficient for the recovery of ion concentration in the device chamber to its initial value, the peak value of ionic current still had a slightly drop. The green line shows the drop of peak values from about 1.5×10^{-5}A to about 1.4×10^{-5}A for 1mol/L NaCl concentration.

In the study of driving ions by pressure, 0.2 ml 3.7% HCl solution was preloaded in the tube. 60 ml DI water was loaded in the beaker. Air pressure of 10kPa and 20kPa was applied for 80 min to study the relation between pressure and permeability with a zero biasing voltage. Solution in the beaker was sampled at 10, 20, 40 and 80 min. The pH value of solution samples was measured by pH meter (CORNING Pinnacle, Model: 530) as shown in **Figure 3.7** (d). The line of 20kPa pressure shows a greater pH value drop than that of 10kPa. At 80 min, the pH values of solution after applying 10kPa and 20kPa were 4.25 and 3.97. According to the definition of pH value:

pH=-log[H^+]; ([H^+] refers to the H^+ concentration.)

The ratio of H+ concentration is $[H^+]_{20kPa}/[H^+]_{10kPa}$ =104.25/103.97=1.9. The ratio of H^+ concentration was almost the same as the ratio of pressure level. This result suggests a linear relation between mass transport rate and pressure level, which is consistent with result reported[65].

3.1.2.2 Bio-molecules transport test

In the study of large molecule translocation through CNTs membrane, ss-DNA and Haemagglutinin were employed to study CNTs bundles' function of filter. The inner diameter of the CNTs in this study is 10 nm (**Figure 3.5** (e)). The ss-DNA whose cross sectional dimension is smaller than 10nm was expected to pass through CNTs membranes just by applying pressures. And Haemagglutinin, whose shape is like a cylinder and dimension is approximately 13.5 nm long that are larger than the inner diameter of the CNTs, was expected not to pass through CNTs membranes by applying pressure. The preparation of ss-DNA can be found in Appendix 2.

A medley of pressure and electric field driven method could drive ss-DNA through CNTs is reported[66]. In the experiment of ss-DNA, 60 ml DI water was loaded in the beaker, a droplet of ss-DNA solution was preloaded in the tube. Pressure of 25 kPa was applied for 7 hours. The solution in the beaker was sampled after the experiment. The absorbance spectra were shown by FTIR (Fourier transform infrared spectroscopy Cary 660-FT-IR). DI water was used as background to show the absorbance in **Figure 3.8** (a). The green line shows that ss-DNA could pass through CNTs membranes just by applying pressure. The absorbance shown in **Figure 3.8** (a) suggests that more ss-DNA could pass through CNTs by the additional electric field.

In the case of Haemagglutinin under pressure driven condition, no absorbance observed in spectra of samples carried out at applied pressure of 10, 15 and 20kPa for 7 hours. **Figure 3.8** (b) shows the measured spectrum under 25 kPa for the above samples with additional 15 hours. Again

there is no absorbance observed. Then a pressure level of 25kPa and a bias of 5V was applied together. The measured spectrum indicates a weak absorbance as shown in **Figure 3.8** (b). It suggests that Haemagglutinin could pass through CNTs when pressure and electric field were applied together. But the translocation rate was relatively low compared to that of ss-DNA. This is because the dimension of Haemagglutinin is much larger than that of ss-DNA. The test result shows that permeability decreases with the increase of dimension of molecule.

To confirm CNTs nanofilters could block all the micro-scale substance, we further tried passing bacterium through CNTs nanofilters. In this experiment, PBS and BPSM (Bordetella pertussis, streptomycin resistant) are employed. The test setup is as shown in **Figure 3.6** (a). 0.1 ml mixed solution was loaded in the device and PBS was loaded in the beaker. A medley of pressure and electric field driven method was used to drive the PBS through the CNTs nanofilters. The pressure is 20kPa and the electric bias is 5V. To detect the bacterium of very low concentration, the solution should be sampled for cell culture and enrichment. To ensure the bacterium were viable in ambient temperature during the experiment, the test was conducted for 2 hours. The solution sampled in the beaker was cultured on blood agar plates for 5 days to see whether bacteria passed through the CNTs nanofilters. Solution with bacteria loaded in the device chamber was also cultured as control group for comparison. **Figure 3.9** (a) shows the result of bacterial culture of the solution sampled from the device chamber. After 5 days of culture, bacterial colonies were observed. **Figure 3.9** (b) shows the result of bacterial culture of the solution sampled in the beaker. No bacterial colony was found which confirms a perfect bacterium blockage.

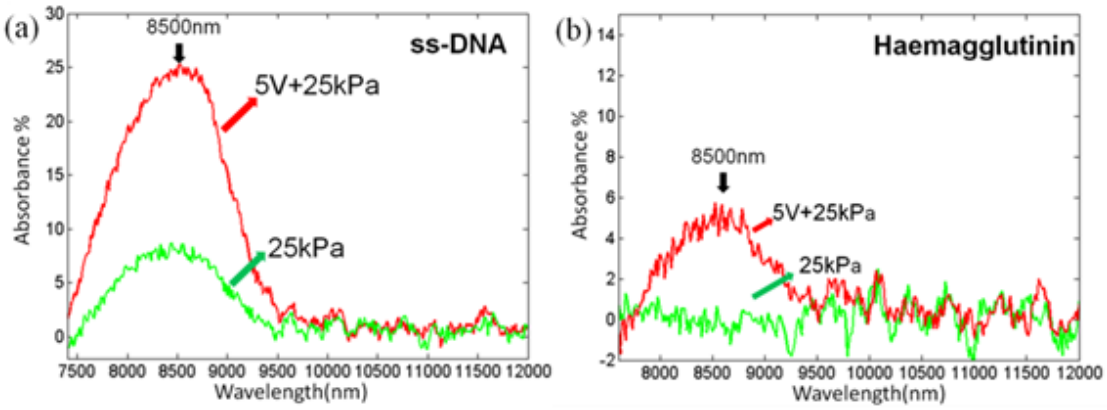

Figure 3.8 (a) IR spectra of ss-DNA in the beaker after applying 25kPa pressure and after applying both 25kPa pressure and 5V bias; (b) IR spectra of Haemagglutinin in the beaker after applying 25kPa pressure and after applying both 25kPa pressure and 5V bias.

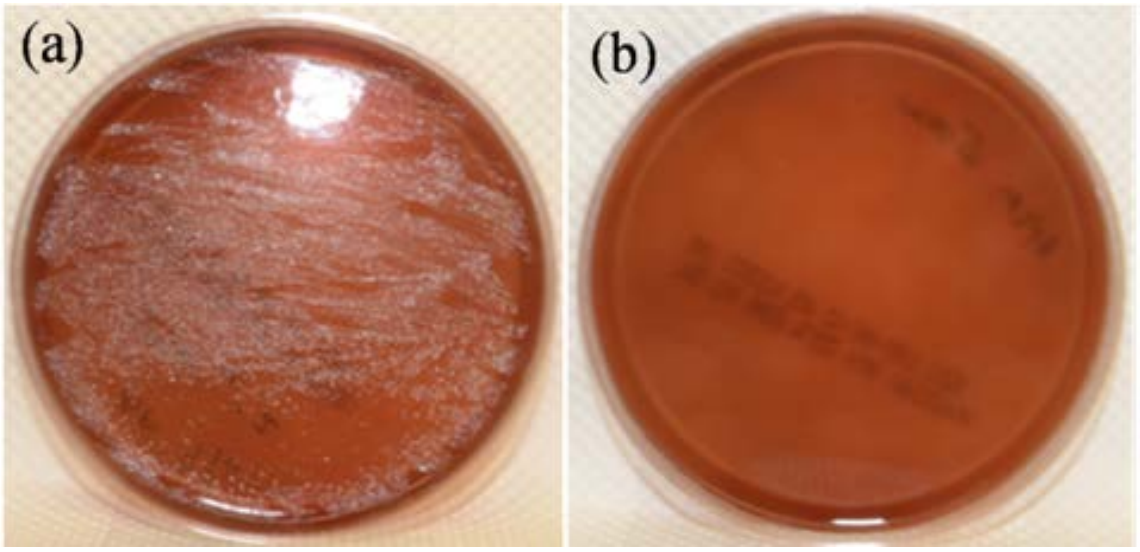

Figure 3.9 **(a)** Result of bacterium culture of the solution sampled from the device chamber, bacterial colonies were observed; (b) Result of bacterium culture of the solution loaded in the beaker, no bacterial colony was found.

In conclusion, we propose a new fabrication process for a stretchable membrane based nanofilters using patterned array of vertically grown carbon nanotubes bundles. The functionality is proved by pumping ions through CNTs membranes either by applying pressure or applying electric field. A linear relation between mass transport rate and driving pressure is observed. The ss-DNA could pass through the CNTs membranes by applying high pressure and an additional

electric field can further enhance the permeability. However, Haemagglutinin whose dimension is close to the inner diameter of the CNTs cannot pass through the CNTs membranes just by applying pressure but an additional electric field could make it pass through. It proves that the permeability through CNTs nanofilters is highly dependent on molecular weight and physical dimension. Micro-scale bacterium would be totally blocked which confirms device's high quality and reliability. The test results prove that the CNTs membranes could be deployed as nanofilters working at high pressure which is not reported yet. The CNTs nanofilters of patterned CNTs bundles on the flexible polymer materials enable a further integration with other microfluidics for chemical and pharmaceutical applications. These results also indicate the device could be used for size matching molecular sieving. Just by using the same process on CNTs of different inner diameters, the devices could be used for different kinds of chemical separation. It is also possible to involve surface functionalization to enhance the capability of chemical separation.

3.2 Integration between Microneedle and CNTs nanofilters for selective drug delivery

3.2.1 Fabrication process

Figure 3.10 illustrates the fabrication process. The process began with thermal oxidation of single crystal silicon substrate to form a etch stop oxide layer. After the CVD of polycrystalline silicon as a sacrificial layer, a 5 nm thickness of Fe film, which acted as the catalyst film for the selective growth of CNTs, was patterned onto the silicon substrate (**Figure 3.10**(a)). As illustrated in **Figure 3.10**(b), the vertical aligned CNT bundles of 50 μm in height were grown via pyrolysis of acetylene at 800ºC with an Ar/NH3 flow for 15 min. As illustrated in **Figure 3.10**(c), the CVD parylene-C was employed to fill into vertically aligned CNTs and then to reinforce the inter-tube binding at room temperature. Thus, the top side of CNTs was covered with parylene-C, and the discrete CNTs were bound together by parylene-C as show in **Figure 3.11**(a). This step was the most critical process for forming the mechanical supporting layer for CNT bundles. The thickness

of the flexible parylene-C layer was determined by the CVD process. To achieve reliable mechanical strength for the following process, a 10 μm thick parylene layer was deployed. The parylene layer was peeled off together with CNT bundles from the substrate. As shown in **Figure 3.10**(d), the parylene film was attached onto a thin glass slide. Then a layer of 50μm SU-8 was deposited onto the parylene layer. The thickness of this SU-8 layer was the same as the height of CNT bundles. Due to the transparency of the glass slide and parylene layer, the SU-8 layer was exposed from the back side of the glass slide. The catalyst layer under the CNT bundles could act as mask in this lithography step. The SU-8 above the CNT bundles would not be exposed. After development of SU-8, the parylene top of CNT bundles would not be covered by SU-8 as shown in **Figure 3.10**(e) and **Figure 3.11**(b). Such a SU-8 layer deposited above the parylene layer could act as hard mask for plasma etching. The sealed parylene top of CNT bundles could be etched by oxygen plasma as shown in **Figure 3.10**(f) and **Figure 3.11**(c). Then the parylene layer was released together with the SU-8 cover layer from the glass slide and bonded onto an unexposed SU-8 layer deposited on another thin glass slide as shown in **Figure 3.10**(g). In this process, a layer of SU-8 was spin coated and pre-baked on a thin glass slide first. After cooling, the released parylene layer was attached onto the SU8 layer then re-bake the SU-8 layer to make it molten. After cooling, a good bonding was formed between the parylene layer and the SU-8 layer. The sample was exposed from the backside of the glass slide to form a drug reservoir under the parylene layer as shown in **Figure 3.10**(h). The size of the drug reservoir should be slightly larger than the dimension of the CNT bundle array. The catalyst layer at the backside of CNT bundles was etched off by oxygen plasma and a thin PDMS layer was bonded at the backside as shown in **Figure 3.10**(i). For the bonding between PDMS and SU-8, the PDMS layer should be treated with nitrogen plasma then be attached onto the SU-8 layer and baked at 120ºC for 30 minutes. Then a 30μm

thick SU-8 membrane was patterned on the front layer of sample as shown in **Figure 3.10**(j) to reinforce the structure. On this membrane layer, holes aligned with the CNT bundle array were patterned. As shown in **Figure 3.10**(k), array of SU-8 four-beam sidewalls array was further aligned and patterned above the membrane layer. As shown in **Figure 3.10** (i), a thick PDMS layer with a center hole was bonded at the backside. This PDMS layer was used for tubing purpose. The center hole was for the insertion of the tube. Then SU-8 sharp tips were assembled onto the four-beam sidewalls array by double drawing lithography as shown in **Figure 3.10** (m). Finally, a gold surface electrode was deposited onto the whole surface by evaporation as shown in **Figure 3.10** (n). The detailed structure of a single microneedle integrated with a CNT nanofilter is shown in **Figure 3.10** (o).

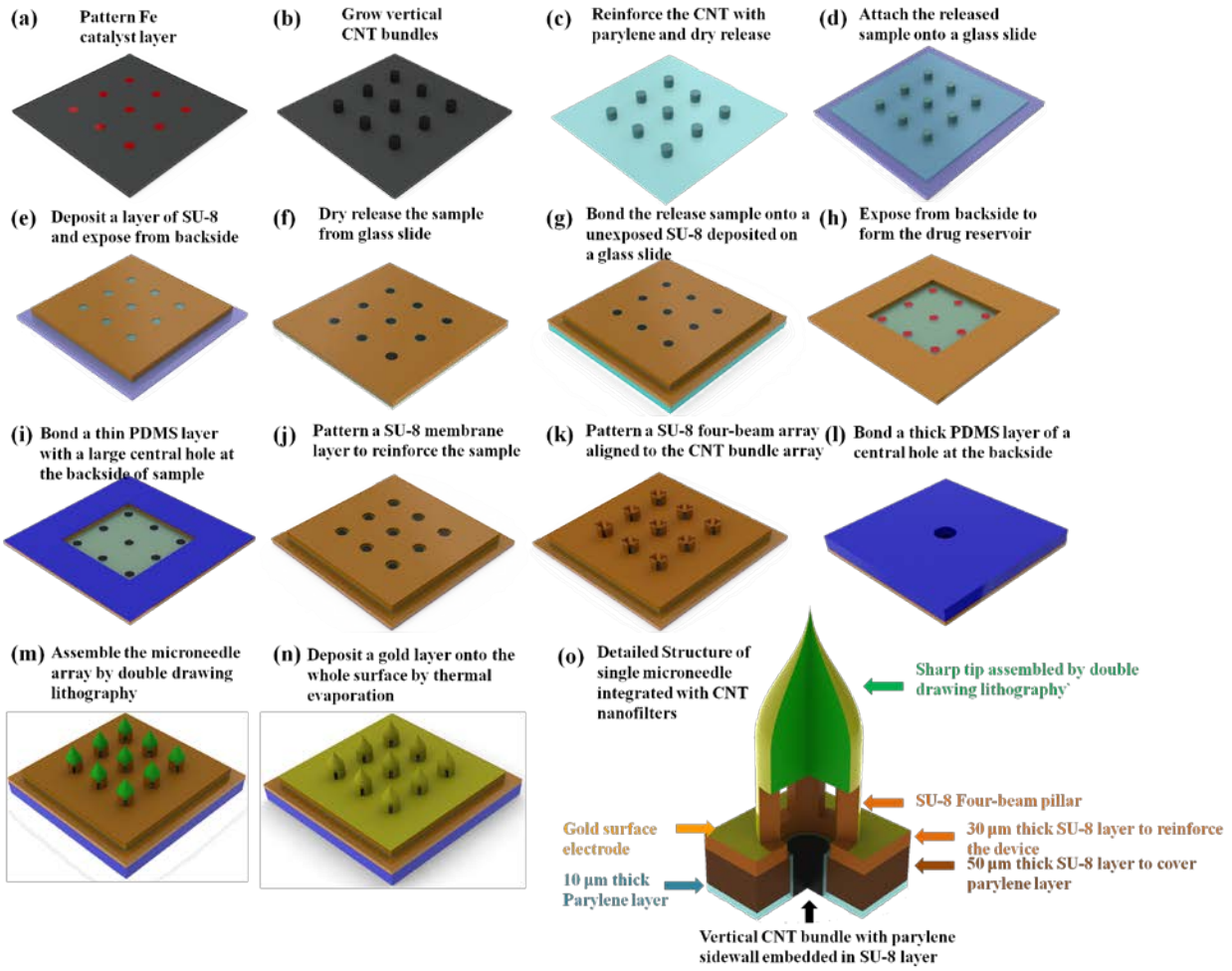

Figure 3.10 Fabrication process for microneedle array integrated with CNT nanofilters: (a) Pattern Fe catalyst layer; (b) Grow vertical CNT bundles; (c) Reinforce the CNT with parylene and dry release; (d) Attach the released sample onto a glass slide; (e) Deposit a layer of SU-8 and expose from backside; (f) Dry release the sample from glass slide; (g) Bond the release sample onto an unexposed SU-8 deposited on a glass slide; (h) Expose from backside to form the drug reservoir; (i) Bond a thin PDMS layer with a large central hole at the backside of the sample; (j) Pattern a SU-8 membrane layer to reinforce the sample; (k) Pattern a SU-8 four-beam array aligned to the CNT bundle array; (l) Bond a thick PDMS layer with a central hole at the backside; (m) Assemble the microneedle array by double drawing lithography; (n)deposit a gold layer onto the whole surface by thermal evaporation; (o) Detailed structure of single microneedle integrated with CNT nanofilters.

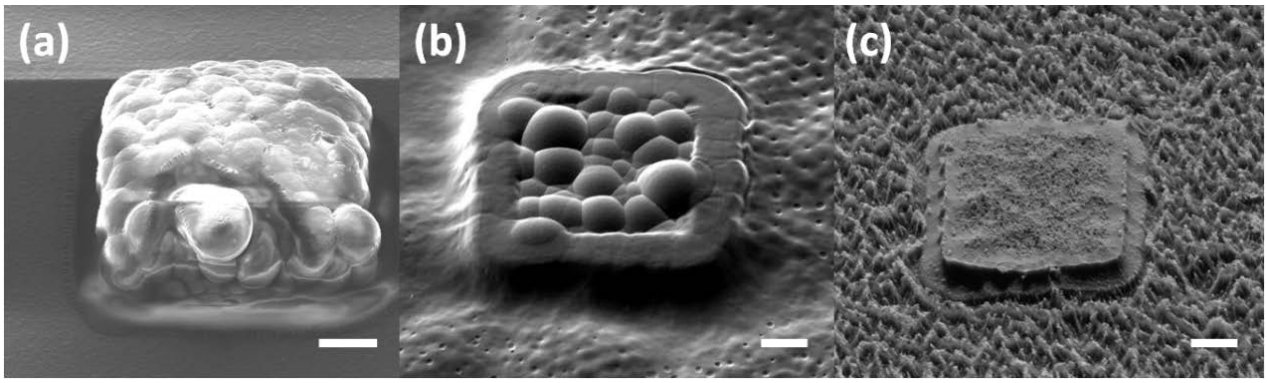

Figure 3.11 (a) CNT bundle coated with parylene, the scale bar is 10μm; (b) CNT bundle with parylene top embedded in SU-8 layer, the scale bar is 10μm; (c)CNT bundle embedded in SU-8 layer after oxygen plasma etching, the scale bar is 10μm.

3.2.2 Characterization of CNT nanofilters within microneedles

In the fabrication process, the both ends of CNT bundle need to be opened by oxygen plasma. Initially the bottom end of CNT bundle is sealed by Fe catalyst layer. Fig 5(a) shows the exposed CNTs at the bottom side after oxygen plasma treatment. The infiltration depth of the parylene by CVD is limited by the nano-scale gap between the individual CNTs, the inner part of the CNT bundle cannot be reinforced by parylene. Thus there is no parylene at the central bottom area of the CNT bundles. Fig 5(b) shows the detailed image of the exposed CNTs at the bottom end of a CNT bundle after oxygen plasma etching. There is no parylene between the CNTs.

In the process of etching the top parylene layer, the proper dose of oxygen plasma is critical to make the CNTs exposed. **Figure 3. 12** (c) shows the top of CNT bundle with the proper dose of oxygen plasma. **Figure 3. 12** (d) shows the detailed image of the exposed CNTs. In the images, tops of individual CNTs could be seen embedded within the parylene reinforcement. No cracks between CNT and parylene were observed. The SU-8 layer around the CNT bundle was very rough after the oxygen plasma etching. **Figure 3. 12** (e) shows the CNT bundles with the over dose oxygen plasma treatment. The CNTs were fully exposed and the parylene between CNTs are totally etched off. The connection between CNT bundles and parylene sidewalls became very weak.

By applying an air pressure from the backside, the whole CNT bundle would be blown away as shown in **Figure 3. 12** (f). To ensure the CNT bundles are etched with the proper dose of oxygen plasma, the whole etching process was divided into several cycles. The samples were checked by SEM after every cycle until only the tops of CNTs were exposed as shown in **Figure 3. 12** (d).

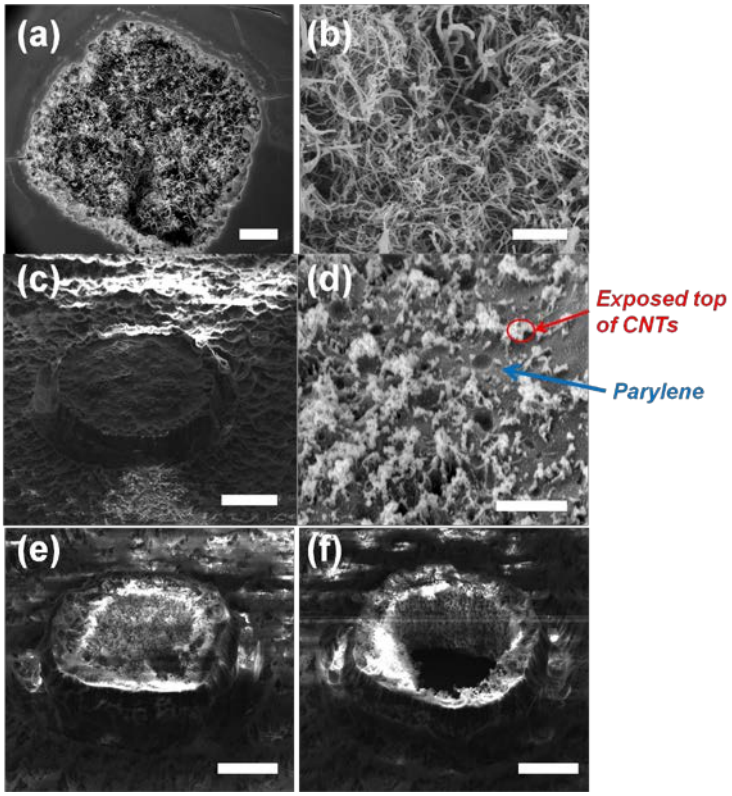

Figure 3.12 Backside of the CNT bundle. The catalyst layer is etched by oxygen plasma. The scale bar is 10μm. (b) The detailed image of the backside exposed CNTs. The scale bar is 2μm. (c) Top of the CNT bundle with proper etching dose. The scale bar is 20μm. (d) The detailed image of the top exposed CNT. The scale bar is 2μm. (e) Top of the CNT bundle with over etching dose. The scale bar is 20μm. (f) After applying an air pressure, the CNT bundle within the parylene sidewall is blown away. The scale bar is 20μm.

3.2.3 Nanoparticles blockage test

By having the CNT nanofilters, nano-scale substance whose dimension is larger than the inner diameter of the CNT nanotube should be blocked. However, micro-scale and nano-scale cracks may occur in the parylene reinforced CNT bundles which will cause the device failure. It is necessary to verify there is no crack in the CNT nanofilters device. Because the whole device is

made of polymer which is not suitable for TEM imaging, we leveraged fluorescent nanobeads to confirm whether the samples were crack free or not in this study.

Texas red (Sigma Aldrich, Singapore) whose molecular weight is 606.71 and fluorescent nanobead (Sigma Aldrich, Singapore) whose dimension is 80nm were mixed and delivered into the mouse skin by the microneedle devices with and without CNT nanofilters. The fluorescent images are shown in **Figure 3. 13**. For the device without CNT nanofilters, both Texas red and fluorescent nanobeads are delivered into skin as shown in **Figure 3. 13** (a). The color of the mixed fluorescent is violet. For the device with CNT nanofilters, the skin shows red color rather than violet as shown in **Figure 3. 13** (b), which indicates only Texas red is delivered and fluorescent nanobeads are blocked. The results confirm that the CNT nanofilters could block nanobeads and there was no nano-scale crack in the CNT nanofilters. On the other hand, it has been reported that out-of-plane microneedles are not able to be inserted entirely into the skin [67-69]. During the process of delivering drug into the skin, we found that there were micrometer scale tiny gaps between bottom edge of each microneedle and skin surface due to the skin deformation as depicted in **Figure 3. 13** (c). The concave skin surface around the edge of microneedle sidewall leaves a tiny gap at bottom part of microneedles. To investigate efficacy of microneedles in delivering drug even with the existence of these micrometer scale gaps, hydrogel absorption experiments were conducted to quantify the delivery rate and the relation between pressure and transport rate of drugs**.**

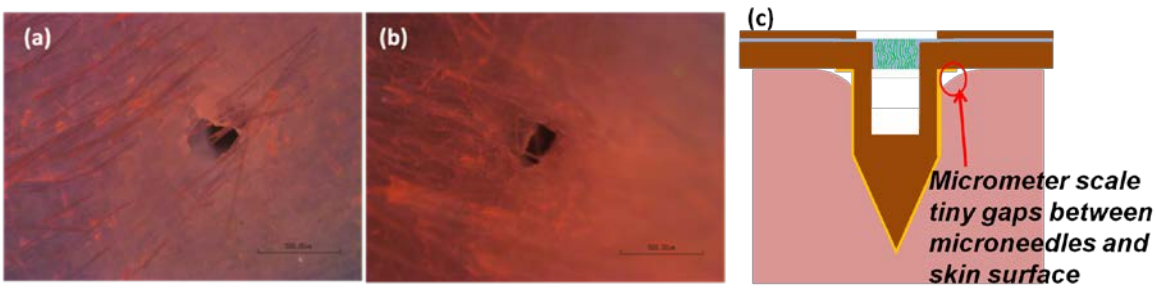

Figure 3.13 Fluorescent images of mouse skin: (a) Texas red and nano-fluorescent beads are delivered with microneedle device without CNT nanofilters; (b) Texas red and nano-fluorescent beads are delivered with microneedle device with CNT nanofilters; (c) The micrometer scale gaps occur between skin and bottom edge of a microneedle due to skin deformation.

3.2.4 In Vitro Drug Delivery Test

Gelatin hydrogel was prepared by boiling 70 mL DI (Deionized) water and mixing it with 7g of gelatin powder (KnoxTM original unflavored). After cooling down, the solution was poured into a petri dish to 1cm high. Then the petri dish was put into a fridge for half an hour. The Gelatin solution became collagen slabs. The collagen slabs were cut into 6mm×6mm sections. A piece of fully stretched Parafilm (Parafilm M, USA) was tightly mounted on the surface of the collagen slabs. This parafilm was used here to block further diffusion of leaked solution into the collagen slab in the delivery process. Then the microneedles penetrated the parafilm and went into the collagen slab as shown in **Figure 3.14**. The drug could be delivered through microneedles and absorbed by the hydrogel.

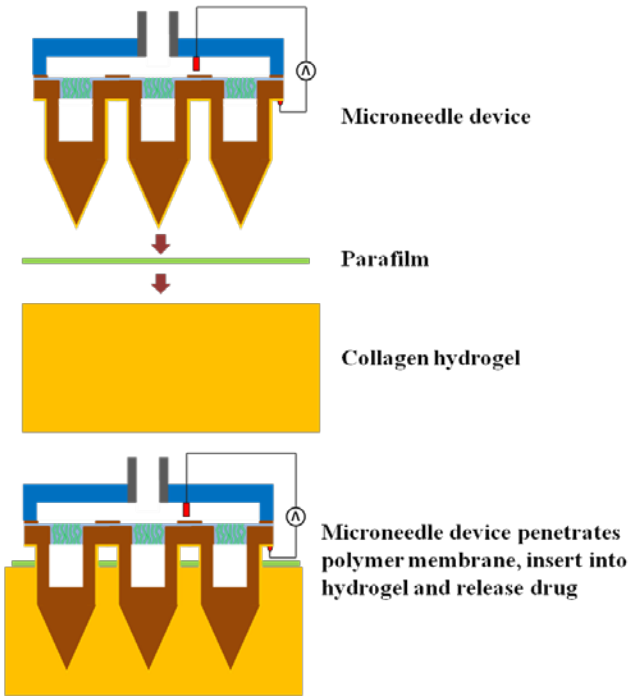

Figure 3.14 Scheme describing experimental setup to test microneedle device in an in vitro hydrogel skin model. Mironeedles penetrate parafilm and collagen hydrogel to subsequently deliver drugs with controlled pressure and electric field.

In the test of glucose delivery, glucose solution was delivered into the collagen slab under different pressure and duration. Then the collagen slabs were digested in 1mg/mL collagenase (Sigma Aldrich, Singapore) at room temperature. It took around 1h for all the collagen slabs to be fully digested. The solution was collected to measure the glucose concentration with Glucose Detection kit (Abcam, Singapore). By comparing the readings from the kit with the measured concentration standard curve[70], the concentration of the glucose in hydrogel was measured. According to the glucose concentration, the absorption rate and solution delivery rate of the glucose in the hydrogel were calculated.

Figure 3. 15 shows that the transport rate of glucose is proportional to the given pressure and the duration of the tests. When the pressure is lower than 1 kPa, no glucose could be detected. It indicates that the CNT nanofilters could be used as a pressure valve for the delivery of glucose. The delivery rate is around 70% for all the test data. It means around 30% of the drug would leak

to the surface. More importantly, after the pathways are created through the stratum corneum layer by microneedles, the drug which leaked to the skin surface eventually diffused into a deeper layer under the stratum corneum layer [71].

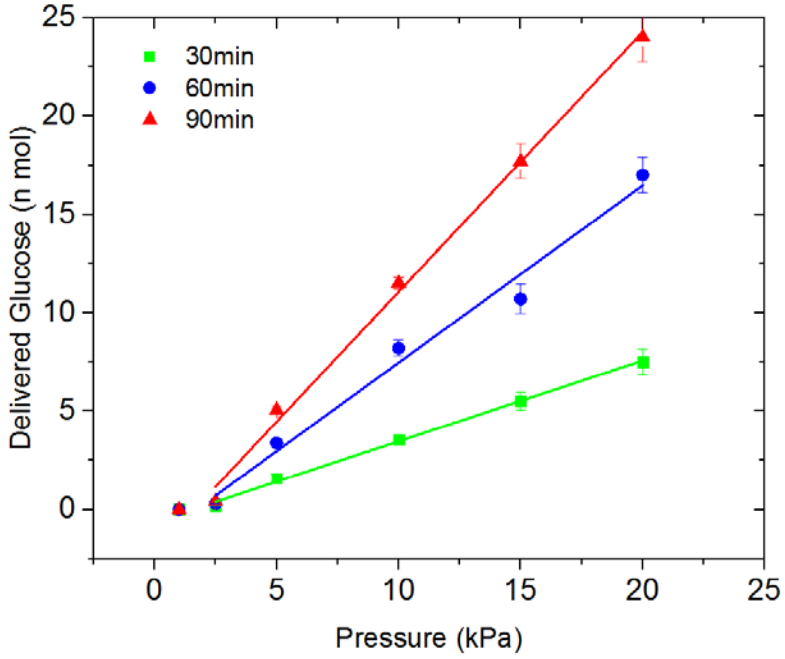

Figure 3.15 Glucose delivery quantity as a function of pressure.

We conducted the same hydrogel absorption experiment for insulin. Insulin is a peptide hormone and central for regulating carbohydrate and fat metabolism in the body. Due to the poor absorption or enzymatic degradation of insulin in the gastrointestinal tract and liver, the transdermal delivery has been so far the preferred method of insulin administration. The molecular radius of insulin is 1.34nm[72] which is smaller than the inner diameter of the CNTs in the device. It could pass through the CNTs just by applying pressure. Since the insulin molecules are positively charged in the solution, the transport rate could be tuned by applying electric field.

The insulin solution of 1mg/ml concentration was preloaded in the drug reservoir. Air pressure levels in the range from 5kPa to 20kPa were applied for 30mins. The resultant solution samples were analyzed by FTIR as shown in **Figure 3. 16** (a). The peak value indicates the concentration

of insulin in the sampled solutions. From the test results, the concentration of insulin is proportional to the pressure level which means the transport rate of insulin through CNTs is linear to the pressure level.

Then the test was repeated by applying bias ranges from -10V to +10V and air pressure ranges from 5kPa to 20kPa. The peak value of IR spectra at 4.7μm wavelength was recorded in **Figure 3. 16** (b). The positive bias could facilitate the transport of insulin and negative bias could decrease the transport rate. For the line of -7.5V and -10V, when the pressure was lower than 10kPa, the IR spectra at 4.7μm wavelength was lower than the noise level thus no insulin was detected. This result indicates that the CNT nanofilters could be used as both pressure valve and electric switch for the delivery of insulin. And a sufficient reverse bias could balance the air pressure, realizing a zero delivery of insulin.

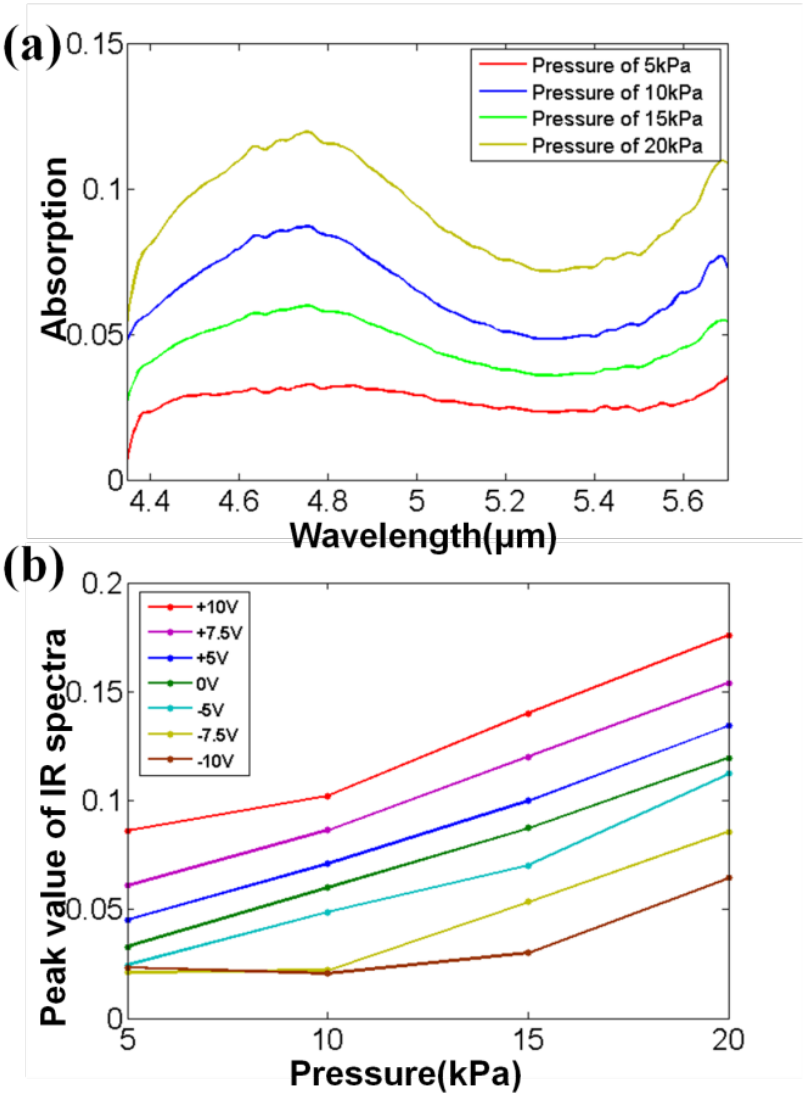

Figure 3.16 Insulin delivery test result: (a) IR spectra of insulin by applying different pressure; (b) The peak value of IR spectra by applying different pressure and bias of electric field.

Hemagglutinin is a type of antibody that agglutinates red blood cells. It is a cylindrical molecule whose longitudinal dimension and diameter are is 13.5 and 6.5nm, respectively [73]. Because the length of the molecule, 13.5nm, is larger than the inner diameter of the CNT nanotubes, 10nm, the Hemagglutinin cannot pass through the CNT just by applying pressure.

According to our previous study [74], Hemagglutinin can pass through the CNTs when both electric field and pressure are applied together. This is because the cylindrical molecule can be aligned by the DEP force.

In the test, we applied 5V bias for 1 hour. The pressure changes from 5kPa to 20kPa. The sample solution was analyzed with FTIR. The IR spectra were shown in **Fig. 3. 17**. Due to that we used a water based s0olution as background for FTIR analysis, some negative peaks occurred in the spectra meaning the absorption was lower than water at that wavelength. The peak value was not in proportion to the pressure which indicates that the transport rate of large molecules is not proportional to the pressure. No heamagglutinin was detected when no electric field was applied. Therefore, the CNT nanofilters could act as an electric switch for the delivery of heamagglutinin.

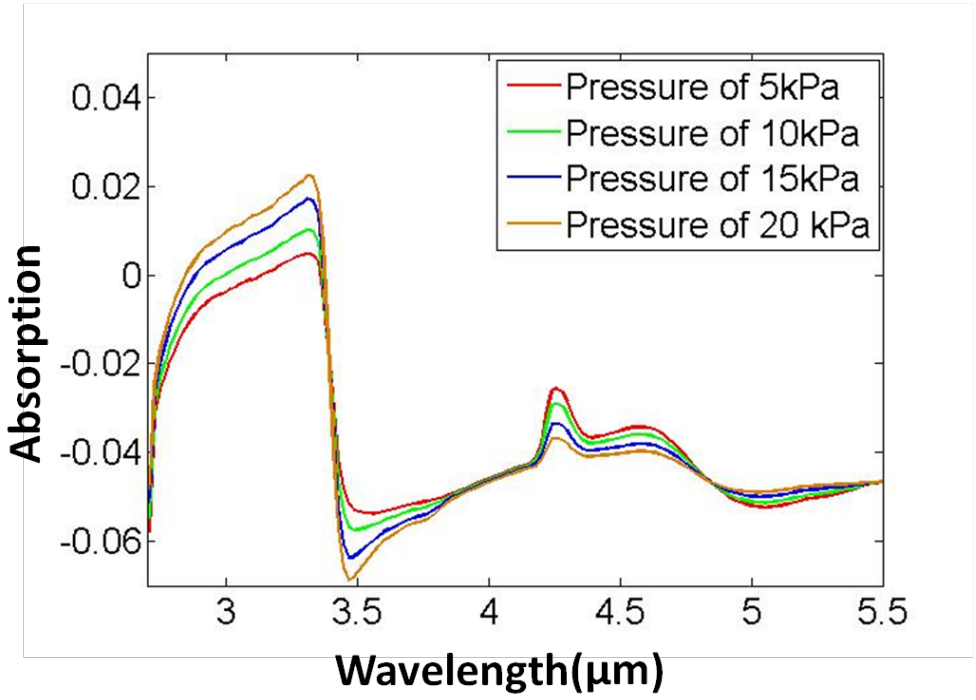

Figure 3.17 IR spectra of Hemagglutinin by applying different pressure.

The transport conditions of glucose and Hemagglutinin through CNT nanofilters are different. So if glucose and Hemagglutinin are mixed together, a selective transport could be realized by controlling the pressure and electric field applied. Then we mixed the glucose and Hemagglutinin together and conducted the test again. In one test, only 20kPa pressure was applied. In another test 5V bias and 20kPa pressure were applied. The duration of both tests was one hour. The IR spectra

were shown in **Figure 3.18**. The green line is the reference of Hemagglutinin and the brown line is the reference of glucose. For Hemagglutinin, there is a negative peak at 3.5μm. For glucose, there is a positive peak at 4.3μm. When only pressure was applied, only glucose was detected. The blue line shows the similar curve as the brown line without the negative peak at 3.5μm. When both pressure and electric field were applied, both Hemagglutinin and glucose could be detected. The red line indicates both the negative peak at 3.5μm. and positive peak at 4.3μm. This result confirms that by controlling the conditions, Hemagglutinin could be selectively delivered while glucose could always be delivered.

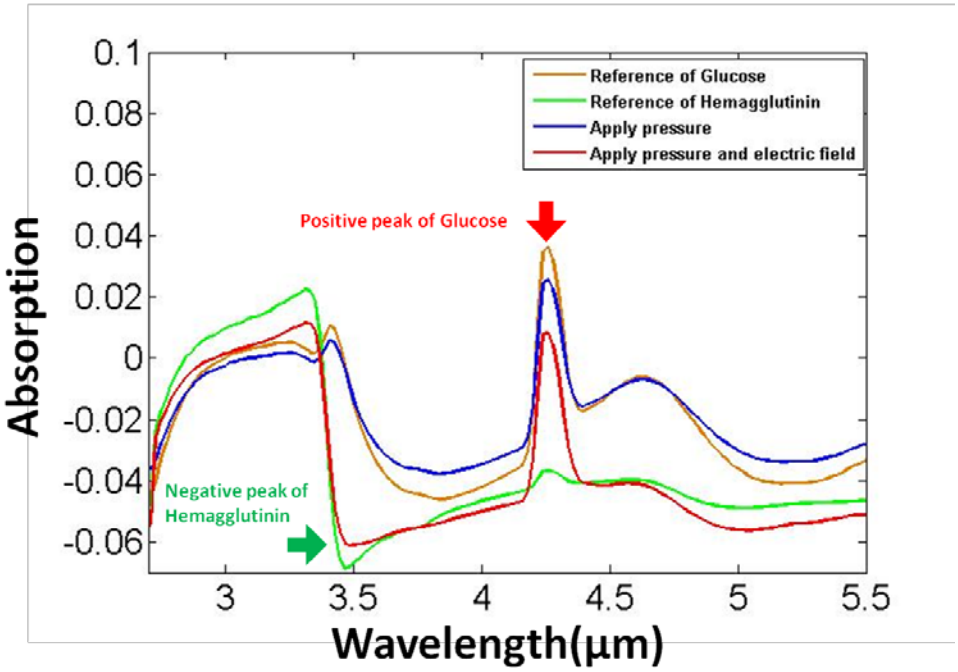

Figure 3.18 IR spectra of mixture solution of difference conditions.

3.3 Conclusion

A microneedle array integrated with CNT nanofilters for realization of controlled and selective drug delivery has been reported. The SU-8 tips made by the double drawing lithography process are sharp and stiff enough to penetrate skin. Nanobeads of 80 nm diameter were blocked in the test. It indicates there were no nano-scale cracks in the device and the CNT nanofilters could block

all substance larger than its inner diameter. The device could be used for controlled selective transdermal drug delivery. The transport rate of glucose and insulin of low molecular weight is proportional to the pressure given. But the transport rate of Hemagglutinin, i.e., a large molecule, is not in proportion to the pressure. The transport rate of charged molecule such as insulin could be tuned by an electric field. For the molecule which could be aligned by DEP force to pass through the CNT inner channel, CNT nanofilters could be used as an electrical switch. When the molecule is much smaller than the inner diameter of the CNTs, CNT nanofilters could be used as a pressure valve. The function of drug administration could be implemented by having the CNT nanofilters in microneedle array. It could expand the application of microneedles for a long term automatically disease monitoring and drug delivery system.

Chapter 4 Bendable microneedle

Currently the safety issue caused by needle breakage after skin penetration step is the main concern for clinically relevant applications. High aspect ratio and sharp tips made of rigid materials are necessary for conventional microneedles to provide a successful and reliable skin penetration [76-77]. Normally, microneedles made of materials of high Young's modulus such as nickel [78-79], stainless steel [80-81] and silicon [82-83], can avoid this needle breakage. However, these materials lack of biocompatibility, which is a key requirement for medical devices. On the other hand, microneedles made of bio-compatible polymers or natural fibers suffer from low mechanical strength. The consequent needle breakage can be induced either by very high buckling force attributed to the deformable skin surface during the skin penetration or by the lateral movement between the microneedle patch and the skin surface during the drug administration.

Thus, a novel bendable microneedle is proposed in this chapter to avoid the needle breakage during the drug administration. This bendable microneedle array with a soft base and a rigid sharp tip can tolerate the deformation associated with skin stretching without breakage when the skin patch is applied on the joint such as elbow and knuckle for osteoporosis treatment. In other cases, such as diabetes, for which microneedle patches are normally applied on the arm or abdomen, a lateral movement between the microneedle patch and skin surface may occur due to either the occasional touch or friction. In such case, the bendable microneedle will be dragged out of the skin instead of leaving a broken needle in the skin when lateral movement occurs. The sharp tips assembled onto the soft bases can be either non bio-dissolvable, i.e., made of SU-8 [84], or bio-dissolvable, i.e. made of maltose [85]. For the configuration with SU-8 sharp tips, the outlets of the microneedles, connecting with the drug reservoirs, are always exposed to air. Both water-soluble

and lipophilic drugs can be immediately delivered just after skin penetration. For the configuration with maltose sharp tips, the outlets can be fully encapsulated by maltose to inhibit the solvent evaporation of lipophilic drug formulation [86]. The drug can be delivered when the maltose tips are melted after skin penetration. However, the microneedle with maltose tip is not suitable for application of water-soluble drug formulation [87]. The evaporation of water in solvent will cause maltose tip melting. Therefore, the water-soluable drug formulation can only be stored in patches with SU-8 sharp tips.

4.1 Configuration and Demonstration of the bendable microneedle

In order to solve the needle breakage issue after skin penetration, a unique bendable microneedle design is proposed here. The bendable microneedle consists of two parts: a soft four-beam-pillar base made of PDMS and a stiff SU-8 sharp tip. The material of the sharp tips can be either SU-8 (**Figure 4.1(a)**) or maltose (**Figure 4.1(b)**). These sharp tips were assembled onto the four-beam-pillar structured array, which has four vertical gaps along the sidewalls (**Figure 4.1(a2)** and **Figure 4.1(b2)**). These four vertical gaps serve two functions: firstly, because the sharp tips made of SU-8 are not bio-dissolvable, the drug could be delivered out through these gaps; secondly, during the drawing lithography process, the sharp tips could form an anchor shape in these gaps to enhance the adhesion between sharp tips and four-beam-pillar base. Due to the flexibility of the PDMS pillars, the needle will bend when the lateral force applied onto the microneedle exceeds the threshold. These anchors of the rigid sharp tips in the gaps could fix the sharp tips onto the PDMS pillar and protect them from detaching the PDMS pillars when the whole microneedle is bent. **Figure 4.1(a3)** and **Figure 4.1(b3)** show the demonstrations of the bendable needle when a glass slide pushes the microneedle array from a lateral direction. These needles will bend when the lateral force is applied. They will recover to the initial state as long as the force is removed. After skin penetration, the relative movement between the microneedle patch and skin is inevitable

during the manual operation, which is one the major reasons for needle breakage. The soft PDMS pillars at the bottom of the microneedles will bend to absorb the mechanical strain caused by lateral movement and further prevent the breaking when this relative movement occurs. **Figure 4.1(a4)** shows a demonstration when the relative movement between skin and microneedle occurs after skin penetration. The dash line indicates the contour profile of needle position inside skin; from **(a4-i)** to **(a4-iii)**, the needle penetrated the skin, the whole sharp tip was into the skin; from **(a4-iv)** to **(a4-v)**, a lateral movement occurred, the needle had a displacement from its original position. The PDMS pillars beneath the SU-8 tip bended and the SU-8 tip still remained within the skin**(a4-vi)**; the needle was taken out of the skin and recovered to its original shape without breakage. This demonstration confirms that when the relative movement occurs, the needles will bend to match the new position of the skin. If the relative movement is too large, then the needles will be dragged out the skin and recover the initial state.

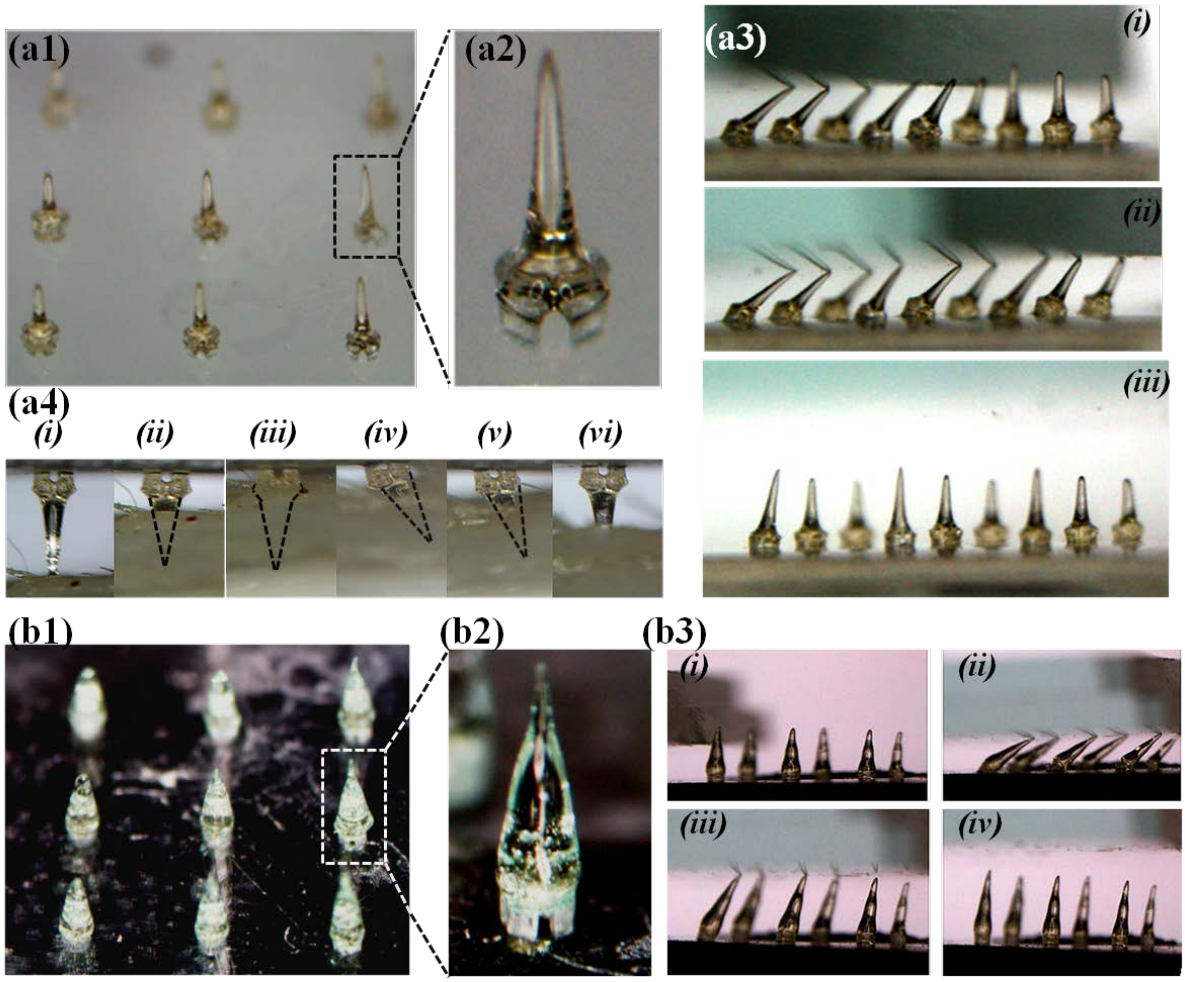

Figure 4.1 Demonstration of the bendable microneedle array. (a1) Optical image of the microneedle array with SU-8 sharp tips; (a2) Detailed optical image of an individual bendable microneedle with SU-8 sharp tip; (a3) Demonstration of the bendable microneedle array with SU-8 sharp tips when an lateral force is applied; (i): A glass slide began pushing the needle array from a lateral direction, part of the needle array bent; (ii): All the needle array was pushed by the glass slide and bended; (iii): The glass slide was removed, all the needles recovered to their original shape without breakage; (a4) Demonstration of the bendable microneedle when relative movement between skin and microneedle occurs after skin penetration. The dash line is used to indicate the contour profile of needle position inside skin;(i) A bendable needle is out of skin before the penetration; (ii) The microneedle pressed to penetrated the skin; (iii) The whole needle is into the skin; (iv) Al lateral movement occurs, the skin moves rightwards. The need is bent to adapt the lateral movement; (v) The distance of the lateral movement exceeds the threshold of the bendable needle, then the microneedle is out of the penetration hole; (vi) Lower the skin sample and make the bendable microneedle separate from skin surface. The needle recovers to its initial shape; (b1) Optical image of the microneedle array with Maltose sharp tips; (b2) Detailed optical image of an individual bendable microneedle with maltose sharp tip; (b3) Demonstration of the bendable microneedle array with maltose sharp tips when an lateral force is applied. The process is similar as in (a3).

4.2 Characterization and optimization of the bendable microneedles

Due to the elasticity of PDMS, the bottom part of the microneedles, which is represented by the PDMS pillars, will bend when the force applied onto the microneedles exceeds the buckling force. To realize a successful skin penetration, the stiffness of the PDMS pillars are expected to be as high as possible. Thus, we conducted a study of the stiffness of the PDMS by tuning the mix ratio of elastomer and curing agent. The PDMS with higher concentration of curing agent can have a higher stiffness. Here we tested the samples with mix a ratio of 1:4, 1:6, 1:8 and 1:10 for microneedles with both SU-8 and maltose sharp tips. Individual microneedles with PDMS base and SU-8 sharp tips were subjected to load in order to study their mechanical stability. The variation of measured bending force versus displacement was recorded. **Figure 4.2(a)** shows the measured curve of one sample. There are three parts: non-contact region, contact region and bend point, as indicated in this curve. The sharp drop of the force after the bend point confirms that the needles will not bend when the applied force is below the threshold. The forces of bend points of all the samples with different mix ratio of PDMS are shown in **Figure 4.2(b)**. For each mix ratio, 10 needles were tested. As shown in **Figure 4.2(b)**, for the mix ratio of 1:4, the bending force is about 0.8N for SU-8 sharp tips and 1.14N for maltose sharp tips. The bending force decreases with the decrease of the mix ratio. The buckling force of needle with maltose sharp tip is higher than that of the needle with SU-8 sharp tip because of the different shapes of the sharp tips. As shown in **Figure 4.1(a2)** and **(b2)**, the SU-8 sharp tip is slimmer than the maltose needle. This is because the viscosity of SU-8 is lower than that of maltose. During the drawing lithography process, the SU-8 sharp tip tends to have a slim central part while maltose sharp tip tends to have a thicker and stronger central part. Thus the force to make the needle with SU-8 sharp tip bent is lower than that of the needle with maltose sharp tip. Based on previous research[144], the force required for skin penetration ranges from 0.1N to 3N for an individual microneedle. The bending force of the

microneedle cannot be higher than the maximum force required for skin penetration, which is 3N. Thus our bendable microneedle may not able to realize a stable skin penetration. Here we conducted the skin penetration tests with samples of different PDMS ratio to check the performance of skin penetration. A 3x3 microneedle array was applied onto skin and the number of penetrated holes created by needles was recorded and the results are shown in **Figure 4.2(c)** and recorded in **Table 1**. For the samples with a mix ratio of 1:4, there are 8 **Figure 4.2(i-1)** and 6 **Figure 4.2(i-2)** penetrated holes on skin for needles with SU-8 sharp tips and maltose sharp tips respectively. For the samples with mix ratio of 1:6, there are 4 **Figure 4.2(ii-1)** and 3 **Figure 4.2(ii-2)** penetrated holes on skin for needles with SU-8 sharp tips and maltose sharp tips respectively. For the samples with a mix ratio of 1:8, there is no penetrated hole that can be found on skin for both needle configurations, as shown in **Figure 4.2(iii-1)** and **Figure 4.2(iii-2)**. Thus, we could conclude that, in order to ensure a good skin penetration, the mix ratio of 1:4 is desirable for the device fabrication. The success penetration rate of the needle with maltose sharp tip is lower than that of needle with SU-8 sharp tip when the test results of buckling force show an inverse trend. Although the maltose needle can stand a higher buckling force, it also requires higher force to penetrate the skin. This is because the thicker needle body of maltose sharp tip will affect a wider surface area during skin penetration, thus resulting in a higher possibility to get bent during skin penetration. **Figure 4.2(d)** shows the histology image of skin penetration by needles with SU-8 sharp tip and maltose sharp tip. The micro-channel created by the maltose sharp **(Figure 4.2(d-i-2))** tip is broader than that of the SU-8 sharp tip**(Figure 4.2(d-i-1))**, which confirms that the maltose sharp tip requires more force to penetrate skin. Another parameter that may affect the buckling force of the bendable microneedles is the angular of the PDMS pillars beneath the rigid sharp tips. When the angular of the pillars decreases from 60°to 30° and the angular of gaps

between pillars increases from 30° to 60°, the anchor of the rigid sharp tip will take a higher ratio, making the needle more rigid and enhancing the buckling force. However, for the assembly of SU-8 sharp tips by double drawing lithography, the baking time to melt the SU-8 tip assembled by the first step drawing cannot be well controlled to realize a partially filled gap for the samples with pillar angular lower than 55°. Because of the large gap angular, once melted, the SU-8 always fills the whole gap, leaving no outlet for the drug to be delivered. Therefore, for the needles with SU-8 sharp tips, we only use the pillars of 60°pillar angular. The drawing process to assemble maltose sharp tip is not limited by the pillar angular, thus the buckling force of needle with maltose needle by changing the pillar angular is evaluated and reported in **Figure 4.2(f)**. For each pillar angular, 9 needles were tested. When the pillar angular decreases from 60° to 30° (**Figure 4.2(e)**), the buckling force of the individual needle increases from 0.43N to 0.92N because the whole microneedle becomes more rigid. However, the contact area between maltose and PDMS pillars also decreases with the decrease of the pillar angular. Thus the maltose sharp tip cannot be well fixed within the PDMS pillars and tends to break or detach from the PDMS pillars when the vertical force is applied to make the microneedle bent. For the case of 30° pillar angular, 8 of 9 needles showed sharp tip breakage. The possibility of the needle breakage decreases with the increase of pillar angular. For the needles of pillar angular more than 50°, no needle breakage was observed in the buckling force tests. As a conclusion, to avoid needle breakage and have buckling force as high as possible, pillar angular of 50° is the optimum value for microneedles with maltose sharp tips.

Table 1. Details of success rate of skin penetration for needles with SU-8 and maltose sharp tips when the mix ratio of PDMS changes from 1:4 to 1:10.

Mix ratio / Needle type	1:4	1:6	1:8	1:10
SU-8 sharp tips	8/9	4/9	0/9	0/9

Maltose sharp tips	**6/9**	**2/9**	**0/9**	**0/9**

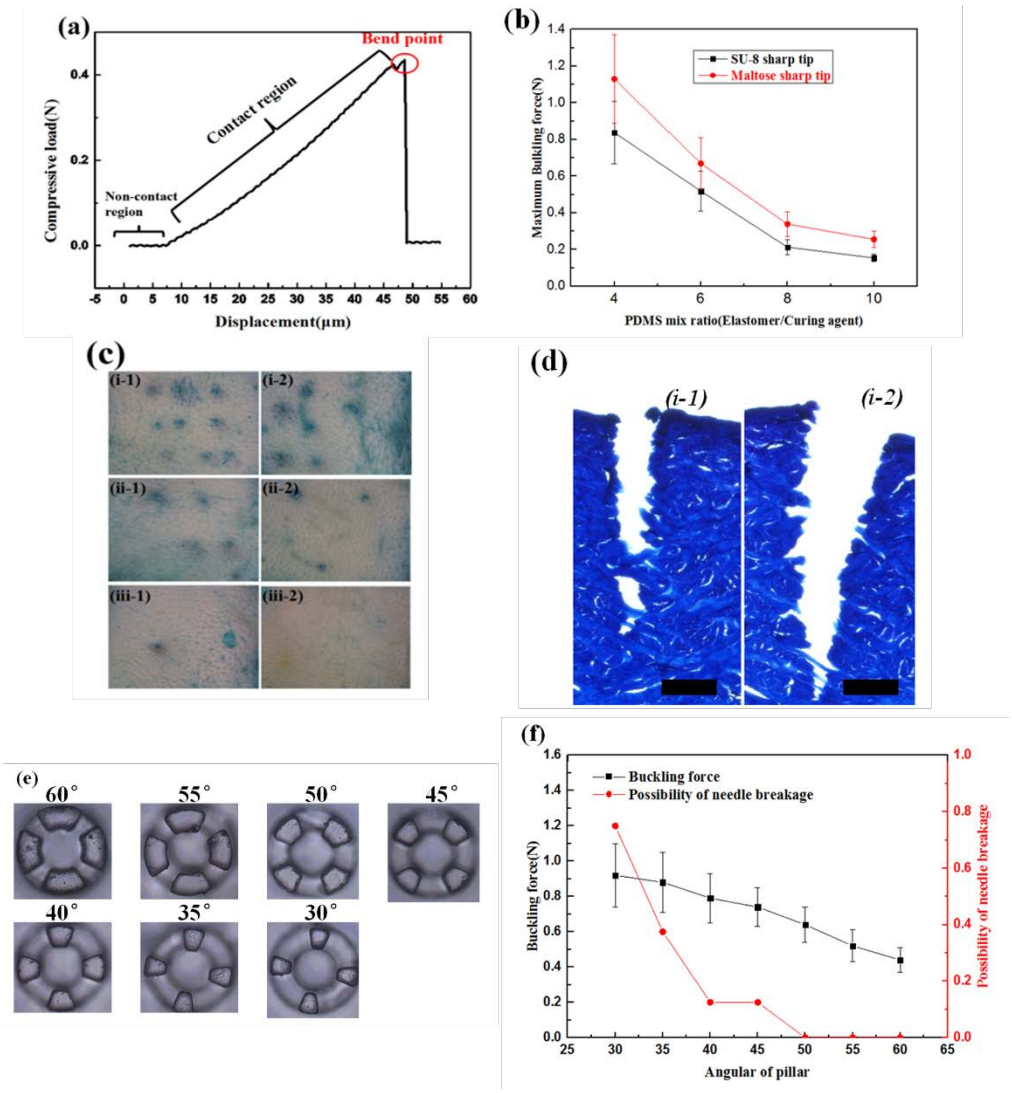

Figure 4.2 Optimization of PDMS stiffness and pillar angular of bendable microneedles for higher buckling force and success rate of skin penetration. (a) A representative example of the buckling force test result for bendable microneedle; (b) A representative example of the buckling force test result for bendable microneedle; (c) (c) Skin penetration results of microneedle with PDMS mix ratio of 4:1, 6:1 and 8:1 for needles with SU-8((i-1), (ii-1) and (iii-1)) and maltose((i-2), (ii-2) and (iii-2)) sharp tips: (i-1) and (i-2): The mix ratio is 4:1 and the number of penetrated holes are 8 and 6 respectively ; (ii-1) and (ii-2): The mix ratio is 6:1 and the number of penetrated holes are4 and 3 respectively; (iii-1) and (iii-2): The mix ratio is 8:1 and there is no penetration holes on the skin; (d) Histology image of skin penetration by needles with SU-8 sharp tip(i-1) and maltose sharp tip(i-2). The scale bar is 200μm; (e) Optical image of the PDMS pillar of angular changing from 60° to 30°; (f) Buckling force test and possibility of needle breakage of needle with maltose sharp tip by changing the pillar angular from 60° to 30°.

4.3 Conclusion

A unique bendable microneedles were proposed to overcome the safety issue associated with the microneedle breakage during the application. The PDMS mix ratio and pillar spacing are optimized for a maximum buckling force to enhance the skin penetration success rate. To adapt the applications for water-soluble and lipophilic drug formulations, two kinds of microneedle configurations are developed. Microneedles with SU-8 sharp tips are more suitable for the storage of water-based drugs while microneedles with maltose sharp tips are more suitable for the storage of lipid-based drugs. Such bendable microneedle can be integrated onto other flexible skin patch for transdermal drug delivery.

Chapter 5 Self-powered Wearable Adhesive Skin Patch with Bendable Microneedle Array for Transdermal Drug Delivery

Wearable flexible electronic medical devices have received major attention recently owing to their considerable practicability for several applications [88-97], including health monitoring and drug delivery for disease treatment [98-100]. The bendable microneedle introduced in the last chapter is promising to be integrated with flexible electronic device to realize a wearable drug delivery function.

Moreover, one key feature for wearable medical device is the fixation method. Acrylic medical bandage is widely used for medical patches. However, aging skin is more sensitive and vulnerable to a prolonged exposure to Acrylic medical bandage which is skin irritating and non-bio-compatible. Dry adhesive, which is inspired by the hierarchical structure on Gecko foot hair [101-102], possesses several advantages compared with conventional acrylic medical bandages: First, it shows repeatable and restorable adhesion with surface cleaning after each usage. Second, the physical structure to generate adhesive force is less affected by surface contamination, oxidation and other environmental stimuli. Third, the space between the pillars for ventilation of air should provide better bio-compatibility. Hence, we also adopt the dry adhesive for the fixation of the whole device on the skin.

To construct a complete drug delivery system for home healthcare monitoring, it is important to have feedback control function of the delivered drug. It can alert patients and provide the guidance when the dose of the drug to be delivered should be accurately controlled [103-106].

Currently, several wearable sensors for health monitoring have been explored, including devices that measure hydration [107], strain [108], glycaemia [109-111], metabolic acid [112] and cardiorespiratory signals [113]. For a further integration of diversified sensors mentioned above and construct a standalone wearable drug delivery skin patch with capability of health monitoring, signal process and interfacing with external cloud computing apparatus, a built-in energy source is inevitable to power components such as integrated circuits(ICs), microprocessor, liquid-crystal display(LCD) reading panel. Triboelectric energy harvester (TEH) typically using patterned PDMS is compatible with the fabrication process of flexible skin patch with microneedles. Thus, TEH is the most promising technique to fulfil the above-mentioned requirements.

In this chapter, the bendable microneedles were integrated on a wearable skin patch. The micro-patterns of the dry adhesives can provide the adhesive force. Meanwhile, the same microstructure of the dry adhesive are used for triboelectric patch to harvest energy from the contact with human skin, which has not been reported yet. Considering the locations for patch attached can be on flat skin surface like arm and abdomen or on joints like elbow and knuckle in different applications, we studied and developed two kinds of configurations to adapt these two situations for energy harvesting.

5.1 Configuration and fabrication process of the microneedle skin patch

We propose a stretchable adhesive flexible microneedle skin patch attached onto flat skin surface or joint parts, i.e., s elbow and knuckle, as shown in **Figure 5.1 (a)**. The whole skin patch consists of four functional components: bendable microneedle patch; dry adhesive patch; triboelectric energy harvester patch and drug delivery system with pump and drug reservoirs connected to the bendable microneedle skin patch. The detailed structure is depicted in **Figure 5.1 (b)**. The microneedle and triboelectric patches are connected with three dry adhesive patches to

make the whole wearable device able to be fixed onto the curved skin surface. The microfluidic control system with pump and drug reservoirs [113] can be assembled at the backside of the microneedle patch to control the drug delivery after the skin penetration. The detailed working principle of the pump system will be introduced in **Chapter 6**.

The structure of an individual bendable microneedle is shown in **Figure 5.1 (c)** where it consists of a bendable four-beam-pillar base and a rigid sharp tip. The bendable pillar base is made of PDMS with optimized stiffness to ensure a high success rate of skin penetration, while certain volume deformation is allowed. A rigid sharp tip for skin penetration can be assembled onto the four-beam-pillar base structure by using double drawing lithography process. The gaps between the pillars can be partially filled with the same materials to form microneedles during the drawing lithography step. It provides anchoring between the sharp tip and soft base in order to fix the sharp tip onto the soft base and protect it from breakage when the whole microneedle is bent. Another functional component is the TEH patch for energy harvester. The triboelectric contact surface with PDMS micro-patterned structure can enhance the performance. Here we used the micro-pillar array with and without mushroom top, which is obtained from the same fabrication process of the dry adhesive patch, as the surface micro structure for TEH patch. Meanwhile, we also tested the sample with pyramid micro structure, which is normally used for TEH [114-117], as a comparison.

Two methods were developed to generate power from the TEH patch by applying the skin patch on different locations of the human body. When the patch is attached to the elbow of a straight forearm, the spacing between two dry adhesive patches is slightly shorter than the length of the TEH patch. Thus the TEH patch is bent and has no contact with skin surface at this initial state. Then when the joint is bent, the TEH patch is stretched and in contact with the skin. Thereafter, when the joint is straight again, the spacing between two dry adhesive patches is

compressed to make the TEH bent and separate from skin. Power can be harvested by repeating this cycle as illustrated in **Figure 5.1 (g)**.

For the case in which the patch is applied onto a flat skin surface like arm and abdomen, power can be generated by pressing and releasing the TEH patch to induce contact and separation between TEH patch and skin surface as illustrated in **Figure 5.1 (f)**. However, due to the sticky surface of PDMS, once the triboelectric contact surface is pressed onto skin, it cannot automatically separate from skin when the pressing is released. To solve this problem, a dry adhesive patch is assembled at the backside of the TEH patch as shown in **Figure 5.1 (d)**. When the finger lifts up, the dry adhesive can provide a pulling force to make the TEH detach from the skin surface. Because the adhesive force provided by the dry adhesive is limited, the dry adhesive will detach from finger when lifted up to a certain height. In order to have a maximized output power of TEH patch, the dry adhesive is optimized to provide a maximum lift-up height.

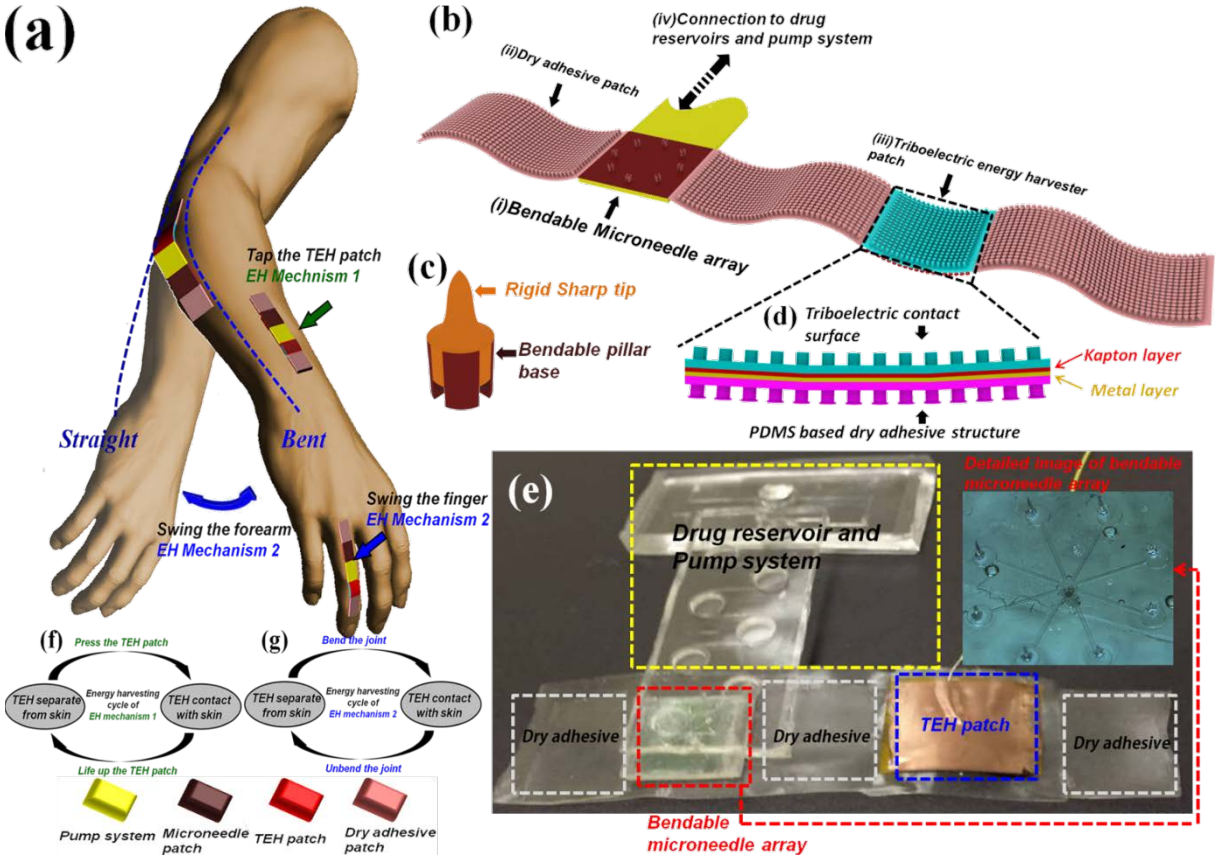

Figure 5.1 (a) Concept of the flexible microneedle skin patch attached on arm, elbow and knuckle. The patch consists of four functional components integrated on a whole PDMS sheet: Microneedle patch; Dry adhesive patch, TEH patch and pump system. (b) Detailed structure and functional components of the flexible microneedle skin patch; (c) Detailed structure of an individual bendable microneedle; (d) Detailed layer structure of the TEH patch; (e) Image of fabricated skin patch; (f) Attach the patch on flat skin surface like arm, power can be generated by pressing and lifting up the TEH patch (g) Attach the patch at the joint like elbow or finger, power can be generated by bending and unbending the elbow or finger.

The dry adhesive film in the skin patch is used to fix the whole device onto skin surface and also provides the pulling force to separate the TEH patch from the skin which will be mentioned in the next section. The detailed fabrication process can be found in **Figure 5.2**.

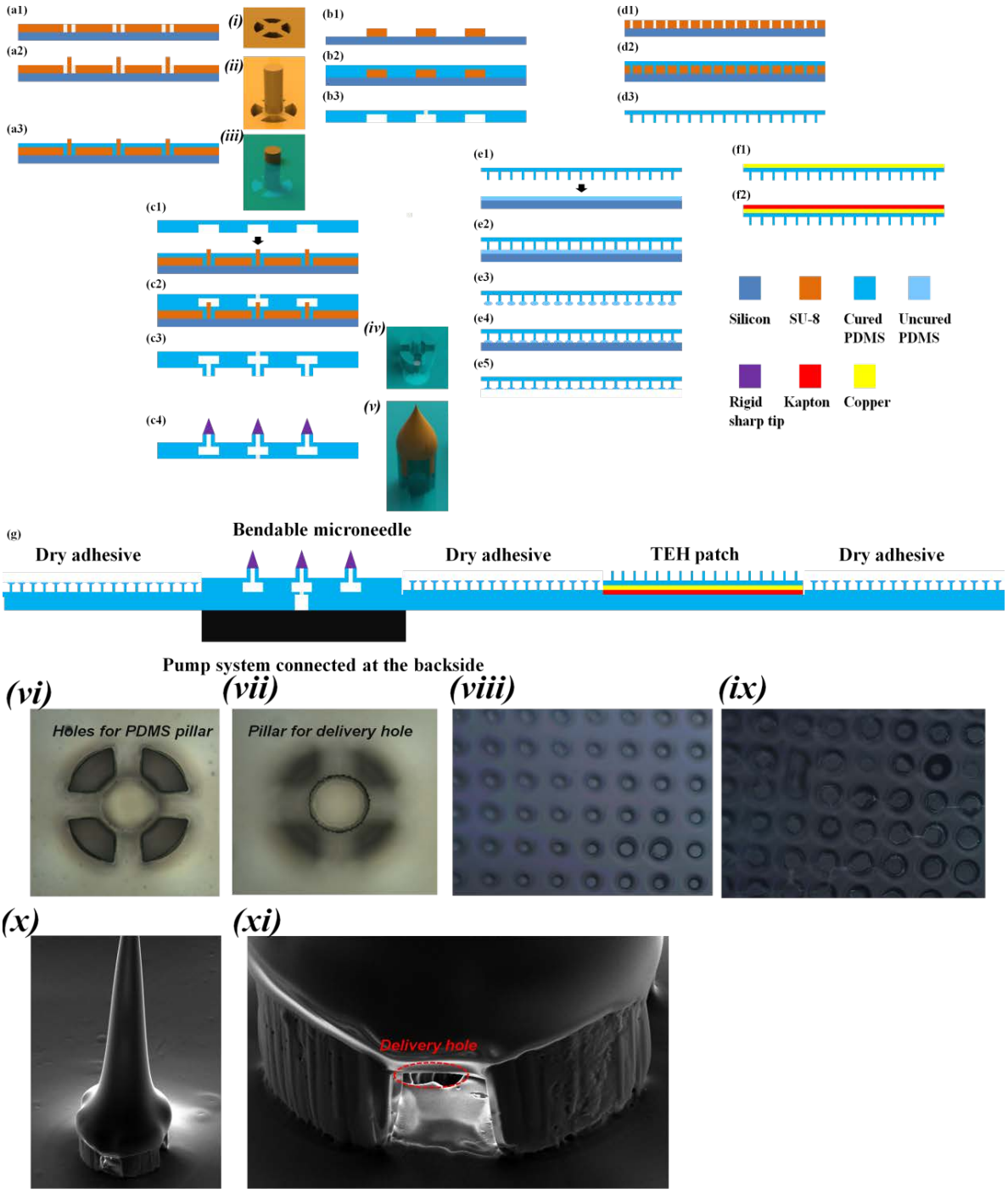

Figure 5.2 The fabrication process of the flexible microneedle skin patch.

5.1.1. Fabrication process for bendable microneedle array

(a), (b) and (c) show the fabrication process of the bendable microneedle patch. This microneedle comprises two PDMS layers and sharp tips.

The first PDMS layer is for the pillars supporting the sharp tips and the film holding the PDMS pillars as shown from (a1) to (a3). A SU-8 layer on silicon substrate was patterned to form the holes which are used as the mold for PDMS pillars as shown (i) and (vi). A SU-8 pillar was further patterned at the center of the holes as shown in (a2), (ii) and (vii). A PDMS layer was then spin coated onto the SU-8 layer to fill the SU-8 holes. But the thickness was not thick enough to cover the top of the SU-8 pillar as shown in (a3) and (iii). Thus, after the release of the PDMS layer off from the SU-8 layer, there will be a delivery hole located at the center of the four PDMS pillars as shown in (iv). These delivery holes form the connection between microneedles and other microfluidic channels.

The second layer is for the micro-channels array connecting the delivery holes as shown from (b1) to (b3). A SU-8 layer of the negative pattern of the micro-channel array was patterned on silicon substrate as shown in (b1) then covered with a PDMS layer as shown in (b2). Then the PDMS was cured by baking and released from the SU-8 layer as shown in (b3). A center hole was drilled by punch at the center of the channel array. This hole is to connect the channel array and the pump system in the final assembly process.

Then align the second PDMS layer with the first layer of PDMS which is still on the SU-8 mold as show in (c1) then bond these two layers by oxygen plasma treatment as shown in (c2). Release these two layers together off from the SU-8 mold as shown in (c3). Then rigid sharp tips were assembled by double drawing lithography as shown in (c4), (v), (x). (xi) shows the delivery hole within the four-beam pillar structure. The material can be maltose or SU-8 by leveraging the similar process.

5.1.2 Fabrication process for dry adhesive

The dry adhesive is fabricated by leveraging the inking and printing technology. A PDMS layer with un-inked micro-pillar array was achieved by demolding the PDMS from SU-8 mold as shown from (d1) to (d3). A SU-8 mold of 20μm thickness with micro-pattern of hole array was patterned on silicon substrate as shown in (d1). Then a PDMS layer was spun onto the SU-8 mold to fill all the holes on SU-8 mold as shown in (d2). Then cure and demold the PDMS layer off from the SU-8 mold as shown in (d3) and (viii). The height of the pillar is 20μm, which is the same as the thickness of the SU-8 mold.

The mushroom top which is necessary for dry adhesive to enhance the adhesive force is achieved by inking and printing process as shown from (e1) to (e5). A thin film of un-cured PDMS (5μm) was spun coat on a silicon chip as shown in (e1). Then the array of un-inked micropillars is inked in the un-cured PDMS film as shown in (e2). Subsequently, when lift the PDMS layer up from the un-cured PDMS film, small drops of un-cured PDMS is placed at the top of the array of un-inked micropillars as shown in (e3). Then the array was gently pressed against a silicon chip with treatment of detergent on the surface to peel sample easily as shown in (e4). Bake the sample to cure the PDMS droplet and release the dry adhesive off from the silicon chip as shown in (e5) and (ix).

5.1.3 Fabrication process for TEH patch

We leverage the pillar array which is achieved in (d3) as the surface micro-pattern required for TEH patch. A copper layer (200nm) was deposited by thermal evaporation at the backside of the PDMS layer as shown in (f1). Then a kapton layer was attached above the copper layer to fix the metal wire and protect the metal from scratching as shown in (f2). To study the different of performance by using different surface micro-patterns, we also use the dry adhesive in (e5) instead

of the pillar array in (d3) for the TEH patch. As a comparison with normal triboelectric patch, the pyramid surface micro-pattern is also used for TEH patch.

5.1.4 Fabrication process of the complete patch

All the functional patches are assembled onto a long PDMS sheet (200μm thickness) as shown in (g). For bendable microneedle patch, dry adhesive and pump system, they can be directly bonded onto the PDMS sheet by oxygen plasma treatment. Before the bonding of the bendable microneedle patch, a hole was drilled and aligned to the hole on the backside of the bendable microneedle patch to connect the bendable microneedle patch and pump system. The TEH is fixed by double side tape onto the PDMS sheet because the backside of the TEH patch is Kapton and cannot be directly bonded by oxygen plasma.

5.2 Characterization of the dry adhesive

To ensure the patch can be steadily fixed onto the skin, the normal adhesive force of the dry adhesive patch with two sets of pillar (diameter of 11μm and 13μm) and different ratio of pillar spacing vs pillar diameter (range from 20/11 to 3) was characterized. The adhesion strength was measured up to 10 repeating cycles for each sample by Instron Microtester 5848 (Instron, USA). The sample was attached onto the glass or skin and the normal force was applied by the Microtester from the backside to peel the dry adhesive off. The maximum force was recorded as the adhesive force. **Figure 5.3 (a)** and **(b)** show the adhesive force on glass and skin of each cycle. The dry adhesive was cleaned with acetone after each cycle to prevent the contamination and recover the adhesive force. The sample with 20μm pillar spacing can achieve higher adhesive force than the sample with 24μm pillar spacing when the pillar diameter is 11μm. For the test on the glass, the adhesive force does not have an obvious decline as shown in **Figure 5.3 (a)**. However, for the test on the skin, there is a decline of the adhesive force when repeating the test cycles. This is because

the deformable skin will cause more damage on the mushroom top when the dry adhesive was pressed onto skin surface. Thus repeating the test cycles will accumulate the damage of mushroom and further reduce the adhesive force.

The characterization of the adhesive force on the glass and skin by changing the pillar spacing for pillars of 11μm and 13μm diameter is shown in **Figure 5.3 (c)** and **(d)**. The test results agree with the data in **(a)** and **(b)**. The adhesive force decreases when the spacing increases. And the adhesive force of the patch with 13μm diameter is a bit lower than that with 11μm due to the lower pillar aspect ratio when the pillar diameter is higher. Base on the characterization of the dry adhesive force, we can conclude that the sample with 11μm pillar diameter and 20μm pillar spacing can achieve the highest adhesive force. Therefore, this parameter is adopted for the dry adhesive to be integrated on the patch of complete device.

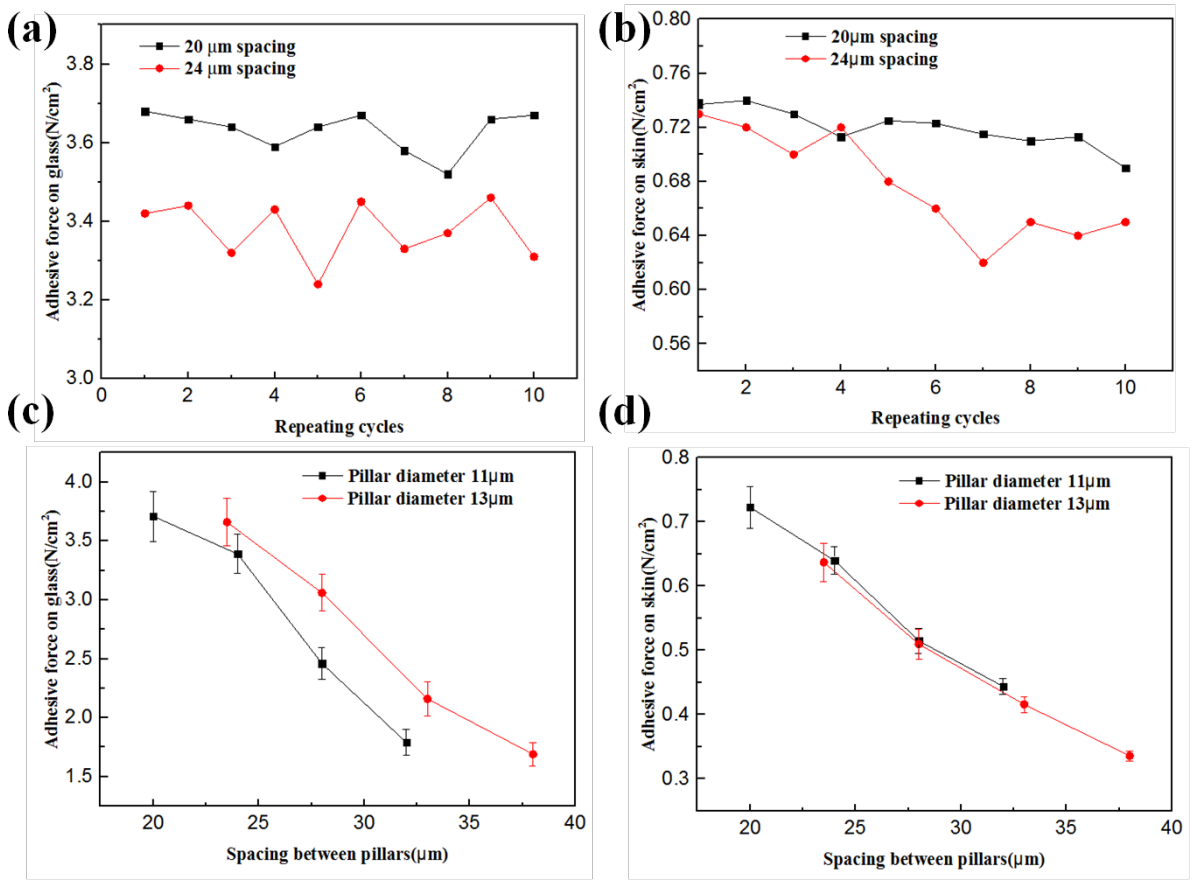

Figure 5.3 Characterization of the adhesive force of dry adhesive patches by changing the pillar diameter and pillar spacing. Adhesive force test by repeating 10 cycles on glass (a) and on skin(b). After each test cycle, the dry adhesive patch was cleaned by acetone. The diameter of the pillar is 11μm; Average adhesive force of the dry adhesive patches on glass(c) and skin(d) for samples with pillar diameter of 11μm and 13μm.

5.3 Characterization of the TEH patch

5.3.1 Comparison of the TEH patches with different surface micro-patterns

A dielectric PDMS layer with micro-patterns was used to enhance the effective surface area and output voltage. Here we studied the performance by using micro-pillar with and without mushroom top and pyramid as the micro-patterns. At the backside of the dielectric PDMS layer, a Cu layer of 200nm thickness was deposited by thermal evaporation. Then a Kapton layer was attached above the Cu layer to protect the metal from scratching and friction. As mentioned before, to adapt the different locations for our patch to be applied, we developed two methods to generate

power. For the first case when the patch is applied on flat skin as shown in **Figure 5.4 (a)**, the distance between two dry adhesive patches is a bit shorter than the original length of the TEH patch, making the TEH patch bent upward and having no contact with skin surface (**Figure 5.4 (a-1-i)**). Then the TEH patch is pressed by finger and contact with the skin surface, as shown in **Figure 4(a-1-ii)**, then is separated from skin again by lifting up the finger as shown in **Figure 5.4 (a-1-iii)**. Due to the sticky surface of PDMS, once the TEH is attached onto the skin, it cannot separate from skin without a pulling force. Thus, a dry adhesive patch is assembled at the backside of the TEH patch, providing the pulling force by having the adhesive force between the finger and dry adhesive patch. The detailed charge transport process is shown in **Figure 5.4 (a-2)**. When the TEH patch was pressed onto the skin surface (**Figure 5.4 (a-2-i)**), there is charge transport between them. According to the triboelectric theory, electrons are transferred from the PDMS to the skin during the electrification process, since PDMS is more triboelectrically negative than skin as shown in **Figure 5.4 (a-2-ii)**. The change of the negative charges on the surface of the PDMS induces positive charges on the Cu electrode, driving free electrons to flow from the Cu layer to the ground. An output voltage or signal is generated. Once the finger is lifted up, making the PDMS and skin separated (**Figure 5.4 (a-2-iii)**), the recovery of the surface negative charge on PDMS surface will induce a backflow of electrons from ground to Cu electrode. An opposite signal will be generated.

According to the V–Q–x relationship for contact-mode TEHs [119], the output voltage is determined by the following equation:

$$\boldsymbol{V = E_{dielectric} \times d + E_{air} \times x} \quad \text{.....(1)}$$

where $E_{dielectric}$ is the electric field though the dielectric layer, which is PDMS layer here, generated by the tribo-charges on the opposite sides of the TEH; d is the thickness of the dielectric

layer; E_{air} is the electric field though the spacing between the top surface of TEH and contact surface, this electric field is generated by the tribo-charges on the TEH surface and contact surface; x is the spacing between the TEH surface and contact surface. The output voltage should increase with the increase of the spacing between the TEH surface and contact surface in the ideal fully contact-mode TEHs. Thus to achieve the maximum output power, the TEH should be lifted up as high as possible. The maximum height to be lifted up is determined by the spacing between the two adhesives. When this spacing decreases, the TEH can bend upward more and have a large distance away from the skin surface. However, a shorter spacing between the two dry adhesive patches also decreases the effective contact area between the TEH patch and skin. It will further lower the quantity of the tribo-charges to be generated. The spacing between the two dry adhesive patches is optimized in **Figure 5.5** to achieve a maximum lift-up height. The adhesive force should provide a certain adhesive force to lift up the TEH to the maximum height. Otherwise, before the TEH is lifted up to the maximum height, the finger will detach from the dry adhesive because of the insufficient pull force. Based on the adhesive force characterization in **Figure 5.4**, output voltage of dry adhesive patches with different adhesive forces are tested in **Figure 5.5**. The dry adhesive with highest output voltage was selected to be assembled at the backside of the TEH for output power characterization in **Figure 5.4 (b)** and **Figure 5.4 (c)**.

In order to calculate the power generated by the TEH, a load resistor was connected between TEH patch and ground. The finger pressing of 2Hz frequency was applied to generate the power. The voltage was then measured across the load resistor to obtain the power generated by the TEH. As the load resistance was increased, the power output increased, peaked at a point, and then started dropping thereafter. The voltage and power characteristics of TEH with different surface micro-patterns and load resistance are shown in Fig 5(b) and 5(c). The maximum power

output for TEH patch with pillar with and without mushroom top assembly and pyramid are 11.79 μW, 13.3 μW and 15.21 μW, respectively; when the load resistance values are approximately 23.08 MΩ, 37.5 MΩ and 44.44 MΩ, respectively, as shown in **Figure 5.4 (c)**. This load resistance for peak output power represents the inner impedance of the TEH patch. The TEH with pyramid surface micro-patterns generates a higher voltage and output power, but also gives a higher inner impedance. The inner impedance is determined by the following equation:

$$R_{opt} \approx \frac{(d_0 + x_{\max})^2}{Sv\varepsilon_0} \qquad \text{.....(2)}$$

where R_{opt} is the inner impedance; d_0 is the thickness of the PDMS layer; x_{max} is the maximum height to be lifted up for TEH patch; S is the effective area size of TEH patch which can be altered by the surface micro-patterns; v is the speed of the TEH to be lifted up; ε_0 is the dielectric constant of air.

For the TEH patches whose surface micro-patterns are pillar with and without mushroom tops, the contact surface is stickier than the TEH patches with pyramid surface micro-pattern. Thus when the TEH patches were lifted up, TEH with pyramid surface micro-pattern has a faster detachment from skin, thus with a higher v, result in a narrower and higher output voltage pulse. However, when the height of the micro-pillar, which is 20μm, is much higher than the height of the pyramid, which is 1.37μm, the micro-pillar structure can provide a higher S, effective area size of TEH patch, than the pyramid structure and further lower the inner impedance.

Another method to generate the power is to attach the device to the joint. In this case, when people bend and straight their joint, the skin will be stretched and compressed, making the TEH patch contact and detach the skin. Thus, the dry adhesive on the backside of TEH patch is not required. The test result of the output voltage and output power is shown in **Figure 5.4 (d)** and **(e)** showing the same trend as that of **(b)** and **(c)**. The maximum power output for TEH patch with

pillar with and without mushroom top assembly and pyramid are 12.4 μW, 13.4 μW and 15.6 μW, respectively; when the load resistance values are approximately 28.1 MΩ, 37.7 MΩ and 46.8 MΩ, respectively.

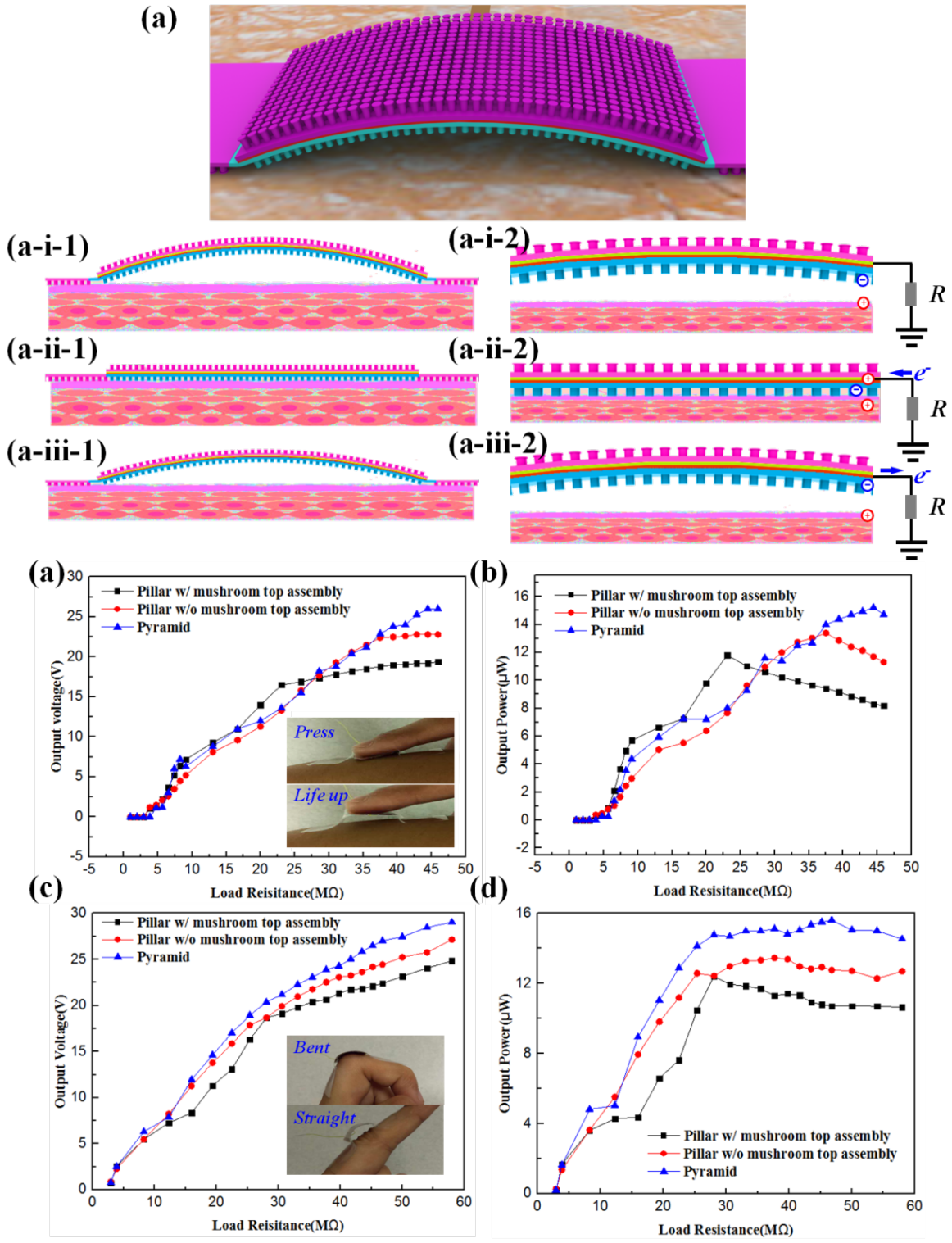

Figure 5.4 (a) Working principle of the TEH patch when applied on flat skin surface; Characterization for the TEH output voltage(b) and power(c) when applied on flat skin; Characterization for the TEH output voltage(d) and power(e) when applied on finger knuckle.

5.3.2 Optimization for TEH patch configuration

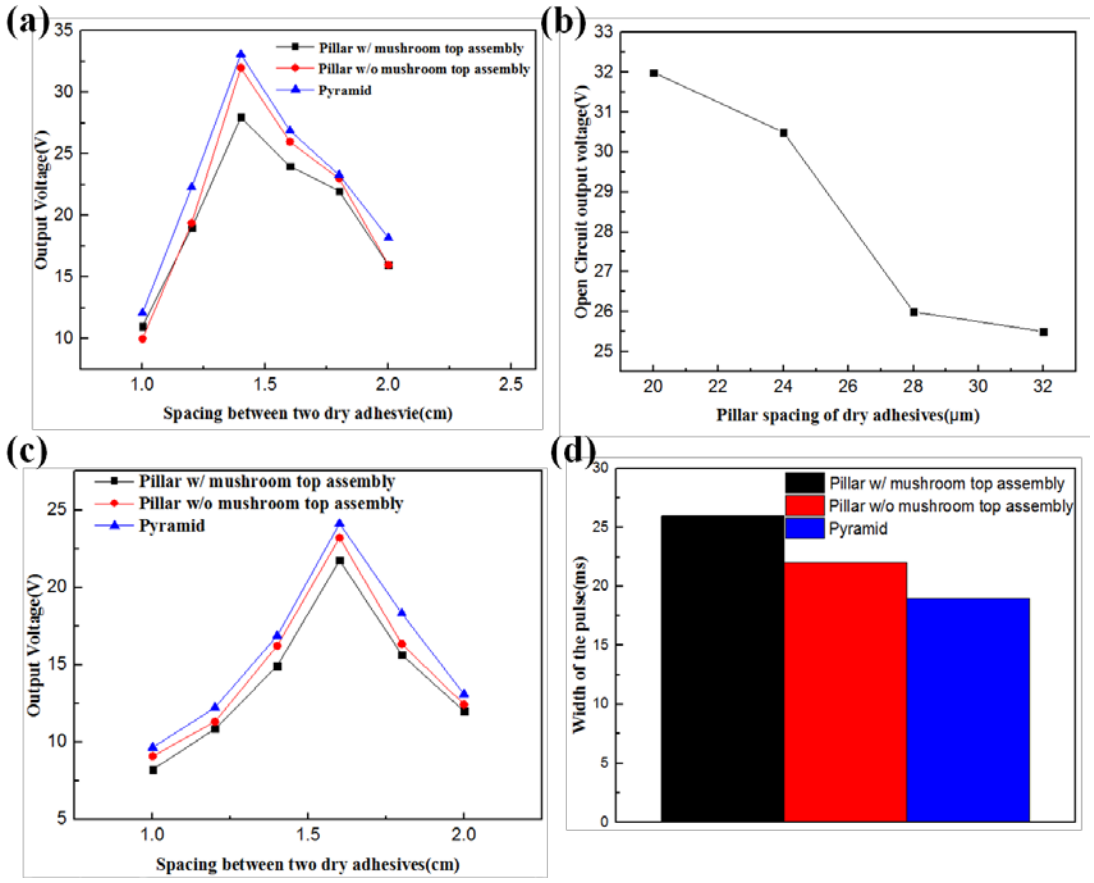

Figure 5.5 Open circuit voltage by changing the spacing between two adhesive for the TEH attached on arm; (b) Open circuit voltage by changing the pillar spacing of the dry adhesive patch at the backside of the TEH patch; (c) Open circuit voltage by changing the spacing between two adhesive for the TEH attached on finger knuckle; (d) Average width of the pulse for the signal in (a).

The spacing between the two dry adhesive patches beside the TEH patch will affect the maximum height to be lifted up and further affect the maximum output voltage. The test results of the output voltage of the TEH patch by changing the spacing between two dry adhesive patches for the situation when the TEH was applied on arm is shown in (**Figure 5.5** (a)). The length of the TEH patch is 2cm. Thus the spacing between two dry adhesive patches decreases from 2 cm to 1cm with 0.2cm step. The output voltage peaks at 1.4cm because the increase of the height to be lifted up. Then it declines by reducing the spacing because the effective contact area reduces when

the spacing is too low. For the situation when the TEH patch was applied on finger knuckle, the rest results are shown in **Figure 5.5** (c). The output voltage peaks at 1.6cm. Another fact will affect the lift- up height is the adhesive force of the dry adhesive patch assembled at the backside of the TEH patch. If the adhesive force is not sufficient, it will detach from finger before the TEH patch is lifted up to the maximum height. Based on the adhesive force characterization in **Figure 5.4**, we selected the sample of 11μm and pillar spacing ranges from 20μm to 32μm in the test. In this test, only micro-pillar without mushroom top is used. As shown in **Figure 5.5** (b), the voltage decrease with the increase of the pillar spacing because of the reduction of the adhesive force. Only the dry adhesive patch with 20μm spacing can give the highest output voltage which indicates that the highest lift-up height. The width of the pulse for the signal measured in **Figure 5.5** (a) is shown in **Figure 5.5** (d). As mentioned in paper, because the TEH patch with pillar-based micro-pattern is stickier than that with pyramid micro-pattern, thus it takes longer time to detach from skin surface and generate a broader pulse. The average width of the pulse for pyramid, pillar with and without mushroom top assembly is 19ms, 22ms and 26ms, respectively.

5.4 Conclusion

We developed a stretchable wearable flexible medical device for transdermal drug delivery. Unique bendable microneedles were proposed to overcome the safety issue associated with the microneedle breakage during the application. The PDMS mix ratio and pillar spacing are optimized for a maximum buckling force to enhance the skin penetration success rate. To adapt the applications for water-soluable and lipophilic drug formulations, two kinds of microneedle configurations are developed. Microneedles with SU-8 sharp tips are more suitable for the storage of water-based drugs while microneedles with maltose sharp tips are more suitable for the storage of lipid-based drugs. We leverage the dry adhesive as the fixation method to realize a conformal

attachment. The micro-pillar structure achieved in fabrication of dry adhesive is also investigated as a TEH patch which is a promising energy source for other active components. Two methods for power generation, based on different positions for skin patch to be attached, were developed and characterized. Thus the TEH patch can generate power no matter the patch is attached on flat skin or joint part.

Chapter 6 Towards self-powered Microneedle skin patch integrated with Triboelectric liquid volume sensor for lab-on-chip applications

For the treatment of diseases such as type 2 diabetes and osteoporosis, multiple drug injections per day with dose control of each injection will be necessary. Thus, large delivery volume and a precise control mechanism are desirable features for wearable skin patch drug delivery system but not developed yet. It means within the skin patch, a liquid volume sensor with proper mechanism should be integrated with the fluidic system for drug loading and delivery. Moreover, a standalone wearable drug delivery skin patch with capability of health monitoring, signal processing and interfacing with external cloud computing apparatus, an built-in energy source is inevitable to power components such as integrated circuits (ICs), microprocessor, liquid-crystal display (LCD) reading panel, drug delivery and control actuators, and diversified sensors, e.g., glucose sensor.

In this chapter, we report a LoC drug delivery patch with manually-controlled drug delivery function and power source which is suitable for further integration with other active components for more applications. The key innovation of our design is that the liquid volume could be sensed by a triboelectric mechanism using the same materials for LoC. Thus the delivery volume can be well measured and controlled during the drug delivery process. The bendable microneedle array was assembled onto the patch to confirm the drug control function by insulin delivery tests on rats. By leveraging the similar triboelectric mechanism as the liquid sensor, we developed and optimized a stacked layer design triboelectric energy harvester(TEH) which is suitable to be

attached onto the patch as an energy source. Such energy source can be used to support the operation of other components.

6.1 Structure and fabrication process

6.1.1 Structure of the skin patch

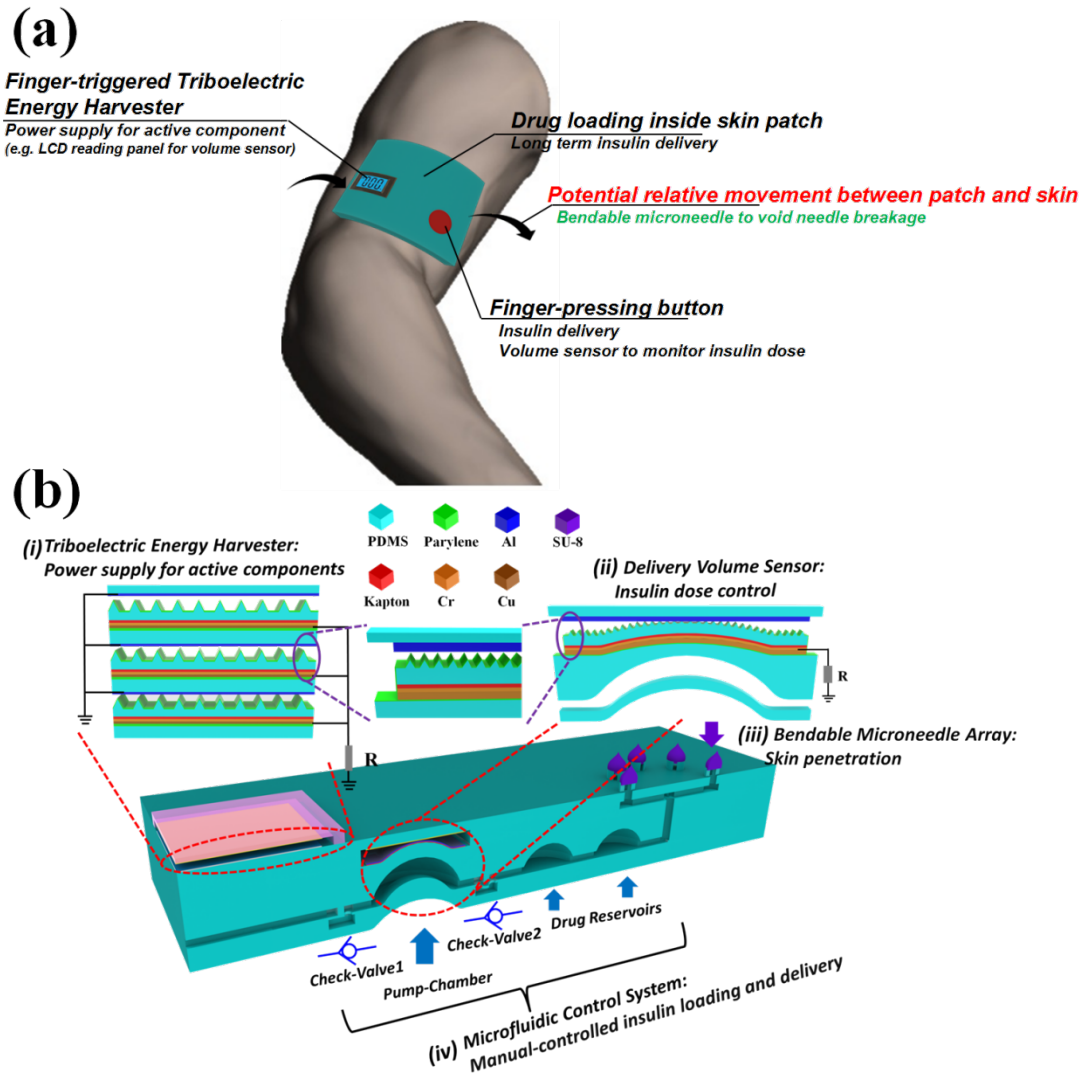

Figure 6.1 (a) Concept of the flexible microneedle skin patch attached on skin; (b) Detailed structure and functional components of the flexible microneedle skin patch with manual-controlled insulin delivery and delivery volume monitoring function. (i) TEH assembled on the top surface of the skin patch as power source for other functional active components to be integrated in the future; (ii) Delivery volume sensor using triboelectric mechanism to measure the drug volume to be delivered and control the insulin dose; (iii) Bendable microneedle array for skin penetration; (iv) Microfluidic control system including a pump chamber, two check-valves and drug reservoirs; insulin can be loaded and delivered by pressing the pump chamber.

We propose a flexible microneedle skin patch with manually-controlled drug delivery, dose volume monitoring, bendable microneedles and TEH as shown in **Figure 6.1**. The whole device consists of four functional components: microfluidics control system, bendable microneedle array for skin penetration, delivery volume sensor and TEH.

The microfluidics control system has four parts: two check-valves in series, a pneumatic pump-chamber between these two check-valves, several drug reservoirs in series and microfluidic channels connecting all these components. By having this microfluidics control system, drugs can be manually loaded and delivered.

The bendable microneedle array, connected with the microfluidic control system by a vertical channel, is assembled onto the top surface of the microneedle patch. After skin penetration, drugs stored in the drug reservoirs will be delivered into skin through this microneedle array when we use fingertip to press the pump chamber.

The main component of the delivery volume sensor above the pump chamber leverages the triboelectric sensing mechanism which has yet been demonstrated as liquid volume sensor. Currently, triboelectric sensing mechanism has been investigated in terms of chemical sensor[120-123], pressure sensor[124-126], motion sensor[127-133] and tactile sensor[134-136] because of its advantage of easy fabrication and self-powered feature. Here we assembled a triboelectric layer pair with the same area as the pump chamber, i.e., of 1.2×1.2 cm^2 for sensing delivery volume.

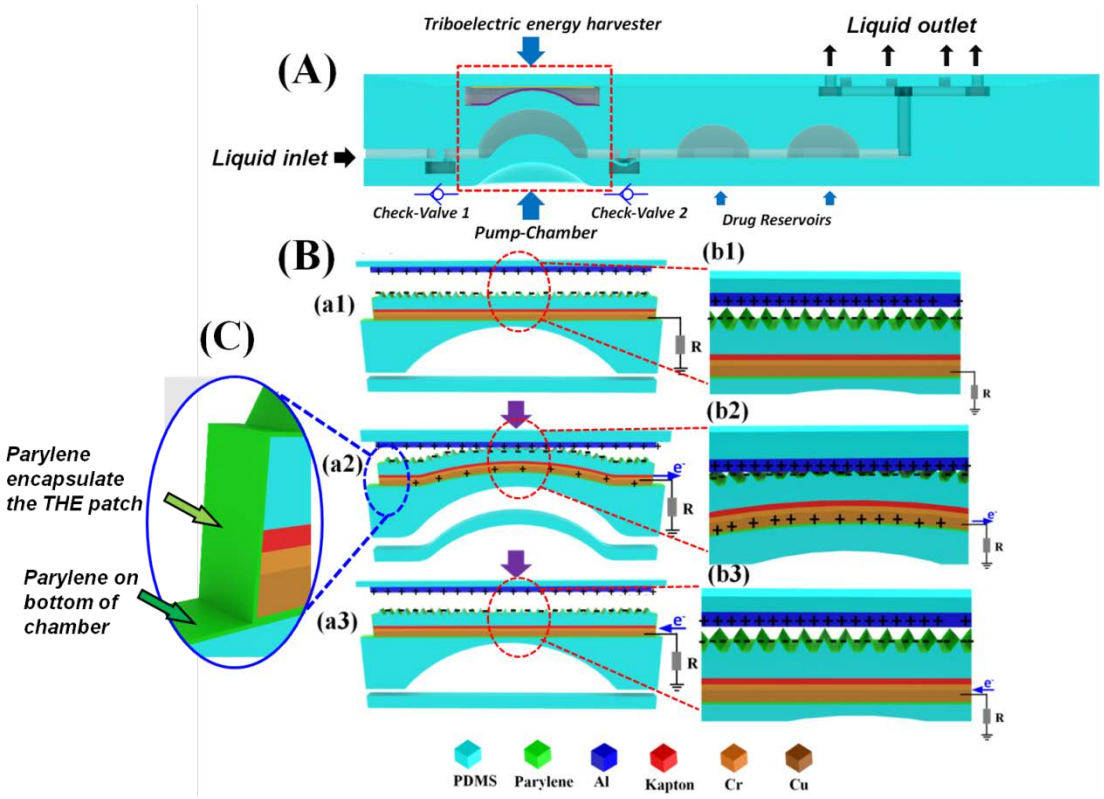

Figure 6.2 (A) Cross-sectional view of the lab-on-chip drug delivery patch; (B) Working principle of the TEH for the delivery volume sensor; (b1) to (b3) shows the a magnification of layer structure and charge polarity in (a1) to (a3).(C) Detailed image shows the parylene layer to encapsulate the TEH patch and coated on the bottom of the chamber.

A detailed cross-sectional view of the device without microneedle is shown in **Figure 6.2**. The microfluidics control system has four parts: two check-valves in series, a pneumatic pump-chamber between these two check-valves, several drug reservoirs in series and microfluidic channels connecting all these components. By pressing the pump chamber, the liquid will be sucked into the channel from the inlet and delivered out from the outlet as shown in **Figure 6.2** (A). The detailed structure and working principle are shown in **Figure 6.3**.

Figure 6.2 (B) shows a detailed structure of the TEH assembled for liquid volume sensor. A dielectric PDMS layer with pyramid shape micro-patterns was used to enhance the surface area and output voltage. Underneath the PDMS layer, a Kapton tape was attached as an intermediary

layer for metal deposition. To have a better adhesion between Cu and Kapton, a Cr layer was deposited before the deposition of Cu layer. In order to protect the metal layer, a parylene layer was coated by CVD onto the whole surface of the TEH, including the PDMS top surface. Then the TEH was assembled in a PDMS chamber with Al layer coated on the ceiling.

In the original position, the surface of the TEH and ceiling are not in contact (**Figure 6.2** (a1) and (b1)). When the bottom layer of the pump chamber is pressed, the liquid or the air in the in the pump chamber will be compressed and the top layer of the pump chamber will also be deformed. This deformation will induce a contact between the top layer of the TEH and the ceiling of the PDMS chamber, resulting in charge transport between them (**Figure 6.2** (a2) and (b2)). According to the triboelectric theory, electrons are transferred from the parylene to the Al during the electrification process, since parylene is triboelectrically negative and Al is triboelectrically positive. The change of the negative charges on the surface of the parylene can induce positive charges on the Cu electrode, driving free electrons to flow from the Cu layer to the ground. An output voltage or signal is generated. Once the pressing is released, the parylene and Al surfaces are separated (**Figure 6.2** (a3) and (b3)). The recovery of the surface negative charge on parylene surface will induce a backflow of electrons from ground to Cu electrode. An opposite signal will be generated. The output voltage is generated by the contact between parylene and Al and it is determined by the contact area. And this contact area is also determined by the deformation of the pump-chamber, which is related with the delivery volume. Thus, based on the output signal, the delivery volume can be measured.

To avoid the interference from the backside of the TEH, the bottom of the chamber is also coated with parylene as shown in **Figure 6.2** (C). Thus, the backside of the TEH and the bottom

surface of the chamber are of the same material. The contact of these two interfaces will not generate any output voltage.

To achieve the highest voltage, the surface materials of the triboelectric layer pair should be optimized. The gap between the top and bottom of the delivery volume sensor is critical to measurement accuracy of the liquid volume sensor. To ensure a good accuracy of this delivery volume sensor, this gap is also optimized.

6.1.2 Structure and working principle of the pump and check-valves for microfluidic control system

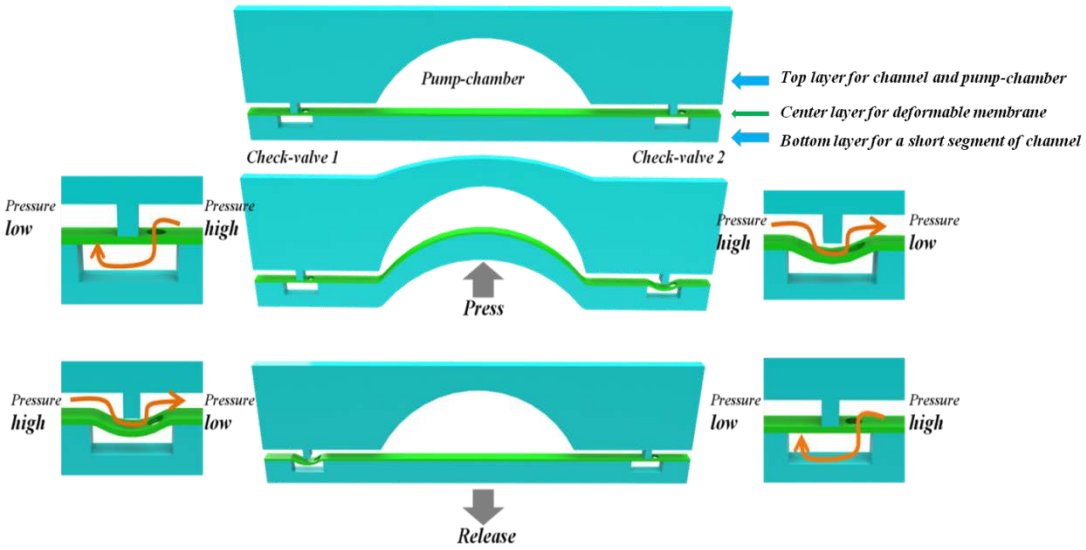

Figure 6.3 Structure and working principle of the pump chamber and check-valves.

The design and working principle of the pump-chamber and check-valves are illustrated in **Figure 6.3**. The pump -chamber is located between two check-valves. The check-valve has three parts: a thin PDMS membrane layer with a hole, a top layer that contains a discontinuous channel, and a bottom layer that contains a short segment of a channel. The device was formed by bonding these three layers together. But the contact area between the protruding poster of the top layer and center membrane layer should not be treated with Oxygen plasma. When pressure applied, the

center membrane could detach from the top layer and deform. During the plasma treatment, the contact area will be covered by a piece of Al foil. These two check-valves ensure that the liquid or air can only enter the pump-chamber through one valve, and leave the pump-chamber through the other. Due to the elasticity of PDMS, when the bottom layer of the pump-chamber is pressed and deformed, the pressure in the pump-chamber will increase. For check-valve 1, this high pressure in the pump-chamber will make the chamber below the membrane expand. Thus the membrane will be pushed and attach tightly onto the protruding poster of the upper layer, sealing the channel. Then check-valve 1 is off. For check-valve 2, this high pressure in pump-chamber will push the membrane of the check-valve 2 and make it deform. Then check-valve 2 is on and the air or liquid in the pump chamber can pass through. When the bottom layer of the pump-chamber is released, the pump-chamber tends to recover its initial shape. Thus the pressure in pump-chamber is low. This low pressure in the pump-chamber will make the membrane of check-valve 1 have a downwards deformation. Then the check-valve 1 is on and the air or liquid outside the device can be sucked into the pump-chamber. Meanwhile the low pressure in pump-chamber will make the membrane of check-valve 2 have an upwards deformation and seal the channel. Then check-valve 2 is off.

In summary, one check-valve can be on only when another check-valve is off. Then a one directional flow can be formed by pressing the pump chamber.

6.1.3 The fabrication process of the TEH

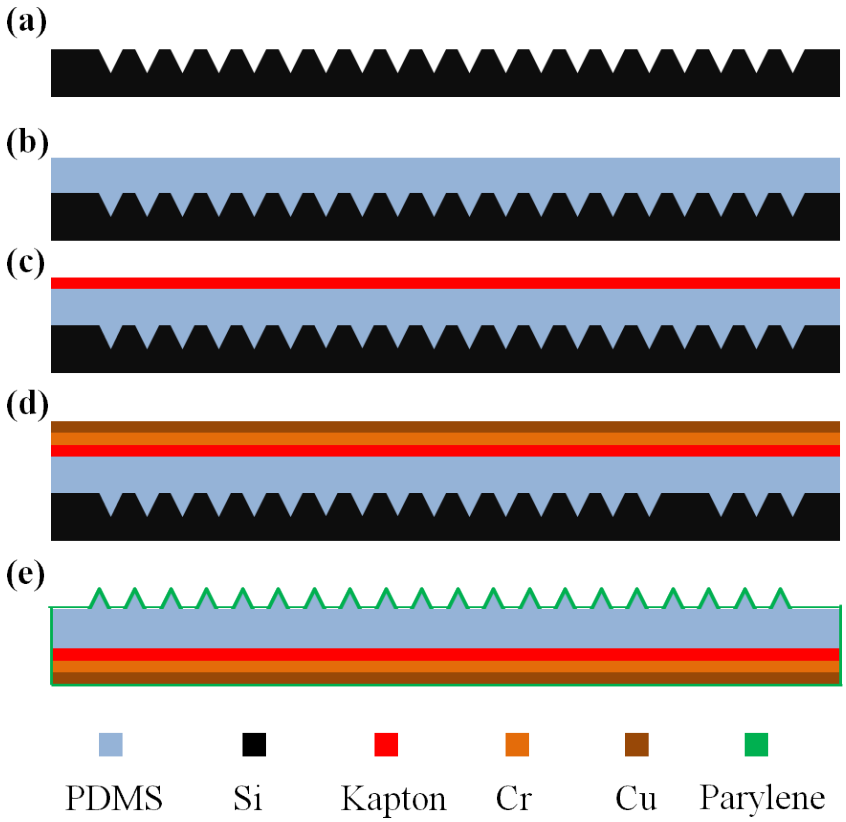

Figure 6.4 Fabrication process of the TEH

Figure 6.4 shows the fabrication process of the TEH used for energy harvester and delivery volume sensor. The process of the TEH fabrication started from a Si wafer with pyramid shape holes as shown in (a). A PDMS layer was coated and cured onto the Si mold as shown in (b). The thickness of the PDMS layer was controlled by the spin rate of the spin coater. Then attach the Kapton tape at the backside of the PDMS layer as shown in (c). Two layers of metal were coated onto the Kapton tape by evaporation as shown in (d). The first layer of Cr is to enhance the adhesion between Cu and Kapton tape. Then PDMS layer with Kapton and metal layers was released from the Si mold and encapsulate it with parylene by CVD. This parylene layer can protect the metal from peeling off by scratch and contact with adhesive surfaces. In the test, the backside metal layers of the TEH were assembled onto PDMS surface which is adhesive. Thus if without

the parylene coating, the metal may detach from the TEH because of the contact with the adhesive PDMS surface.

6.1.4 Fabrication process of the LoC drug delivery patch

The fabrication process of the LoC drug delivery patch is as shown in the **Figure 6.5**. Two SU-8 molds were prepared first. The first SU-8 mold was for the upper layer of the check-valve, pump-chamber, drug reservoirs and fluidic channels ((a1) to (a2)). The SU-8 layer was coated and patterned on a glass wafer as shown in (a1). On this SU-8 mold, there were bases for pump-chamber and drug reservoirs. Then SU-8 of liquid phase was dipped onto the SU-8 base and formed hemispheres as shown in (a2). Previous research reveals that the maximum skin absorption rate is around 33μL/day for each microneedle[143]. Considering the microneedle array has 8 microneedles in our design, the total drug solution can be delivered in one day is around 264 μL. Thus by controlling the volume of SU-8 dipped onto the substrate to form the drug reservoir, the total volume of the drug reservoir is 270 μL. The sample was baked to make the SU-8 hemispheres solidified. Then the sample was exposed with UV light and post baked to make the SU-8 crosslink. The second SU-8 mold is for the fluidic channels for microneedle array and chamber for TEH delivery volume sensor as shown in (b). To have a well control of the spacing of the chamber, a glass slide of certain thickness was attached onto the base of the chamber. Then the SU-8 molds of (a2) and (b) were face to face aligned and fixed with a spacer at the edge. The space between these two SU-8 molds was filled with PDMS as shown in (c1). These fixed SU-8 molds with PDMS in between were kept at room temperature for 24 hours without baking to avoid the air bubbles within the PDMS layer. Then sample was cured at 75ºC for 30 minutes. The sample was cooled down to room temperature and release these two SU-8 molds from the PDMS layer as shown in (c2). This PDMS layer has patterns on both sides and acts as the main body of the device. The top side has the channels for microneedle array and the bottom layer has the pattern for

microfluidic control system. To have the top PDMS layer for microneedle pillar array, a third SU-8 mold was prepared ((d1) to (d3)). For this SU-8 mold, a SU-8 layer with hole array was patterned as shown in (d1). The holes were for the four-beam PDMS pillars. Then a pillar array was aligned to the hole pattern as the second SU-8 layer. The second layer is for the vertical channel connecting to the channel array on the top layer of (c2) with the microneedles which will be assembled later. Then PDMS was coated onto the SU-8 mold to fill the hole pattern and form a whole layer above the SU-8 mold as shown in (d3). The thickness of the PDMS layer (150 μm) was lower than the thickness of the height of the SU-8 pillar (350 μm). Thus the top of the SU-8 pillar was not covered by PDMS. This SU-8 mold can create a penetrated hole through the PDMS layer and form a vertical channel inside the microneedle. Make the sample of (d3) face down and bonded to the top surface of main body as shown in (c2). Then the SU-8 mold was released as shown in (c3). Now at the top surface of the main body of the device, a PDMS pillar array was aligned and connected to the channel array. Then for the bottom surface of the main body, two PDMS layer was needed to form the two check-valves. Thus two SU-8 molds were required. (e1) shows the SU-8 mold for the bottom chambers of check-valves. Then a thick PDMS layer was coated onto the SU-8 mold. Then cured PDMS was released as shown in (e2). (f1) shows the SU-8 mold for the holes on the center membrane layer of the check-valves. Then a thin layer of PDMS was coated onto the SU-8 mold as shown in (f2). To create penetrated holes on this membrane layer, the thickness of the PDMS (40 μm) is lower than the height of the SU-8 pillar (350 μm). The PDMS layer of (e2) with (f2) were aligned as shown in (g1) and bond them together (g2). Then the bonded the PDMS layers were released from the SU-8 mold as shown in (g3). These bonded PDMS layers have the membrane with holes and chambers for the check-valve. These PDMS layers were aligned and bonded to the bottom surface of the main body as shown in (c4). Then the sharp tips were

assembled onto the PDMS pillar array as shown in (c5). This sharp tip assembly is realized by drawing lithography. Then the TEH was fixed at the bottom of the sensor chamber and a PDMS with Al coating was bonded above to seal the chamber as shown in (c6).

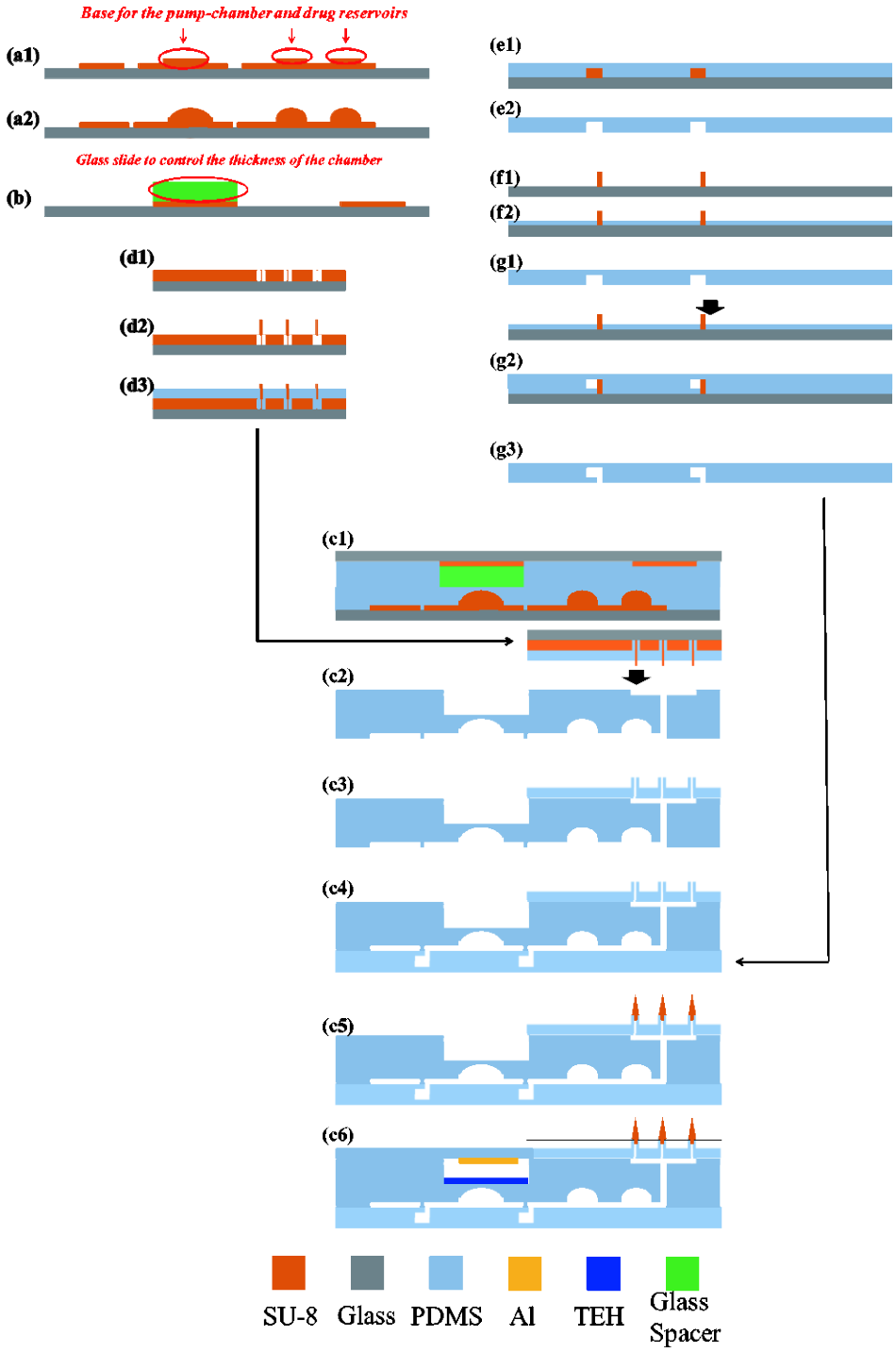

Figure 6.5 Fabrication process of the LoC drug delivery patch

6.2 Characterization and optimization

6.2.1 Optimization and characterization of the surface materials of the triboelectric layer pair

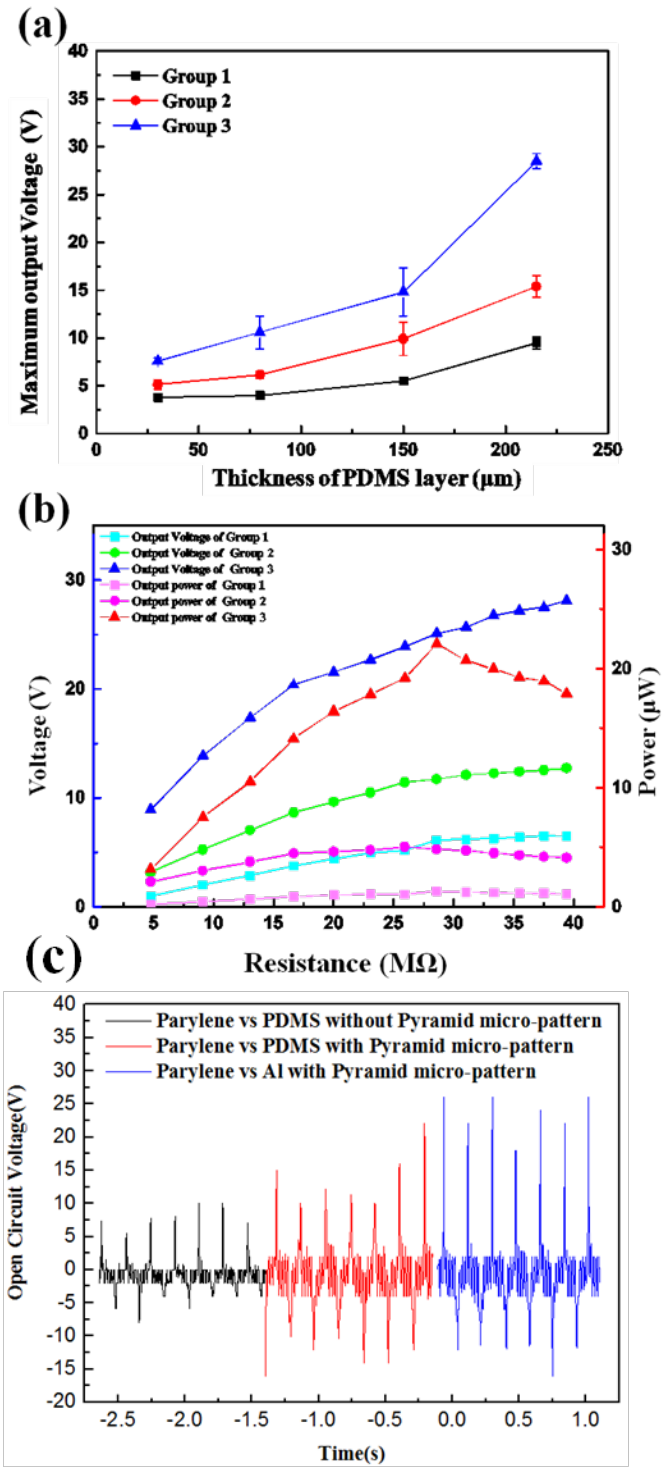

Figure 6.6 Optimization for PDMS thickness and material of contact surfaces; (b) Characterization of the output power; (c) Output voltage over time of the different triboelectric surface pairs when the thickness of the PDMS layer is 200μm.

To enhance the sensitivity of the delivery volume sensor, the output voltage of the TEH is expected to be as high as possible. Here we investigated the effect of surface pyramid micro-pattern, material of contact surface and the thickness of the PDMS dielectric layer. Three groups of samples with different PDMS thickness are prepared as shown in the following table.

Table 6.12 Details of groups of sample for optimization of PDMS thickness and contact surfaces

Group No.	Surface micro-pattern	Contact surface	Thickness of dielectric layer
Group 1	Without pyramid micro-pattern	Parylene vs PDMS	30 μm
			80 μm
			150 μm
			215 μm
Group 2	With pyramid micro-pattern	Parylene vs PDMS	30 μm
			80 μm
			150 μm
			215 μm
Group 3	With pyramid micro-pattern	Parylene vs Al	30 μm
			80 μm
			150 μm
			215 μm

In the test, the TEH patches were fixed onto a force gauge and applied onto the PDMS or Al contact surface with the same force, which is 10 N. To make the open circuit output voltage of TEH reaches the maximum value, the surface of TEH is fully contacted with PDMS or Al surface.

The experimental measurement data is shown in **Figure 6.6** (a). According to the V–Q–x relationship for contact-mode TEHs, the output voltage is determined by the following equation:

$$V = E_{dielectric} \times d + E_{air} \times x \qquad (1)$$

where $E_{dielectric}$ is the electric field though the dielectric layer generated by the tribo-charges on the opposite sides of the TEH; d is the thickness of the dielectric layer; E_{air} is the electric field though the spacing between the top surface of TEH and contact surface, this electric field is generated by the tribo-charges on the TEH surface and contact surface; x is the spacing between the TEH surface and contact surface. The output voltage should increase with the increase of the dielectric layer thickness in the ideal fully contact-mode TEHs.

For group 1, there is no pyramid micro-pattern on the surface of TEH. The two contact surfaces are parylene and PDMS. The output voltage increases from 3.8 V to 9.5 V when the thickness of PDMS dielectric layer increases from 30 μm to 215 μm, which is consistent with the equation (1).

For group 2, there are pyramid micro-patterns on the surface of TEH. The two contact surfaces are the same as group 1. Compared with the samples of group 1, the output voltages of the samples of group 2 have about 50% enhancement with the same PDMS thickness. The output voltage increases from 5.2 V to 14.6 V when the thickness of the PDMS dielectric layer increases from 30 μm to 215 μm. Thus the pyramid micro-pattern on the surface of TEH can enhance the output voltage by 50%.

The samples of group 3 are the same as group 2. To further increase the output voltage, we changed another contact surface from PDMS to Al. Since Al is more triboelectrically positive than PDMS, these contact surfaces of parylene and Al could generate higher output voltage. For the samples of 30 μm, 80 μm and 150 μm, the output voltages are about 50% higher than their counterparts of group 2. For the sample of 215 μm thickness, the output voltage has 100% enhancement than the sample with the same thickness of group 2. This maybe induced by the too thick layer of PDMS. During the test, not only the surface pyramid micro-patterns get deformation,

but the PDMS layer itself also got serious deformation which induced more charge transport. Thus the enhancement of the output voltage of thicker PDMS dielectric layer is much higher than that of thinner PDMS dielectric layer.

The output power for each group by changing the load resistance is shown in **Figure 6.6** (b). The change of the maximum output power for each group follows the same trend as that of open circuit output voltage as shown in **Figure 6.6** (a).

6.2.2 Optimization and evaluation of the liquid flow sensor

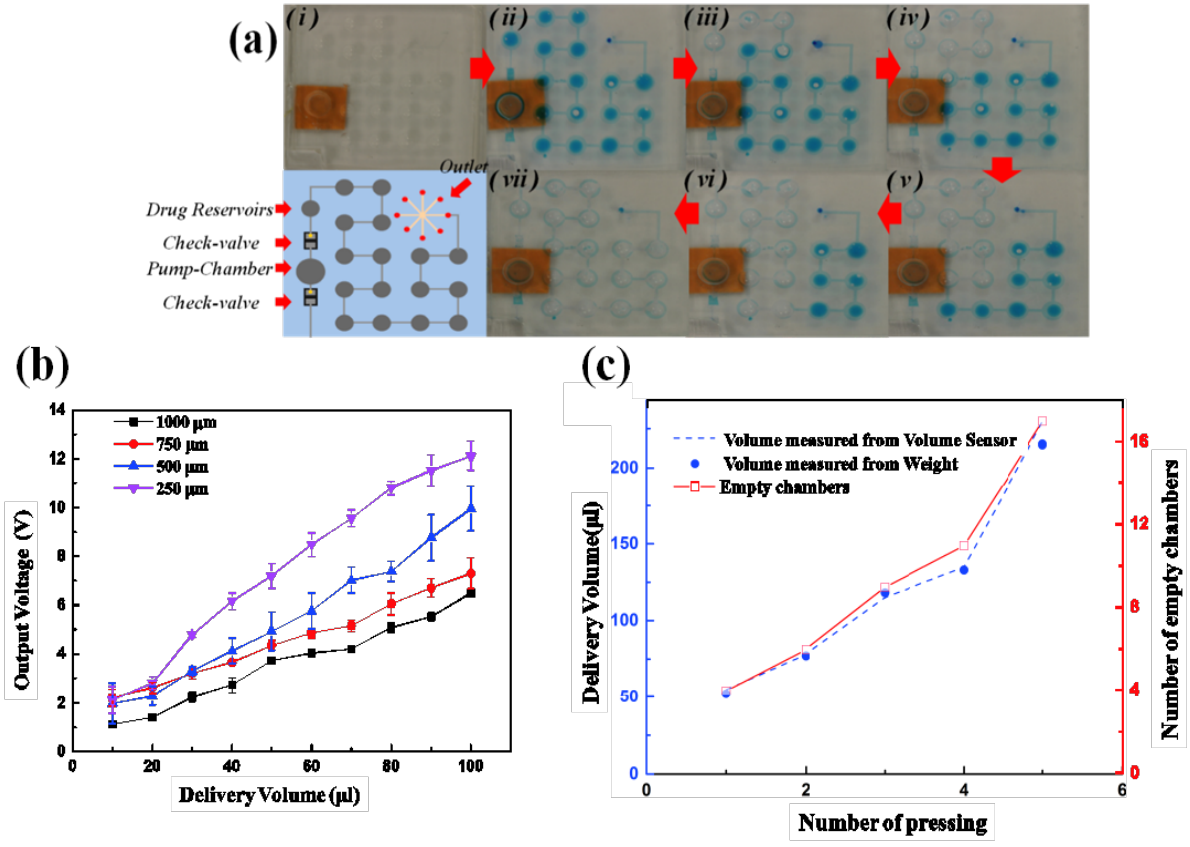

Figure 6.7 Volume sensor monitors the delivery volume of each pressing of the pump chamber. (a) Demonstration of the drug delivery with volume sensor monitoring; (b) Optimization for spacing between the top and bottom surface of the triboelectric pair; (c) Delivery volume calibration with different measuring method.

In equation (1), the spacing between the top surface of the TEH and another contact surface is also another parameter to determine the output voltage. In order to investigate the effect of the spacing between the TEH surface and contact surface, which is the height of the PDMS chamber, we changed the spacing from 250 μm to 1000 μm. In this test, the TEH samples are with pyramid surface micro-pattern and of 215 μm PDMS thickness, which are the samples generating the highest output voltage in **Figure 6.7**(a). The sample was assembled above the top layer of pump-chamber as shown in **Figure 6.1** and **Figure 6.2** (A). The bottom layer of the pump-chamber was pressed to delivery solution of certain volume within the range from 0.01 ml to 0.1 ml. The output voltage was recorded and the relation between the delivery volume and output voltage is shown in **Figure 6.7** (b). According to the equation(1) for fully contact-mode TEHs, the output voltage will increase with the increase of the spacing. But as shown in **Figure 6.7** (a), the output voltage decreases with the increase of the spacing. This is because the TEH shown in **Figure 6.1** and **Figure 6.2** is not working in fully contact-mode. With the same deformation of the top layer of the pump-chamber, the contact area decreases with the increase of the spacing. Although the TEH could give higher output voltage when the spacing was lower, the standard deviation was also higher, which is shown as the error-bar in **Figure 6.7** (b). Thus there is a trade-off between the accuracy and the output voltage of the TEH delivery volume sensor. When the pump chamber is pressed by finger, the TEH patch will deform and contact with the Al surface. However, these two surfaces not only contact with each other but also squeeze each other and further have a friction between them. So the whole TEH does not only work in contact mode but also partially works in friction mode. The friction will also contribute to the output voltage. This friction is more obvious when the spacing is lower. This is because with the same force applied on the pump chamber, the TEH patch will squeeze the Al surface more when the spacing is lower. If the force applied onto

the pump chamber is not perpendicular to the Al surface, then a friction will occur. However, the direction of the force applied by human finger cannot be too well controlled. Thus, the extent of friction also cannot be well controlled. This is the reason why the error bar is larger when the spacing is lower. When the spacing is 1000μm, this fiction almost does not happen because the deformation of the TEH surface is not large enough to squeeze the Al surface. Based on the data when the spacing is 1000μm, the Coefficient of Variation is %CV=11%. To have a better accuracy for the delivery volume monitoring, the design of 1000 μm spacing was applied for the sample in other tests.

A demonstration of the drug delivery with volume sensor monitoring is shown in **Figure 6.7** (a). The weight of the patch was measured after each pressing to calculate the volume of the delivered solution. And the output voltages of the delivery volume sensor were also recorded and converted to delivered volume according to the voltage-volume curve calibrated in **Figure 6.6** (b). Moreover, the number of empty drug reservoirs can be counted to roughly estimate the delivered drug volume. The results of the delivery volume of each finger-pressing measured by these three methods are shown in **Figure 6.7** (c). The number of empty drug reservoirs for each pressing is 4, 2, 3, 2 and 6, which is indicated as red line in **Figure 6.7** (c). The volume measured by the weight and delivery volume sensor is indicated as blue spots and dash line, respectively. The delivered volume measured by delivery volume sensor and weight is almost the same except to the last data point, i.e., the volume measured by delivery volume sensor is a bit higher than the volume measured by weight. The applied force recorded by the delivery volume sensor at the last finger-pressing data point was higher than the required force to deliver the rest solution in the patch, where the accurate volume is characterized as weight. Secondly the delivered volume measured by counting the empty chamber does not perfectly match with the data measured by delivery

volume sensor and weight because there was some residual solution in the empty drug reservoirs and channels. Generally the delivered volume can be roughly and straightforwardly estimated by counting the number of empty drug reservoirs. Thus the triboelectric volume sensor is required to figure out relatively precise delivered volume as long as some usage scenarios need the information of accurate delivered volume.

6.2.3 Characterization and optimization for the TEH of stacked layers design

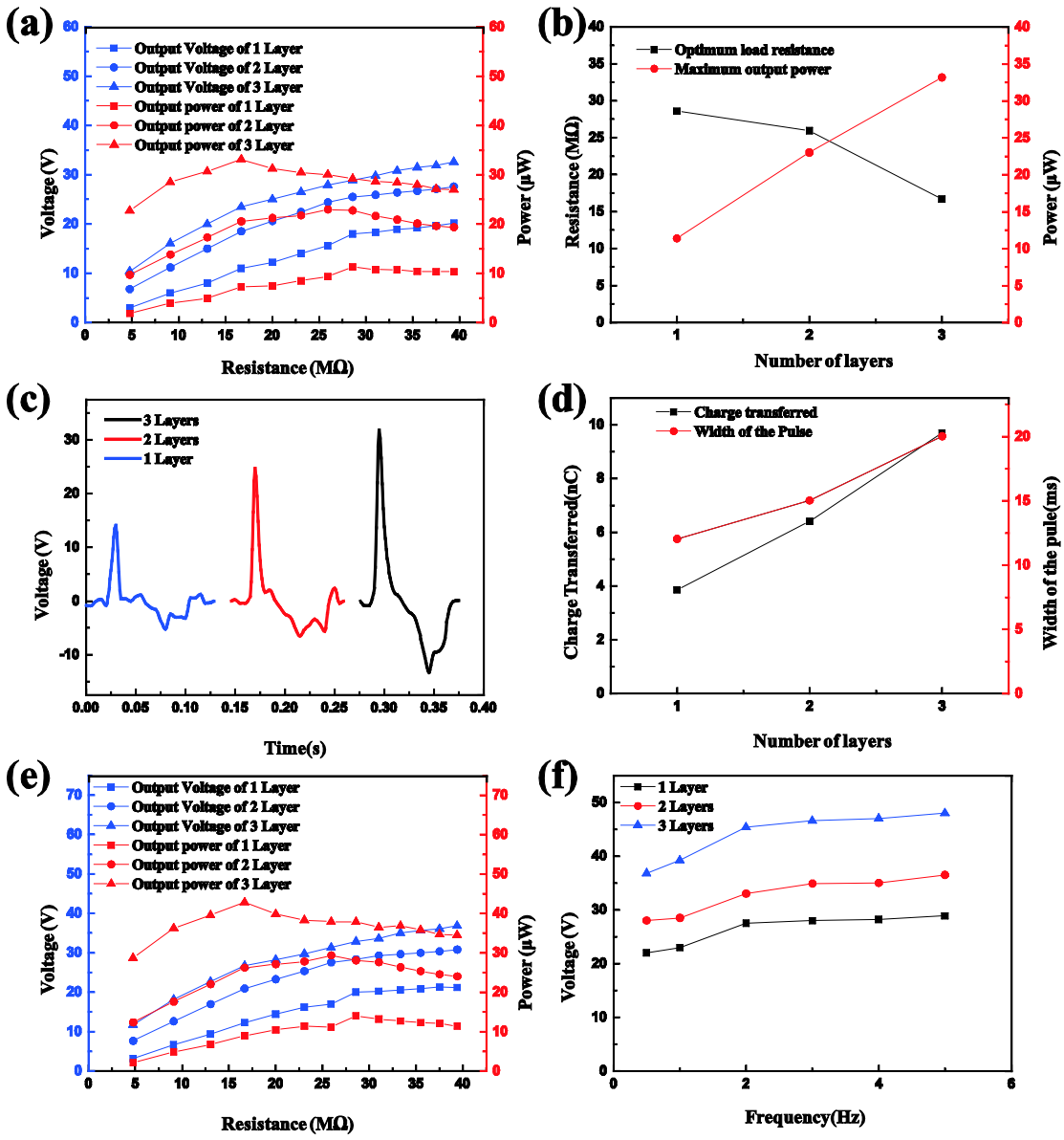

Figure 6.8 Characterization and optimization for the TEH of stacked layers design.

Due to the small area of the whole device, the power generated by a single layer of TEH is limited. Thus TEHs of stacked layer design [137-142] have been applied to enhance the output voltage. Multi-TEHs (N layers) are stacked layer by layer and connected in parallel to achieve a N-times charge transferred by one pressing comparing with the single layer TEH. If all the N-layered TEH has the charge transport simultaneously, the output voltage will increase N times. Meanwhile, due to the parallel connection of all layers in the N-layered TEH, the total inner resistance will decrease, which further enhances the output power.

Here we study the TEH with one, two and three stacked layers. The contact surface of the TEH is parylene vs Al. The thickness of PDMS dielectric layer is 215 μm which is optimized for the highest output (**Figure 6.6** (a)). And to avoid a collapse and contact between two triboelectric surfaces when pressing is not applied, the spacing between two triboelectric surfaces is 700 μm.

In order to calculate the power generated by the TEH, a load resistor was connected between the top and bottom electrodes. A cyclic force of approximately 6 N with 0.5 Hz frequency was applied to generate the power. The voltage was then measured across the load resistor to obtain the power generated by the TEH. As the load resistance was increased, the power output increased and peaked at a point and started dropping thereafter. The voltage and power characteristics of TEH with different stack layers are shown in **Figure 6.8** (a). The maximum power output for devices with one, two and three stacked layers are 11.34 μW, 22.96 μW and 33.12 μW, respectively; the load resistance are approximately 28.57 MΩ, 25.93 MΩ and 16.67 MΩ, respectively, as shown in **Figure 6.8** (b). This decrease of load resistance for peak power represents the decrease of the inner impedance of stacked TEHs, which is induced by the parallel connection of stacked TEHs. Although the quantity of charge transferred is proportional to the number of layers (black line in **Figure 6.8** (d)), the peak voltage with respect to the number of layers does not follow the same

trend. The peak voltage of TEH with 3 layers for open circuit is 33V which is not as high as 3 times of the peak voltage (15 V) of TEH with 1 layer in open circuit (**Figure 6.8** (c)). Since all the triboelectric surfaces cannot be triggered simultaneously for the TEH with more than 1 layer, the voltage pulses of different layers will be generated at different times. Thus the width of voltage pulse, which is the accumulation of the voltage pulses of all layers, will increase with the number of stacked layers (red line in **Figure 6.8** (c)). The finger-pressing frequency will also change the output voltage as shown in Fig. 5(f). As shown in this figure, the peak voltage has an obvious increase within the range from 0.5 Hz to 2 Hz and tends to saturate when frequency is higher than 2 Hz. One major parameter which seem to affect the output voltage was the impact force provided by the fingertip. As the amplitude of acceleration or force increases, the impact force also keeps increasing. Higher impact force results in increased elastic deformation in the PDMS layer which leads to increased contact area between the two triboelectric layers. The increased contact area is possibly the reason for increased triboelectric generation and performance of the device. The output voltage over time generated by different pressing frequency is added in the supplementary information. A representative example of the time domain signals of open circuit output voltage from different frequency with 1 stacked layer is shown in **Figure 6.9**. Considering that the TEH is manually pressed, 2 Hz should be a reasonable optimum operation frequency.

Due to the reliability concern , a parylene coating on the bottom PDMS dielectric layer was used to protect the metal layer at the backside in our design as shown in the S3. An experiment has been conducted for the TEHs without parylene coating as a comparison to previous data with parylene in order to characterize the impact of such parylene coating. Thus, the contact surface is PDMS vs Al. The voltage and power characteristics of TEH with different stack layers are shown in **Figure 6.8** (e). Compared with the results of TEH with parylene coating, the load resistances of

peak powers are the same. However, the peak powers are 14 μW, 29.3 μW and 42.8 μW, respectively, indicating an average of 27% enhancement. This result suggests that, if the backside metal of the TEH patch is not easily detached or scratched, the parylene layer can be avoided and PDMS surface can offer a better performance.

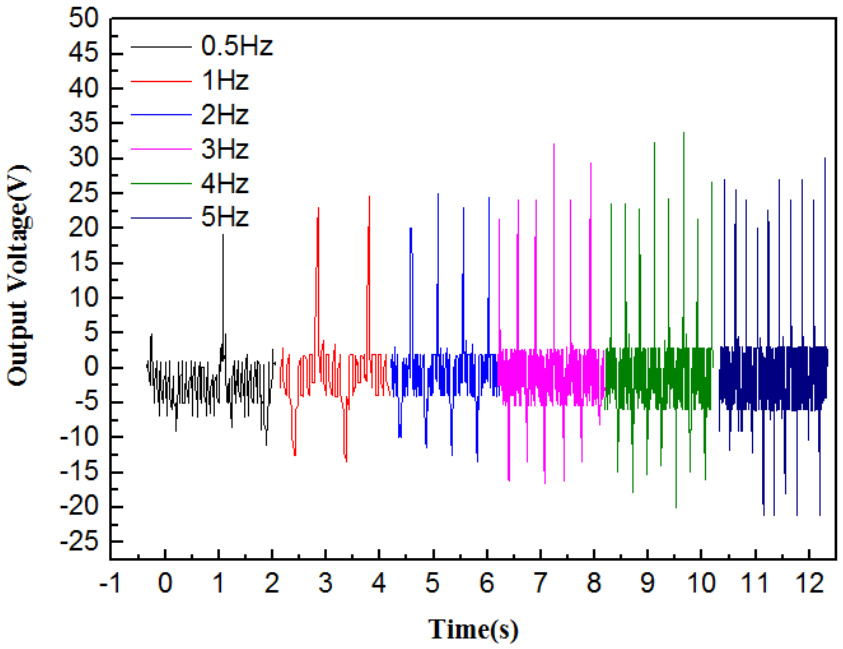

Figure 6.9 Comparison of time domain signals of open circuit output voltage from different frequency with 1 stacked layer.

The force impact increases with the increase of the pressing frequency. Thus, higher impact force results in increased elastic deformation in the PDMS layer which leads to increased contact area between the two triboelectric layers. The increased contact area induce enhances the triboelectric generation and performance of the device. When the pressing frequency is 0.5 Hz, the output voltage is around 20V. When the frequency is higher than 2 Hz, the output voltage is around 26V.

6.2.3 Characterization of the liquid volume sensor in insulin delivery test

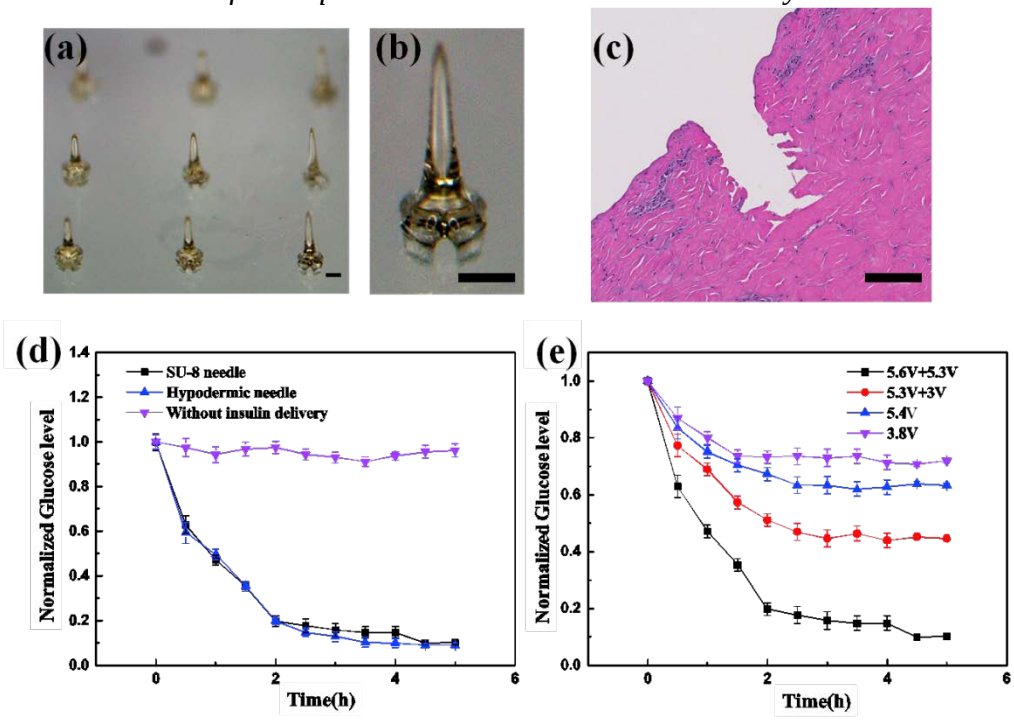

Figure 6.10 Delivery volume sensor monitors and controls the dose for insulin delivery. (a) Optical image of the microneedle array assembled onto the patch, the scale bar is 200μm; (b) Detailed optical image of an individual microneedle, the scale bar is 200μm; (c) Histology image of individual microneedle penetration, scale bar is 200μm; (d) Changes in blood glucose level in diabetic rats after insulin delivery using microneedles, subcutaneous hypodermic injection of insulin, and without injection of insulin; (e) Changes in blood glucose level in diabetic rats after insulin delivery using microneedles with different delivery volumes.

In order to confirm that the device has ideal features for an efficient drug volume control, transdermal delivery of insulin was tested in vivo. As a powerful approach for various biomedical researches such as transdermal drug delivery and transdermal bio-sensing, a microneedle array was assembled onto the skin patch for the skin penetration and insulin delivery. The sharp tips of microneedles were assembled by double drawing lithography onto the patch as shown in **Figure 6.10** (a) and (b). Penetration tests on mouse cadaver skin were conducted to characterize the penetration capability of the SU-8 microneedles made by double drawing lithography. A histology image of the skin at the site of one microneedle penetration confirms that the sharp conical tip was

not broken during the insertion steps as shown in **Figure 6.10** (c). A detailed in vitro drug delivery test is shown in **Figure 6.11**.

All the procedures were performed under protocol and approved by the Institutional Animal Care and Use Committee at the National University of Singapore. Sprague–Dawley rats with weight of 200 ~ 250 g were injected with 50 mg kg^{-1} streptozotocine (Sigma-Aldrich, Singapore) in citrate buffer (pH 4.2) via intraperitoneal injection to generate a diabetic animal model. These rats were kept with free access to food and water for 3 days. Then their blood glucose level was checked by a glucometer (Accu-Chek, USA). The rats with blood glucose level between 16 and 30 mM were selected and the hairs on the abdomen skin were removed by a razor 24 hours before the experiment. All these rats were divided into 3 groups and each group contained 3 rats.

We first conducted the tests without liquid volume control to confirm the drug delivery capability of the patch. Group 1 was a negative control group, in which we only tested the blood glucose level throughout the duration of the test. Group 2 was an experimental group. After the rats were anesthetized, the patch with insulin loaded was applied on the abdomen skin surface. The pump chamber was pressed to deliver all the insulin (10 $IUmL^{-1}$) contained in the drug reservoirs. As mentioned before, the totally volume of all the drug reservoirs is about 246 μL. In group 3, after the rats were anesthetized, 10 $IUmL^{-1}$ Lispro insulin was injected subcutaneously with a 29G hypodermic needle into the rats (2.5 $IUkg^{-1}$) as a positive control experiment.

Blood samples were taken from the tail vein every 30 minutes after the beginning of the experiments in all groups. The blood glucose level monitoring lasted for 5.5 hours. A glucometer (Accu-Chek, USA) was used to give the corresponding blood glucose levels. The results are shown in **Figure 6.10** (d). The blood glucose level in rats treated with our patch dropped continuously during the 5.5 hours insulin delivery period and was quite stable after 3 hours. It was significantly

different compared with the negative control group, where insulin solution was not administered to the rats. Remarkably, the changing of the blood glucose level in the positive control experiments in both groups, i.e., using patch and a hypodermic needle, was about the same. This experiment successfully proved the feasibility of using proposed LoC drug delivery patch to deliver macromolecules like insulin.

A detailed study was conducted in order to study the ability of manual control function for insulin delivery, which is supported by the microfluidic control system including pump chamber, check-valves and liquid volume sensor. During the test with patches, the delivery volume was controlled by controlling the pressing force. The output voltage of the liquid volume sensor was recorded to confirm the different volume delivered during the tests, as shown in **Figure 6.10** (e). There were 4 groups in the study. For the first 2 groups, only one time pressing was applied during the test. The output voltages of the delivery volume sensor were 3.8 V and 5.4 V, respectively. For the last 2 groups, the pump chambers were pressed twice and the output voltages of the delivery volume sensor were measured as 5.3+3 V and 5.6+5.3 V, respectively. The change of the blood glucose level is shown in **Figure 6.10** (e). For the group with higher voltage output, which means a larger volume of insulin delivery, the blood glucose level drops more. But for all the groups, the blood glucose level stabilized at a certain level after 3 hours. The experiment confirms that the manual control delivery mechanism with liquid volume sensor can successfully monitor insulin delivery and further control the blood glucose level. However, during the insulin delivery, the microneedles were immersed within the skin, making the outlets of the microneedles. Thus, the flow resistance of the whole microfluidic channel has a significant increase, result in a slight deviation of the actual delivery volume from the in vitro calibration as shown in **Figure 6.12**.

Generally speaking, the actual delivery volume of in vivo was around 10% lower than that of in vitro calibration in the situation of drug delivery when microneedle were in skin.

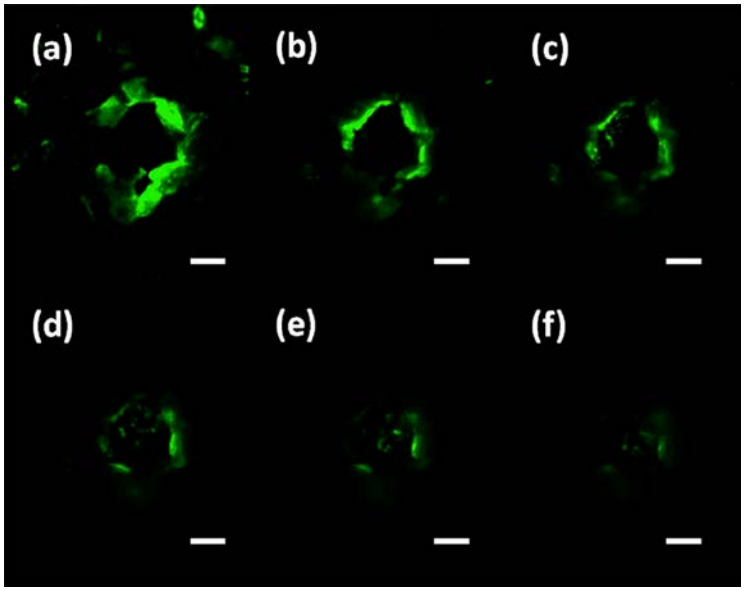

Figure 6.11 Images of confocal microscopy to show the florescent solution is successfully delivered into the tissue underneath the skin surface. (a) 30 lm; (b) 60 lm; (c) 90 lm; (d) 120 lm; (e) 150 lm; and (f) 180 lm (scale bar is 100 lm).

In order to verify that the drug solution can be delivered into tissue from the sidewall gaps of the microneedles, FITC (Fluorescein isothiocyanate) (Sigma Aldrich, Singapore) solution was delivered through the SU-8 microneedles after they were penetrated into the mouse cadaver skin. The representative results were then investigated via a confocal microscope (**Figure 6.11**). The permeation pattern of the solution along the microchannel created by microneedles confirmed the solution delivery results. The black area was a control area without any diffused florescent solution. In contrast, the illuminated area in **Figure 6.11** indicates the area where the solution has diffused to it. These images were taken consecutively from the skin surface down to 180 lm with 30 lm intervals. The diffusion area had a similar dimension with the inserted microneedles. It has proved that the device can be used to deliver drugs into the body.

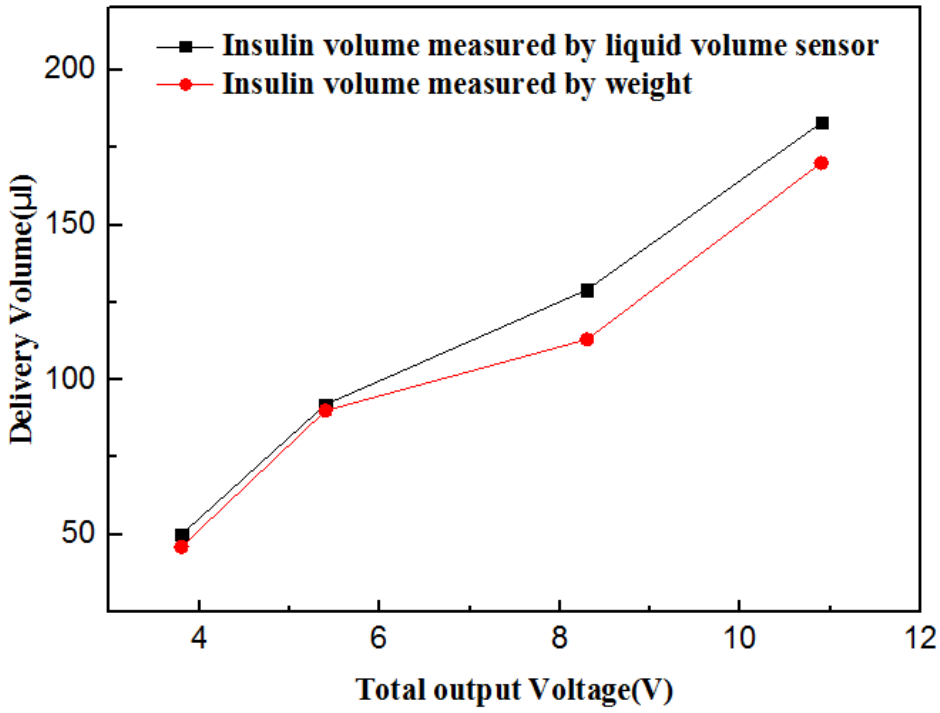

Figure 6.12 Comparison of the insulin delivery volume measured by weight and liquid volume sensor in in vivo test.

When the microneedles were in skin during *in vivo* test, the flow resistance of the whole micrfludic channel increases a lot. Thus, the actual insulin delivery volume was a bit lower than the value of the *in vitro* calibration. The detailed comparison is show in **Figure 6.12**. The actual delivery volume measured by weight (red line) is always lower than that measured by liquid volume sensor (black line). The deviation was small when the delivery volume is low and increases with the increase of the delivery volume.

6.3 Conclusion

Triboelectric energy harvester has been applied for various kinds of wearable sensors and electronics due to its flexible and thin film structure. Here a liquid volume sensor which leverages the triboelectric mechanism was integrated within a wearable lab-on-chip drug delivery patch to realize a manually controlled large volume drug delivery function. To power active components

which will be integrated on the patch in the near future, a stacked layer triboelectric energy harvester (TEH) design was studied and characterized. Increasing the number of stacked layers significantly enhances the output power. The output power generated by a TEH with 3 stacked layers and a 2×2 cm^2 area is 33 μW. The optimum pressing frequency is 2 Hz which is within the reasonable range of usage scenarios based manually finger pressing. The liquid volume sensor integrated within the patch leverages the similar structure as the TEH. The spacing between triboelectric pair surfaces is optimized to be 1000μm for a best accuracy. Thus, the delivery volume can be monitored, which is crucial for certain medical applications such as insulin delivery, whose delivery dose needs to be precisely controlled. Microneedle array was assembled onto the patch to confirm the drug delivery and volume monitoring functions by *in vivo* experiments in rats. The liquid volume sensor can be integrated with other drug delivery devices or lab-on-chip microfluidic devices when the liquid volume delivered should be accurately measured.

Chapter 7 Summary of current work and Future plan

7.1 Summary of current work

In this thesis, we have explored how to further develop the drawing lithography process and integration of microneedle with other functional components to realize different applications. We first designed and developed two different kinds of flexible microneedle patch by using dissolvable and non-dissolvable materials as the sharp tips. Both of them are hollow microneedles for the continuous delivery of large molecules. The flexible microneedle patch with dissolvable sharp tips is able to deliver drugs with large volume while four beams structure with SU-8 tips enhance the microneedle stiffness. The proposed fabrication process is scalable, reproducible and inexpensive. The height of the microneedle by drawing lithography is around 800μm which is comparative with the hollow microneedles fabricated by other processes. But our process is much simpler, of lower coat, and more importantly, enables further integration with other functional components.

Based on the non-dissolvable microneedle we developed, we further investigate the microneedle with CNTs nanofilters. Such CNTs nanofilters can be used to selectively transport biomolecules such as ss-DNA, glucose, insulin and Haemagglutinin. This is the first time to realize biomolecule transport through CNTs. Previously only gas, ion and gold particles transport through CNTs.[143-145] Because the condition to have molecules transport for different biomolecules are different, according to their dimension, shape and polarity, the drugs can be selectively delivered during the drug administration by using the microneedle with CNTs nanofilter assembled within.

For the next step, a soft microneedle skin patch which can have a conformal attachment onto skin as a wearable medical device is expected to be realized. However, the uneven skin

surface will introduce unpredictable buckling force which will cause needle breakage during the skin penetration for the soft skin patch. Therefore, we propose a unique bendable microneedle design to overcome this issue. The design composes a rigid sharp tip, which can be either glucose or SU-8, and a soft PDMS base. Such bendable microneedle can bend when the needle cannot penetrate skin. After skin penetration, the bendable microneedle can also adjust the lateral movement between skin surface and microneedle skin patch to avoid needle broken within skin. With optimization of the PDMS mix ratio and pillar angular, the skin penetration rate for bendable microneedle with SU-8 tip is 88% and with maltose tip is 66%. Although the skin penetration rate cannot be as high as rigid hollow microneedles, the bendable microneedle can avoid safety issue caused by needle breakage within skin.

By using this bendable microneedle, we realize a thin and soft microneedle skin patch as a standalone device which can realize the function of drug loading and delivery only with manual control. As a medical device, other chemical sensors for health monitoring are expected to be integrated onto the skin patch in the future. Thus a power source for these active components are necessary. In this skin patch, we also integrated TEH leveraging dry adhesive micro structure as power source which can power these sensors which may be incorporated in the future. The TEH leveraging dry adhesive micro structure can generate 11.79 μW with 23.08 MΩ inner impedance while the TEH leveraging conventional pyramid micro structure can generate 15.21 μW with 44.44 MΩ inner impedance. Although the maximum output power of pyramid is higher than that of dry adhesive, the lower inner impedance of dry adhesive can realize a higher output power when the load resistance is smaller than the inner impedance of dry adhesive.

To further make the drug delivery system complete and more like a standalone wearable medical device, a volume sensor is inevitable to measure the drug dose to be delivered, especially

for the insulin delivery. Hence we investigate a TEH based volume sensor which can be integrated within the skin patch. We delivery volume can be immediately measured when we press the finger onto the pneumatic pump to deliver drug. With this feedback signal of delivery volume, the drug dose can be manually controlled. The spacing between triboelectric pair surfaces is optimized to be 1000μm for a best accuracy when the Coefficient of Variation is %CV=11%. A minimal delivery volume of 10μL can be realized.

7.2 Flexible microneedle skin patch of ultra-high needle density with surface drug coating for short term drug delivery

For the application of short term drug delivery which only the total drug dose needs to be controlled, we could also make flexible microneedle skin patch without hollow channels but coating with a drug-containing layer onto the surface of microneedles as shown in **Figure 7.1**(a). Compared with the flexible microneedles with hollow channels, this kind of microneedle skin patch could be much thinner and more conformal to skin due to the absence of the thick PDMS layer for chamber reservoir. It could be applied as a normal bandage and will become a disposable device.

To realize a sufficient drug dose on one skin patch, the microneedle array needs to be dense enough. For the previous microneedle made by drawing lithography, the spacing of the microneedles cannot be less than 1 mm. Otherwise the drawing material will form a cluster among a few semi-formed microneedles during the drawing process. Here we propose a new idea to improve the process and overcome this issue, significantly increase the density and production quality of microneedles on one patch. Either the gel-like materials or solution-like drug will be investigated and optimized. To control the volume of the drug, the thickness of the drug coating layer could be further tuned by controlling the cycles of coating process. An improved process is

proposed in this project as shown in **Figure 7.2**. SU-8 is baked on glass slide (**Figure 7.2** (a)) and covered by a grid mold (**Figure 7.2** (b)). The holes on the grid layer would be filled by melted SU-8. Then align the microtube array (**Figure 7.2** (c)) and inserted it into the melted SU-8 (**Figure 7.2** (d)). Due to the physical separation of SU-8 in each well, during the drawing lithography process, the formation of each sharp tip will not be affected by others (**Figure 7.2** (e)). Thus the density of the needle array is simply determined by the density of the holes on grid mold.

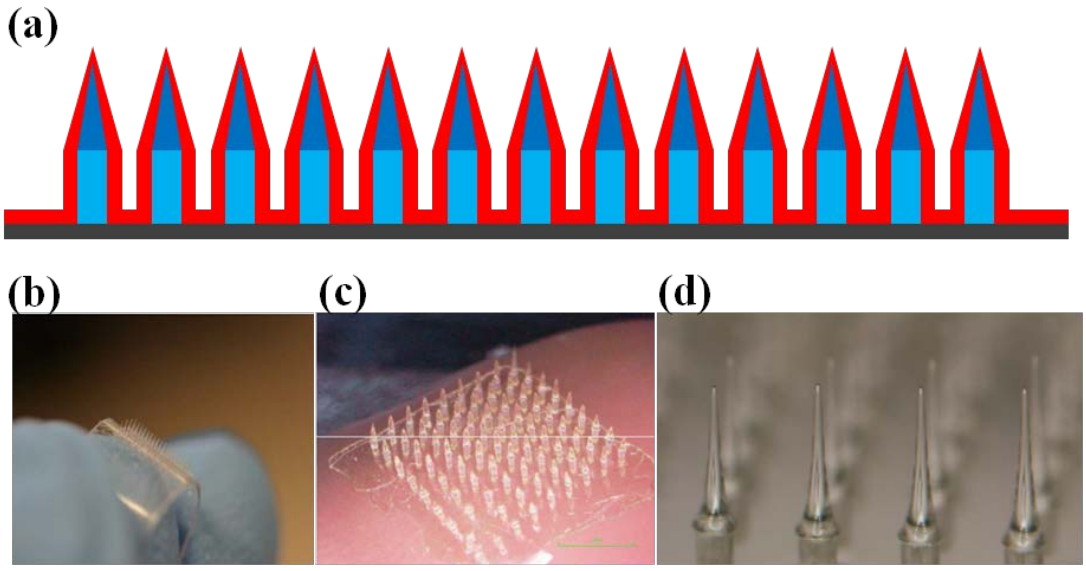

Figure 7.1 (a) 2D illustration of microneedle skin patch of ultra-high needle density with surface drug coating; (b)-(d) Optical images of a prototype of microneedle we currently achieved.

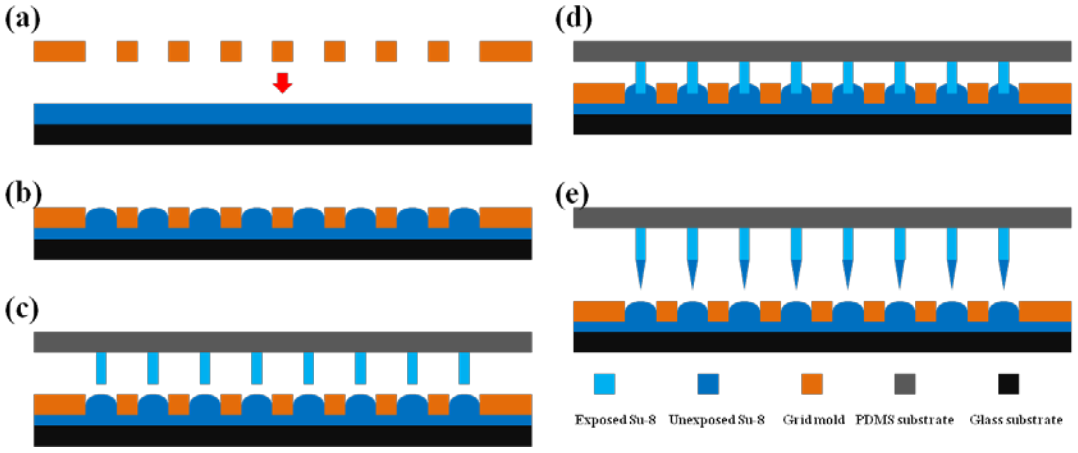

Figure 7.2 Improved drawing lithography process for ultra-high density needle array.

7.3 Further study of the selective drug delivery

A few kinds of ions and molecules pumping through CNTs by different driving methods have been reported. Gas (e.g. H_2, N_2, CO_2, Ar and CH_4), polar molecules (e.g. water, ethanol and isopropyl alcohol), non-polar molecules (e.g. hexane and decane) and non-charged nano-particles (e.g. Au particles) can pass through CNTs by applying pressures, while charged ions (e.g. Na^+, K^+, H^+ and Li^+) and various kinds of molecules (e.g. water, DNA, ss-DNA and charged lysozyme) can pass through CNTs with the aid of an electric field. But selectively transport biomolecules through CNTs nanofilters are only reported by our group. Previously, the biomolecules can pass the CNTs nanofilters just by applying electric field and pressure. However, it is also reported that surface function of CNTs could realize a selective biomolecule transport as shown in **Figure 7.3**. In **Figure 7.3** (a), the surface of CNTs was modified by electrochemically oxidation. Then two biomolecules, lysozyme and BSA, could be separated by applying electric field. Only Lysozyme could pass through the CNTs. And in **Figure 7.3** (b), the surface of CNTs was modified by ethanolamine. And the permeability of ss-DNA and Au nanopaticles could be controlled. Such a modification also could be incorporated in the fabrication of the microneedle with CNTs nanofilters.

In our future study, we could explore the other surface functionalization on CNTs nanofilters and enable a selective drug delivery without applying electric field. Thus only pressure is required, the microneedles with CNTs nanofilters are able to be integrated onto flexible skin patch as a standalone device to wearable drug delivery application.

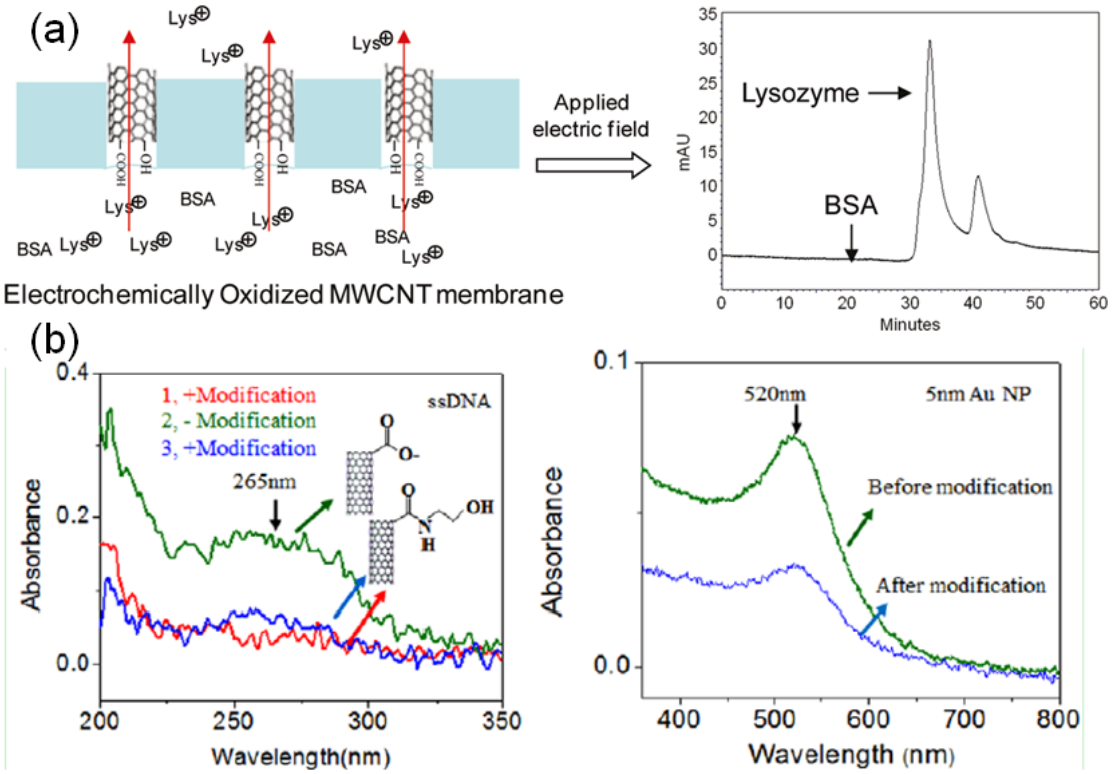

Figure 7.3 (a) The surface of CNTs is modified by electrochemical oxidization and two biomolecules could be separated by CNTs membrane; (b) The surface of CNTs is modified by ethanolamine to control the permeability of ss-DNA and Au nanoparticles.

Bibliography

[1] Singh, R., Singh, S. and Lillard, J.W., 2008. Past, present, and future technologies for oral delivery of therapeutic proteins. Journal of pharmaceutical sciences, 97(7), pp.2497-2523.

[2] Nir, Y., Paz, A., Sabo, E. and Potasman, I., 2003. Fear of injections in young adults: prevalence and associations. The American journal of tropical medicine and hygiene, 68(3), pp.341-344.

[3] Prausnitz, M.R. and Langer, R., 2008. Transdermal drug delivery. Nature biotechnology, 26(11), pp.1261-1268.

[4] Finnin, B.C. and Morgan, T.M., 1999. Transdermal penetration enhancers: applications, limitations, and potential. Journal of pharmaceutical sciences, 88(10), pp.955-958.

[5] Donnelly, R.F., Singh, T.R.R. and Woolfson, A.D., 2010. Microneedle-based drug delivery systems: microfabrication, drug delivery, and safety. Drug delivery, 17(4), pp.187-207.

[6] Sivamani, R.K., Stoeber, B., Wu, G.C., Zhai, H., Liepmann, D. and Maibach, H., 2005. Clinical microneedle injection of methyl nicotinate: stratum corneum penetration. Skin Research and Technology, 11(2), pp.152-156.

[7] Kim, Y.C., Park, J.H. and Prausnitz, M.R., 2012. Microneedles for drug and vaccine delivery. Advanced drug delivery reviews, 64(14), pp.1547-1568.

[8] van der Maaden, K., Jiskoot, W. and Bouwstra, J., 2012. Microneedle technologies for (trans) dermal drug and vaccine delivery. Journal of controlled release, 161(2), pp.645-655.

[9] Choi, C.K., Kim, J.B., Jang, E.H., Youn, Y.N. and Ryu, W.H., 2012. Curved biodegradable microneedles for vascular drug delivery. Small, 8(16), pp.2483-2488.

[10] Moon, S.J. and Lee, S.S., 2005. A novel fabrication method of a microneedle array using inclined deep x-ray exposure. Journal of Micromechanics and Microengineering, 15(5), p.903.

[11] Yoon, Y.K., Park, J.H. and Allen, M.G., 2006. Multidirectional UV lithography for complex 3-D MEMS structures. Microelectromechanical Systems, Journal of, 15(5), pp.1121-1130.

[12] Kolli, C.S. and Banga, A.K., 2008. Characterization of solid maltose microneedles and their use for transdermal delivery. Pharmaceutical research, 25(1), pp.104-113.

[13] Han, M., Lee, W., Lee, S.K. and Lee, S.S., 2004. 3D microfabrication with inclined/rotated UV lithography. Sensors and Actuators A: Physical, 111(1), pp.14-20.

[14] Sugiyama, S., Khumpuang, S. and Kawaguchi, G., 2004. Plain-pattern to cross-section transfer (PCT) technique for deep x-ray lithography and applications. Journal of Micromechanics and Microengineering, 14(10), p.1399.

[15] Lee, K.S., Kim, R.H., Yang, D.Y. and Park, S.H., 2008. Advances in 3D nano/microfabrication using two-photon initiated polymerization. Progress in Polymer Science, 33(6), pp.631-681.

[16] Han, M., Hyun, D.H., Park, H.H., Lee, S.S., Kim, C.H. and Kim, C., 2007. A novel fabrication process for out-of-plane microneedle sheets of biocompatible polymer. Journal of Micromechanics and Microengineering, 17(6), p.1184.

[17] Park, J.H., Choi, S.O., Seo, S., Choy, Y.B. and Prausnitz, M.R., 2010. A microneedle roller for transdermal drug delivery. European journal of pharmaceutics and biopharmaceutics, 76(2), pp.282-289.

[18] Choi, S.O., Kim, Y.C., Park, J.H., Hutcheson, J., Gill, H.S., Yoon, Y.K., Prausnitz, M.R. and Allen, M.G., 2010. An electrically active microneedle array for electroporation. Biomedical microdevices, 12(2), pp.263-273.

[19] Ameri, M., Fan, S.C. and Maa, Y.F., 2010. Parathyroid hormone PTH (1-34) formulation that enables uniform coating on a novel transdermal microprojection delivery system. Pharmaceutical research, 27(2), pp.303-313.

[20] Christodoulou, K.N., Kistler, S.F. and Schunk, P.R., 1997. Advances in computational methods for free-surface flows. In Liquid Film Coating (pp. 297-366). Springer Netherlands.

[21] Gill, H.S. and Prausnitz, M.R., 2007. Coated microneedles for transdermal delivery. Journal of controlled release, 117(2), pp.227-237.

[22] DeMuth, P.C., Su, X., Samuel, R.E., Hammond, P.T. and Irvine, D.J., 2010. Nano‐layered microneedles for transcutaneous delivery of polymer nanoparticles and plasmid DNA. Advanced Materials, 22(43), pp.4851-4856.

[23] Han, M., Kim, D.K., Kang, S.H., Yoon, H.R., Kim, B.Y., Lee, S.S., Kim, K.D. and Lee, H.G., 2009. Improvement in antigen-delivery using fabrication of a grooves-embedded microneedle array. Sensors and Actuators B: Chemical, 137(1), pp.274-280.

[24] Gill, H.S. and Prausnitz, M.R., 2008. Pocketed microneedles for drug delivery to the skin. Journal of Physics and Chemistry of Solids, 69(5), pp.1537-1541.

[25] Raphael, A.P., Prow, T.W., Crichton, M.L., Chen, X., Fernando, G.J. and Kendall, M.A., 2010. Targeted, Needle‐Free Vaccinations in Skin using Multilayered, Densely‐Packed Dissolving Microprojection Arrays. Small, 6(16), pp.1785-1793.

[26] Ito, Y., Hagiwara, E., Saeki, A., Sugioka, N. and Takada, K., 2007. Sustained-release self-dissolving micropiles for percutaneous absorption of insulin in mice. Journal of drug targeting, 15(5), pp.323-326.

[27] Sullivan, S.P., Murthy, N. and Prausnitz, M.R., 2008. Minimally invasive protein delivery with rapidly dissolving polymer microneedles. Advanced materials, 20(5), pp.933-938.

[28] Park, J.H., Allen, M.G. and Prausnitz, M.R., 2006. Polymer microneedles for controlled-release drug delivery. Pharmaceutical research, 23(5), pp.1008-1019.

[29] You, X., Chang, J.H., Ju, B.K. and Pak, J.J., 2011. Rapidly dissolving fibroin microneedles for transdermal drug delivery. Materials Science and Engineering: C, 31(8), pp.1632-1636.

[30] Park, J.H., Choi, S.O., Kamath, R., Yoon, Y.K., Allen, M.G. and Prausnitz, M.R., 2007. Polymer particle-based micromolding to fabricate novel microstructures. Biomedical microdevices, 9(2), pp.223-234.

[31] Fukushima, K., Ise, A., Morita, H., Hasegawa, R., Ito, Y., Sugioka, N. and Takada, K., 2011. Two-layered dissolving microneedles for percutaneous delivery of peptide/protein drugs in rats. Pharmaceutical research, 28(1), pp.7-21.

[32] Chu, L.Y., Choi, S.O. and Prausnitz, M.R., 2010. Fabrication of dissolving polymer microneedles for controlled drug encapsulation and delivery: bubble and pedestal microneedle designs. Journal of pharmaceutical sciences, 99(10), pp.4228-4238.

[33] Lee, J.W., Park, J.H. and Prausnitz, M.R., 2008. Dissolving microneedles for transdermal drug delivery. Biomaterials, 29(13), pp.2113-2124.

[34] Sullivan, S.P., Koutsonanos, D.G., del Pilar Martin, M., Lee, J.W., Zarnitsyn, V., Choi, S.O., Murthy, N., Compans, R.W., Skountzou, I. and Prausnitz, M.R., 2010. Dissolving polymer microneedle patches for influenza vaccination. Nature medicine, 16(8), pp.915-920.

[35] Chu, L.Y. and Prausnitz, M.R., 2011. Separable arrowhead microneedles. Journal of controlled release, 149(3), pp.242-249.

[36] Wonglertnirant, N., Todo, H., Opanasopit, P., Ngawhirunpat, T. and Sugibayashi, K., 2010. Macromolecular delivery into skin using a hollow microneedle. Biological and Pharmaceutical Bulletin, 33(12), pp.1988-1993.

[37] Davis, S.P., Martanto, W., Allen, M.G. and Prausnitz, M.R., 2005. Hollow metal microneedles for insulin delivery to diabetic rats. Biomedical Engineering, IEEE Transactions on, 52(5), pp.909-915.

[38] Burton, S.A., Ng, C.Y., Simmers, R., Moeckly, C., Brandwein, D., Gilbert, T., Johnson, N., Brown, K., Alston, T., Prochnow, G. and Siebenaler, K., 2011. Rapid intradermal delivery of liquid formulations using a hollow microstructured array. Pharmaceutical research, 28(1), pp.31-40.

[39] Yung, K.L., Xu, Y., Kang, C., Liu, H., Tam, K.F., Ko, S.M., Kwan, F.Y. and Lee, T.M., 2011. Sharp tipped plastic hollow microneedle array by microinjection moulding. Journal of Micromechanics and Microengineering, 22(1), p.015016.

[40] Perennes, F., Marmiroli, B., Matteucci, M., Tormen, M., Vaccari, L. and Di Fabrizio, E., 2006. Sharp beveled tip hollow microneedle arrays fabricated by LIGA and 3D soft lithography with polyvinyl alcohol. Journal of Micromechanics and Microengineering, 16(3), p.473.

[41] Ceyssens, F., Chaudhri, B.P., Van Hoof, C. and Puers, R., 2013. Fabrication process for tall, sharp, hollow, high aspect ratio polymer microneedles on a platform. Journal of Micromechanics and Microengineering, 23(7), p.075023.

[42] Gittard, S.D., Miller, P.R., Boehm, R.D., Ovsianikov, A., Chichkov, B.N., Heiser, J., Gordon, J., Monteiro-Riviere, N.A. and Narayan, R.J., 2011. Multiphoton microscopy of transdermal quantum dot delivery using two photon polymerization-fabricated polymer microneedles. Faraday discussions, 149, pp.171-185.

[43] Roxhed, N., Gasser, T.C., Griss, P., Holzapfel, G.A. and Stemme, G., 2007. Penetration-enhanced ultrasharp microneedles and prediction on skin interaction for efficient transdermal drug delivery. Microelectromechanical Systems, Journal of, 16(6), pp.1429-1440.

[44] Ma, B., Liu, S., Gan, Z., Liu, G., Cai, X., Zhang, H. and Yang, Z., 2006. A PZT insulin pump integrated with a silicon microneedle array for transdermal drug delivery. Microfluidics and Nanofluidics, 2(5), pp.417-423.

[45] Daugimont, L., Baron, N., Vandermeulen, G., Pavselj, N., Miklavcic, D., Jullien, M.C., Cabodevila, G., Mir, L.M. and Préat, V., 2010. Hollow microneedle arrays for intradermal drug delivery and DNA electroporation. The Journal of membrane biology, 236(1), pp.117-125.

[46]Miller, P.R., Gittard, S.D., Edwards, T.L., Lopez, D.M., Xiao, X., Wheeler, D.R., Monteiro-Riviere, N.A., Brozik, S.M., Polsky, R. and Narayan, R.J., 2011. Integrated carbon fiber electrodes within hollow polymer microneedles for transdermal electrochemical sensing. Biomicrofluidics, 5(1), p.013415.

[47] Moon, S.J., Lee, S.S., Lee, H.S. and Kwon, T.H., 2005. Fabrication of microneedle array using LIGA and hot embossing process. Microsystem technologies, 11(4-5), pp.311-318.

[48] Gittard, S.D., Ovsianikov, A., Chichkov, B.N., Doraiswamy, A. and Narayan, R.J., 2010. Two-photon polymerization of microneedles for transdermal drug delivery. Expert opinion on drug delivery, 7(4), pp.513-533.

[49] Lee, K., Lee, C.Y. and Jung, H., 2011. Dissolving microneedles for transdermal drug administration prepared by stepwise controlled drawing of maltose. Biomaterials, 32(11), pp.3134-3140.

[50] Lee, K. and Jung, H., 2012. Drawing lithography for microneedles: a review of fundamentals and biomedical applications. Biomaterials, 33(30), pp.7309-7326.

[51] Blanco, F.J., Agirregabiria, M., Garcia, J., Berganzo, J., Tijero, M., Arroyo, M.T., Ruano, J.M., Aramburu, I. and Mayora, K., 2004. Novel three-dimensional embedded SU-8 microchannels fabricated using a low temperature full wafer adhesive bonding. Journal of Micromechanics and Microengineering, 14(7), p.1047.

[52] "Bernhard Tollens (1841-1918) and some American students of his school of agricultural chemistry." Journal of Chemical Education 19, no. 6 (1942): 253.

[53] Hong, C., Bao, D., Thomas, M.S., Clift, J.M. and Vullev, V.I., 2008. Print-and-peel fabrication of microelectrodes. Langmuir, 24(16), pp.8439-8442.

[54] Zhang, J., Tan, K.L. and Gong, H.Q., 2001. Characterization of the polymerization of SU-8 photoresist and its applications in micro-electro-mechanical systems (MEMS). Polymer testing, 20(6), pp.693-701.

[55] Townrow, S., Kilburn, D., Alam, A. and Ubbink, J., 2007. Molecular packing in amorphous carbohydrate matrixes. The Journal of Physical Chemistry B, 111(44), pp.12643-12648.

[56] Kiverin, M.D., 1957. Maltase in the skin. Biohimija, 22, pp.617-621.

[57] Tromp, R., Dusschoten, D. and Ring, S., 1999. Carbon-13 nuclear magnetic relaxation in supercooled liquid and glassy maltose. Physical Chemistry Chemical Physics, 1(8), pp.1927-1931.

[58] Gunning, Y.M., Parker, R. and Ring, S.G., 2000. Diffusion of short chain alcohols from amorphous maltose–water mixtures above and below their glass transition temperature. Carbohydrate research, 329(2), pp.377-385.

[59] Schwartz, R.A., 1995. Cutaneous metastatic disease. Journal of the American Academy of Dermatology, 33(2), pp.161-185.

[60] Brown, M.B., Martin, G.P., Jones, S.A. and Akomeah, F.K., 2006. Dermal and transdermal drug delivery systems: current and future prospects. Drug delivery, 13(3), pp.175-187.

[61] Qin, G., Gao, Y., Wu, Y., Zhang, S., Qiu, Y., Li, F. and Xu, B., 2012. Simultaneous basal-bolus delivery of fast-acting insulin and its significance in diabetes management. Nanomedicine: Nanotechnology, Biology and Medicine, 8(2), pp.221-227.

[62] Fernández, L.J., Altuna, A., Tijero, M., Gabriel, G., Villa, R., Rodríguez, M.J., Batlle, M., Vilares, R., Berganzo, J. and Blanco, F.J., 2009. Study of functional viability of SU-8-based microneedles for neural applications. Journal of Micromechanics and Microengineering, 19(2), p.025007.

[63] Lee, K. and Jung, H., 2012. Drawing lithography for microneedles: a review of fundamentals and biomedical applications. Biomaterials, 33(30), pp.7309-7326.

[64] Olatunji, O., Das, D.B., Garland, M.J., Belaid, L.U.C. and Donnelly, R.F., 2013. Influence of array interspacing on the force required for successful microneedle skin penetration: theoretical and practical approaches. Journal of pharmaceutical sciences, 102(4), pp.1209-1221.

[65] Krishnakumar, P., Tiwari, P.B., Staples, S., Luo, T., Darici, Y., He, J. and Lindsay, S.M., 2012. Mass transport through vertically aligned large diameter MWCNTs embedded in parylene. Nanotechnology, 23(45), p.455101.

[66] Su, J. and Guo, H., 2010. Control of unidirectional transport of single-file water molecules through carbon nanotubes in an electric field. ACS nano, 5(1), pp.351-359.

[67] Mansoor, I., Liu, Y., Häfeli, U.O. and Stoeber, B., 2013. Arrays of hollow out-of-plane microneedles made by metal electrodeposition onto solvent cast conductive polymer structures. Journal of Micromechanics and Microengineering, 23(8), p.085011.

[68] Roxhed, N., Gasser, T.C., Griss, P., Holzapfel, G.A. and Stemme, G., 2007. Penetration-enhanced ultrasharp microneedles and prediction on skin interaction for efficient transdermal drug delivery. Microelectromechanical Systems, Journal of, 16(6), pp.1429-1440.

[69] McAllister, D.V., Wang, P.M., Davis, S.P., Park, J.H., Canatella, P.J., Allen, M.G. and Prausnitz, M.R., 2003. Microfabricated needles for transdermal delivery of macromolecules and nanoparticles: fabrication methods and transport studies. Proceedings of the National Academy of Sciences, 100(24), pp.13755-13760.

[70] Glucose detection kit data sheet, from http://www.abcam.com/glucose-detection-kit-ab102517.html

[71] Wilke, N., Mulcahy, A., Ye, S.R. and Morrissey, A., 2005. Process optimization and characterization of silicon microneedles fabricated by wet etch technology. Microelectronics Journal, 36(7), pp.650-656.

[72] Shorten, P.R., McMahon, C.D. and Soboleva, T.K., 2007. Insulin transport within skeletal muscle transverse tubule networks. Biophysical journal, 93(9), pp.3001-3007.

[73] Böttcher, C., Ludwig, K., Herrmann, A., van Heel, M. and Stark, H., 1999. Structure of influenza haemagglutinin at neutral and at fusogenic pH by electron cryo-microscopy. FEBS letters, 463(3), pp.255-259.

[74] Wang, H., Xiang, Z., Hu, C.F., Pant, A., Fang, W., Alonso, S., Pastorin, G. and Lee, C., 2013. Development of stretchable membrane based nanofilters using patterned arrays of vertically grown carbon nanotubes. Nanoscale, 5(18), pp.8488-8493.

[75] Jin, C.Y., Han, M.H., Lee, S.S. and Choi, Y.H., 2009. Mass producible and biocompatible microneedle patch and functional verification of its usefulness for transdermal drug delivery. Biomedical microdevices, 11(6), pp.1195-1203.

[76] Wilke, N. and Morrissey, A., 2006. Silicon microneedle formation using modified mask designs based on convex corner undercut. Journal of micromechanics and microengineering, 17(2), p.238.

[77] Gill, H.S. and Prausnitz, M.R., 2007. Coated microneedles for transdermal delivery. Journal of controlled release, 117(2), pp.227-237.

[78] Jara, A.J., Zamora, M.A. and Skarmeta, A.F., 2011. An internet of things---based personal device for diabetes therapy management in ambient assisted living (AAL). Personal and Ubiquitous Computing, 15(4), pp.431-440.

[79] Park, J.H., Choi, S.O., Kamath, R., Yoon, Y.K., Allen, M.G. and Prausnitz, M.R., 2007. Polymer particle-based micromolding to fabricate novel microstructures. Biomedical microdevices, 9(2), pp.223-234.

[80] Gill, H.S. and Prausnitz, M.R., 2007. Coated microneedles for transdermal delivery. Journal of controlled release, 117(2), pp.227-237.

[81] Kim, Y.C., Quan, F.S., Compans, R.W., Kang, S.M. and Prausnitz, M.R., 2010. Formulation and coating of microneedles with inactivated influenza virus to improve vaccine stability and immunogenicity. Journal of controlled release, 142(2), pp.187-195.

[82] Wilke, N., Mulcahy, A., Ye, S.R. and Morrissey, A., 2005. Process optimization and characterization of silicon microneedles fabricated by wet etch technology. Microelectronics Journal, 36(7), pp.650-656.

[83] Wilke, N. and Morrissey, A., 2006. Silicon microneedle formation using modified mask designs based on convex corner undercut. Journal of micromechanics and microengineering, 17(2), p.238.

[84] Geim, A.K., Dubonos, S.V., Grigorieva, I.V., Novoselov, K.S., Zhukov, A.A. and Shapoval, S.Y., 2003. Microfabricated adhesive mimicking gecko foot-hair. Nature materials, 2(7), pp.461-463.

[85] Arzt, E., Gorb, S. and Spolenak, R., 2003. From micro to nano contacts in biological attachment devices. Proceedings of the National Academy of Sciences, 100(19), pp.10603-10606.

[86] Porter, C.J., Trevaskis, N.L. and Charman, W.N., 2007. Lipids and lipid-based formulations: optimizing the oral delivery of lipophilic drugs. Nature Reviews Drug Discovery, 6(3), pp.231-248.

[87] Govender, T., Stolnik, S., Garnett, M.C., Illum, L. and Davis, S.S., 1999. PLGA nanoparticles prepared by nanoprecipitation: drug loading and release studies of a water soluble drug. Journal of Controlled Release, 57(2), pp.171-185.

[88] Jeong, C.K., Park, K.I., Son, J.H., Hwang, G.T., Lee, S.H., Park, D.Y., Lee, H.E., Lee, H.K., Byun, M. and Lee, K.J., 2014. Self-powered fully-flexible light-emitting system enabled by flexible energy harvester. Energy & Environmental Science, 7(12), pp.4035-4043.

[89] Lee, T.I., Jang, W.S., Lee, E., Kim, Y.S., Wang, Z.L., Baik, H.K. and Myoung, J.M., 2014. Ultrathin self-powered artificial skin. Energy & Environmental Science, 7(12), pp.3994-3999.

[90] Lee, G., Kim, D., Kim, D., Oh, S., Yun, J., Kim, J., Lee, S.S. and Ha, J.S., 2015. Fabrication of a stretchable and patchable array of high performance micro-supercapacitors using a non-aqueous solvent based gel electrolyte. Energy & Environmental Science, 8(6), pp.1764-1774.

[91] Hwang, G.T., Kim, Y., Lee, J.H., Oh, S., Jeong, C.K., Park, D.Y., Ryu, J., Kwon, H., Lee, S.G., Joung, B. and Kim, D., 2015. Self-powered deep brain stimulation via a flexible PIMNT energy harvester. Energy & Environmental Science, 8(9), pp.2677-2684.

[92] Webb, R.C., Pielak, R.M., Bastien, P., Ayers, J., Niittynen, J., Kurniawan, J., Manco, M., Lin, A., Cho, N.H., Malyrchuk, V. and Balooch, G., 2015. Thermal transport characteristics of human skin measured in vivo using ultrathin conformal arrays of thermal sensors and actuators. PloS one, 10(2), p.e0118131.

[93] Tao, H., Hwang, S.W., Marelli, B., An, B., Moreau, J.E., Yang, M., Brenckle, M.A., Kim, S., Kaplan, D.L., Rogers, J.A. and Omenetto, F.G., 2014. Silk-based resorbable electronic devices for remotely controlled therapy and in vivo infection abatement. Proceedings of the National Academy of Sciences, 111(49), pp.17385-17389.

[94] Gao, L., Zhang, Y., Malyarchuk, V., Jia, L., Jang, K.I., Webb, R.C., Fu, H., Shi, Y., Zhou, G., Shi, L. and Shah, D., 2014. Epidermal photonic devices for quantitative imaging of temperature and thermal transport characteristics of the skin. Nature communications, 5.

[95] Escabí, M.A., Read, H.L., Viventi, J., Kim, D.H., Higgins, N.C., Storace, D.A., Liu, A.S., Gifford, A.M., Burke, J.F., Campisi, M. and Kim, Y.S., 2014. A high-density, high-channel count, multiplexed μECoG array for auditory-cortex recordings. Journal of neurophysiology, 112(6), pp.1566-1583.

[96] Yu, C., Li, Y., Zhang, X., Huang, X., Malyarchuk, V., Wang, S., Shi, Y., Gao, L., Su, Y., Zhang, Y. and Xu, H., 2014. Adaptive optoelectronic camouflage systems with designs inspired by cephalopod skins. Proceedings of the National Academy of Sciences, 111(36), pp.12998-13003.

[97] Hwang, S.W., Song, J.K., Huang, X., Cheng, H., Kang, S.K., Kim, B.H., Kim, J.H., Yu, S., Huang, Y. and Rogers, J.A., 2014. High‐Performance Biodegradable/Transient Electronics on Biodegradable Polymers. Advanced Materials, 26(23), pp.3905-3911.

[98] Atzori, L., Iera, A. and Morabito, G., 2010. The internet of things: A survey. Computer networks, 54(15), pp.2787-2805.

[99] Jara, A.J., Zamora, M.A. and Skarmeta, A.F., 2011. An internet of things---based personal device for diabetes therapy management in ambient assisted living (AAL). Personal and Ubiquitous Computing, 15(4), pp.431-440.

[100] Chin, C.D., Linder, V. and Sia, S.K., 2007. Lab-on-a-chip devices for global health: Past studies and future opportunities. Lab on a Chip, 7(1), pp.41-57.

[101] Arzt, E., Gorb, S. and Spolenak, R., 2003. From micro to nano contacts in biological attachment devices. Proceedings of the National Academy of Sciences, 100(19), pp.10603-10606.

[102] Geim, A.K., Dubonos, S.V., Grigorieva, I.V., Novoselov, K.S., Zhukov, A.A. and Shapoval, S.Y., 2003. Microfabricated adhesive mimicking gecko foot-hair. Nature materials, 2(7), pp.461-463.

[103] Gupta, J., Felner, E.I. and Prausnitz, M.R., 2009. Minimally invasive insulin delivery in subjects with type 1 diabetes using hollow microneedles. Diabetes technology & therapeutics, 11(6), pp.329-337.

[104] Ito, Y., Hagiwara, E., Saeki, A., Sugioka, N. and Takada, K., 2006. Feasibility of microneedles for percutaneous absorption of insulin. European journal of pharmaceutical sciences, 29(1), pp.82-88.

[105] Martanto, W., Davis, S.P., Holiday, N.R., Wang, J., Gill, H.S. and Prausnitz, M.R., 2004. Transdermal delivery of insulin using microneedles in vivo. Pharmaceutical research, 21(6), pp.947-952.

[106] Davis, S.P., Martanto, W., Allen, M.G. and Prausnitz, M.R., 2005. Hollow metal microneedles for insulin delivery to diabetic rats. Biomedical Engineering, IEEE Transactions on, 52(5), pp.909-915.

[107] Huang, X., Liu, Y., Cheng, H., Shin, W.J., Fan, J.A., Liu, Z., Lu, C.J., Kong, G.W., Chen, K., Patnaik, D. and Lee, S.H., 2014. Materials and designs for wireless epidermal sensors of hydration and strain. Advanced Functional Materials, 24(25), pp.3846-3854.

[108] Suh, K.Y., Jeon, N.L. and Pang, C., 2013, April. Wearable skin sensor using programmable interlocking of nanofibers. In Nano/Micro Engineered and Molecular Systems (NEMS), 2013 8th IEEE International Conference on (pp. 132-135). IEEE.

[109] Strambini, L.M., Longo, A., Scarano, S., Prescimone, T., Palchetti, I., Minunni, M., Giannessi, D. and Barillaro, G., 2015. Self-powered microneedle-based biosensors for pain-free high-accuracy measurement of glycaemia in interstitial fluid. Biosensors and Bioelectronics, 66, pp.162-168.

[110] Yoon, Y., Lee, G.S., Yoo, K. and Lee, J.B., 2013. Fabrication of a microneedle/CNT hierarchical micro/nano surface electrochemical sensor and its in-vitro glucose sensing characterization. Sensors, 13(12), pp.16672-16681.

[111] Windmiller, J.R., Zhou, N., Chuang, M.C., Valdés-Ramírez, G., Santhosh, P., Miller, P.R., Narayan, R. and Wang, J., 2011. Microneedle array-based carbon paste amperometric sensors and biosensors. Analyst, 136(9), pp.1846-1851.

[112] Miller, P.R., Skoog, S.A., Edwards, T.L., Lopez, D.M., Wheeler, D.R., Arango, D.C., Xiao, X., Brozik, S.M., Wang, J., Polsky, R. and Narayan, R.J., 2012. Multiplexed microneedle-based biosensor array for characterization of metabolic acidosis. Talanta, 88, pp.739-742.

[113] Xiang, Z., Wang, H., Pastorin, G. and Lee, C., 2015. Development of a Flexible and Disposable Microneedle-Fluidic-System With Finger-Driven Drug Loading and Delivery Functions for Inflammation Treatment. Microelectromechanical Systems, Journal of, 24(3), pp.565-574.

[114] Lin, Z.H., Zhu, G., Zhou, Y.S., Yang, Y., Bai, P., Chen, J. and Wang, Z.L., 2013. A Self‐Powered Triboelectric Nanosensor for Mercury Ion Detection. Angewandte Chemie International Edition, 52(19), pp.5065-5069.

[115] Lin, Z.H., Cheng, G., Wu, W., Pradel, K.C. and Wang, Z.L., 2014. Dual-mode triboelectric nanogenerator for harvesting water energy and as a self-powered ethanol nanosensor. ACS nano, 8(6), pp.6440-6448.

[116] Wang, Z.L., 2013. Triboelectric nanogenerators as new energy technology for self-powered systems and as active mechanical and chemical sensors. ACS nano, 7(11), pp.9533-9557.

[117] Pan, C., Li, Z., Guo, W., Zhu, J. and Wang, Z.L., 2011. Fiber‐Based Hybrid Nanogenerators for/as Self‐Powered Systems in Biological Liquid. Angewandte Chemie International Edition, 50(47), pp.11192-11196.

[118] Lin, L., Xie, Y., Wang, S., Wu, W., Niu, S., Wen, X. and Wang, Z.L., 2013. Triboelectric active sensor array for self-powered static and dynamic pressure detection and tactile imaging. ACS nano, 7(9), pp.8266-8274.

[119] Niu, S., Wang, S., Lin, L., Liu, Y., Zhou, Y.S., Hu, Y. and Wang, Z.L., 2013. Theoretical study of contact-mode triboelectric nanogenerators as an effective power source. Energy & Environmental Science, 6(12), pp.3576-3583.

[120] Xiang, Z., Wang, H., Pant, A., Pastorin, G. and Lee, C., 2013. Development of vertical SU-8 microtubes integrated with dissolvable tips for transdermal drug delivery. Biomicrofluidics, 7(2), p.026502.

[121] Xiang, Z., Wang, H., Pant, A., Pastorin, G. and Lee, C., 2013. Development of vertical SU-8 microneedles for transdermal drug delivery by double drawing lithography technology. Biomicrofluidics, 7(6), p.066501.

[122] Zhang, H., Yang, Y., Su, Y., Chen, J., Hu, C., Wu, Z., Liu, Y., Wong, C.P., Bando, Y. and Wang, Z.L., 2013. Triboelectric nanogenerator as self-powered active sensors for detecting liquid/gaseous water/ethanol. Nano Energy, 2(5), pp.693-701.

[123] Lin, Z.H., Zhu, G., Zhou, Y.S., Yang, Y., Bai, P., Chen, J. and Wang, Z.L., 2013. A Self‐Powered Triboelectric Nanosensor for Mercury Ion Detection. Angewandte Chemie International Edition, 52(19), pp.5065-5069.

[124] Lin, Z.H., Cheng, G., Wu, W., Pradel, K.C. and Wang, Z.L., 2014. Dual-mode triboelectric nanogenerator for harvesting water energy and as a self-powered ethanol nanosensor. ACS nano, 8(6), pp.6440-6448.

[125] Wang, Z.L., 2013. Triboelectric nanogenerators as new energy technology for self-powered systems and as active mechanical and chemical sensors. ACS nano, 7(11), pp.9533-9557.

[126] Pan, C., Li, Z., Guo, W., Zhu, J. and Wang, Z.L., 2011. Fiber‐Based Hybrid Nanogenerators for/as Self‐Powered Systems in Biological Liquid. Angewandte Chemie International Edition, 50(47), pp.11192-11196.

[127] Lin, L., Xie, Y., Wang, S., Wu, W., Niu, S., Wen, X. and Wang, Z.L., 2013. Triboelectric active sensor array for self-powered static and dynamic pressure detection and tactile imaging. ACS nano, 7(9), pp.8266-8274.

[128] Fan, F.R., Lin, L., Zhu, G., Wu, W., Zhang, R. and Wang, Z.L., 2012. Transparent triboelectric nanogenerators and self-powered pressure sensors based on micropatterned plastic films. Nano letters, 12(6), pp.3109-3114.

[129] Li, Y., Cheng, G., Lin, Z.H., Yang, J., Lin, L. and Wang, Z.L., 2015. Single-electrode-based rotationary triboelectric nanogenerator and its applications as self-powered contact area and eccentric angle sensors. Nano Energy, 11, pp.323-332.

[130] Han, C.B., Zhang, C., Li, X.H., Zhang, L., Zhou, T., Hu, W. and Wang, Z.L., 2014. Self-powered velocity and trajectory tracking sensor array made of planar triboelectric nanogenerator pixels. Nano Energy, 9, pp.325-333.

[131] Han, M., Zhang, X.S., Sun, X., Meng, B., Liu, W. and Zhang, H., 2014. Magnetic-assisted triboelectric nanogenerators as self-powered visualized omnidirectional tilt sensing system. Scientific reports, 4.

[132] Chen, J., Zhu, G., Yang, W., Jing, Q., Bai, P., Yang, Y., Hou, T.C. and Wang, Z.L., 2013. Harmonic‐Resonator‐Based Triboelectric Nanogenerator as a Sustainable Power Source and a Self‐Powered Active Vibration Sensor. Advanced Materials, 25(42), pp.6094-6099.

[133] Yang, Y., Zhang, H., Chen, J., Jing, Q., Zhou, Y.S., Wen, X. and Wang, Z.L., 2013. Single-electrode-based sliding triboelectric nanogenerator for self-powered displacement vector sensor system. Acs Nano, 7(8), pp.7342-7351.

[134] Su, Y., Zhu, G., Yang, W., Yang, J., Chen, J., Jing, Q., Wu, Z., Jiang, Y. and Wang, Z.L., 2014. Triboelectric sensor for self-powered tracking of object motion inside tubing. ACS nano, 8(4), pp.3843-3850.

[135] Yang, Y., Zhu, G., Zhang, H., Chen, J., Zhong, X., Lin, Z.H., Su, Y., Bai, P., Wen, X. and Wang, Z.L., 2013. Triboelectric nanogenerator for harvesting wind energy and as self-powered wind vector sensor system. Acs Nano, 7(10), pp.9461-9468.

[136] Meng, B., Tang, W., Too, Z.H., Zhang, X., Han, M., Liu, W. and Zhang, H., 2013. A transparent single-friction-surface triboelectric generator and self-powered touch sensor. Energy Environ. Sci., 6(11), pp.3235-3240.

[137] Zhu, G., Yang, W.Q., Zhang, T., Jing, Q., Chen, J., Zhou, Y.S., Bai, P. and Wang, Z.L., 2014. Self-powered, ultrasensitive, flexible tactile sensors based on contact electrification. Nano letters, 14(6), pp.3208-3213.

[138] Yang, Y., Zhang, H., Lin, Z.H., Zhou, Y.S., Jing, Q., Su, Y., Yang, J., Chen, J., Hu, C. and Wang, Z.L., 2013. Human skin based triboelectric nanogenerators for harvesting biomechanical energy and as self-powered active tactile sensor system. Acs Nano, 7(10), pp.9213-9222.

[139] Kanik, M., Say, M.G., Daglar, B., Yavuz, A.F., Dolas, M.H., El‐Ashry, M.M. and Bayindir, M., 2015. A Motion‐and Sound‐Activated, 3D‐Printed, Chalcogenide‐Based Triboelectric Nanogenerator. Advanced Materials, 27(14), pp.2367-2376.

[140] Ko, Y.H., Nagaraju, G. and Yu, J.S., 2015. Multi-stacked PDMS-based triboelectric generators with conductive textile for efficient energy harvesting. RSC Advances, 5(9), pp.6437-6442.

[141] Cheng, G., Zheng, L., Lin, Z.H., Yang, J., Du, Z. and Wang, Z.L., 2015. Multilayered‐Electrode‐Based Triboelectric Nanogenerators with Managed Output Voltage and Multifold Enhanced Charge Transport. Advanced Energy Materials, 5(5).

[142] Yang, P.K., Lin, Z.H., Pradel, K.C., Lin, L., Li, X., Wen, X., He, J.H. and Wang, Z.L., 2015. Paper-Based Origami Triboelectric Nanogenerators and Self-Powered Pressure Sensors. ACS nano, 9(1), pp.901-907.

[143] Cormier, M., & Daddona, P. E. (2003). Macroflux technology for transdermal delivery of therapeutic proteins and vaccines. Drugs and the Pharmaceutical Sciences, 126, 589-598.

[144] Davis, S. P., Landis, B. J., Adams, Z. H., Allen, M. G., & Prausnitz, M. R. (2004). Insertion of microneedles into skin: measurement and prediction of insertion force and needle fracture force. Journal of biomechanics, 37(8), 1155-1163.

Appendix 1 : Detailed fabrication process for CNT nanofilter

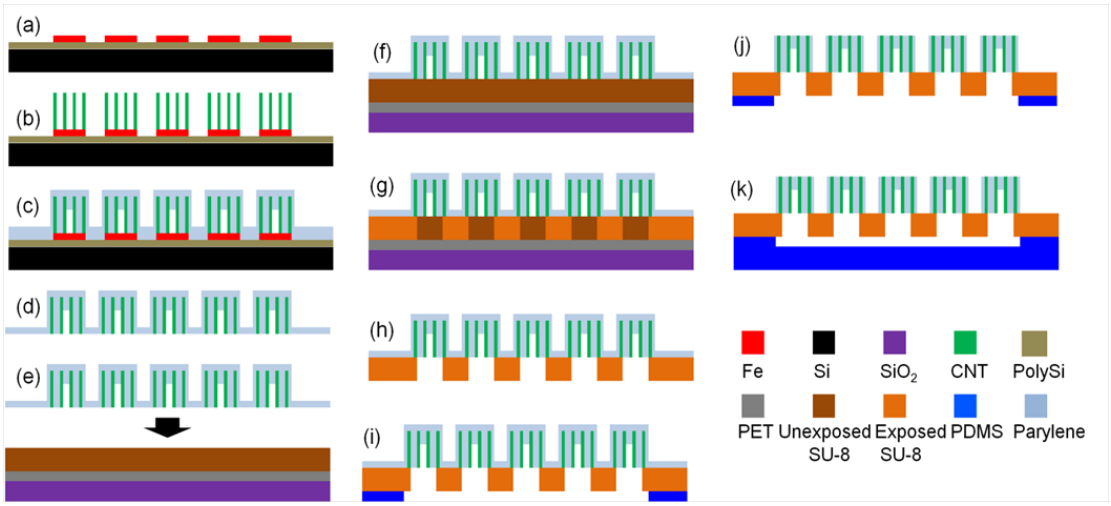

Figure A1. Fabrication process for stretchable membrane based nanofilters using patterned array of vertically grown carbon nanotubes

Figure A1 illustrates the fabrication process. The process began with thermal oxidation of single crystal silicon substrate to form a etch stop oxide layer. After the CVD of poly-silicon as a sacrificial layer, a 5 nm thickness of pattered Fe film, which acted as the catalyst film for the selective growth of CNTs, was prepared onto the silicon substrate (Figure A1(a)). As illustrated in Figure A1(b), the vertical aligned CNT bundles of 50 μm in height were grown via pyrolysis of acetylene at 800ºC with an Ar/NH3 flow for 15 min. The CVD parylene-C was then employed to fill into vertically aligned CNTs to reinforce the inter-tube binding at room temperature. Thus, the top side of CNTs was covered with parylene-C, and the discrete CNTs were bound together by parylene-C (Figure A1(c)). This step was the most critical process for forming the mechanical supporting layer for CNT bundles. The thickness of the flexible parylene-C layer was determined

by the CVD process. To achieve reliable mechanical strength for following handling and process, 10 μm thick parylene layer was deployed. The parylene layer was peeled off together with CNT bundles from the substrate. Since the catalyst layer blocked the bottom ends of CNTs, the catalyst layer at the bottom of CNT bundles was etched by oxygen plasma from backside (Figure A1(d)). Then a prebaked SU-8 layer of 200 μm thickness on PET was prepared. PET is a kind of transparent soft film having low adhesion with SU-8. The PET film was fixed on glass slide by tapes to provide a rigid substrate for processing. The parylene layer was attached on the surface of SU-8 layer. The SU-8 layer was then melted at 95 ºC and cooled to room temperature. A good bonding between parylene and SU-8 was achieved (Figure A1(e) and 1(f)). After this bonding, well aligned microchannels under CNT bundles were patterned by UV lithography (Figure A1(g)). The diameter of the channel is 40 μm, smaller than the diameter of the CNT bundles, to ensure the SU-8 under parylene sidewalls around CNT bundles was exposed. The bonding between SU-8 and parylene sidewalls would finally provide sufficient mechanical bonding strength to fix the CNT membranes on SU-8 substrate. After UV lithography, the sample was post baked at 65 ºC for 10 min and 95 ºC for 30 min. Then the PET film together with SU-8 and parylene layer was released from glass slide by removing the tapes. The SU-8 layer together with the parylene layer was dry released from PET by slightly bending the PET film (Figure A1(h)). The released SU-8 layer was developed to form the microchannels. A bonding technique was developed for bond SU-8 with PDMS. A thin PDMS film of 200 μm thickness with center area larger than the dimension of CNT bundle array cut off was prepared. The surface of this PDMS layer was treated with nitrogen plasma and attached to the bottom surface of SU-8 layer. The sample was baked at 120 ºC for 30 min. A permanent bonding between SU-8 and PDMS was achieved (Figure A1(i)). In this step, the thickness of PDMS must be kept low enough to avoid the poor quality bonding, which is due to

the non-conductivity and the low plasma efficiency of the PDMS layer. After the bonding, the parylene layer was etched by oxygen plasma to open the sealed top ends (Figure A1(j)). In this process, the whole parylene layer was etched away except the parylene sidewall around the CNT bundles due to the anisotropic property of RIE . The adhesion between parylene and SU-8 was good enough to hold suspended CNT bundles as mentioned above. In the RIE etching process, the plasma generated large amount of heat. The temperature of SU-8 layer would rise to several hundred ºC during the long period of the 10 μm thick parylene etching. This high temperature would degenerate the bonding between SU-8 and PDMS. Thus, the whole etching process was divided into several periods to avoid over heating for samples. After etching away parylene on CNT bundles, the membrane was bonded with a thick PDMS layer (Figure A1(k)). This process is a conventional bonding between PDMS surfaces. Both PMDS surfaces were treated with oxygen plasma and bonded together. This thick PDMS layer allows us to connect tubes for further fluidic tests.

Appendix 2 : Preparation of ss-DNA and BPSM

ss-DNA preparation: Single strand DNA (ss-DNA) was prepared by the following steps: Bordetella pertussis genomic DNA was used as a template to synthesize a PCR fragment of 805 base pair using Go Taq Green Master Mix (Promega) kit protocol. Primers used for the PCR were from Sigma Aldrich, HPLC purified vipC forward primer (5'TTGAATTCGAGTTCGAGCCGGTGCTGG3') and vipC reverse primer (5'TTAAGCTTTTGCTGGTAAGGAATGCGCTG3'). Annealing temperature of 64.5ºC was used and the denaturation, annealing and extension cycle was repeated 25 times. Final elongation step was carried out at 72ºC for 10 min. The ds-DNA generated was then kept at 95ºC for 5 min to separate the two DNA strands to generate ss-DNA. PCR reaction was set up using Bio-Rad iCycler-thermal cycler PCR. Haemagglutinin was purchased from Zuellig Pharma. Other chemical reagents were purchased from Sigma Aldrich and used without a further purification. NaCl and HCl solutions were prepared using deionized (DI) water from a water purification system (Millipore SAS 67120 MOISHEIM).

Bacterial preparation: BPSM (Bordetella pertussis streptomycin resistant strain) was grown on sheep blood agar plates for 4 days. A loopful growth was taken to inoculate 10 ml SSAB media with streptomycin. The culture was grown for 24 hours at 37 ºC with continuous shaking. The OD (optical density) was measured and adjusted to 1×107 cfu/mL bacteria in PBS.

Appendix 3 : List of Publication and Award

Journal Paper

1. **Hao Wang**, Giorgia Pastorin, and Chengkuo Lee, " Stretchable Self-powered Wearable Adhesive Skin Patch with Bendable Microneedle Array for Transdermal Drug Delivery", submitted to Advanced Science.

2. **Hao Wang**, Zhuolin Xiang, Giorgia Pastorin, Xiaojing Mu, Zhong Lin Wang, Lee Chengkuo, "Development of triboelectric liquid volume sensor for self-powered lab-on-chip applications", Nano Energy (Under review)

3. **Hao Wang**, Chia-Hung Chen, Zhuolin Xiang, Min Wang and Chengkuo Lee, "Convection-driven long-range linear gradient generator with dynamic controls", Lab on a Chip, vol. 15, no. 6, pp 1445 - 1450, 2015.

4. **Hao Wang**, Zhuolin Xiang, Chih-Fan Hu, Giorgia Pastorin, Weileun Fang, and Chengkuo Lee, "Microneedle Array Integrated with CNT Nanofilters for Controlled and Selective Drug Delivery", IEEE/ASME J. Microelectromech. Syst., vol.23, No.5, pp. 1036-1044, 2014

5. **Hao Wang**, Zhuolin Xiang, Chih-Fan Hu, Aakanksha Pant, Weileun Fang, Sylvie Alonso, Giorgia Pastorin and Chengkuo Lee, "Development of stretchable membrane based nanofilters using patterned arrays of vertically grown carbon nanotubes" , Nanoscale, vol. 5, no. 18, pp. 8488-8493, 2013

6. Zhuolin Xiang, **Hao Wang**, Aakanksha Pant, Giorgia Pastorin, and Chengkuo Lee, "Development of vertical SU-8 microtubes integrated with dissolvable tips for transdermal drug delivery" , Biomicrofluidics, vol. 7, no. 2, 026502, 2013.

7. Zhuolin Xiang, **Hao Wang**, Giorgia Pastorin and Chengkuo Lee, "Development of a Flexible and Disposable Microneedle-Fluidic-System With Finger-Driven Drug Loading and Delivery Functions for Inflammation Treatment", IEEE/ASME J. Microelectromech. Syst., vol. 24, no.3, pp. 565-574, 2015.

8. Zhuolin Xiang, **Hao Wang**, Suresh Murugappan, Shih-Cheng Yen, Giorgia Pastorin, and Chengkuo Lee, "Dense vertical SU-8 microneedles drawn from heated mold with precisely controlled volume", J. Micromech. Microeng, vol. 25, no. 2, pp. 025013, 2015

9. Zhuolin Xiang, **Hao Wang**, Aakanksha Pant, Giorgia Pastorin, and Chengkuo Lee, "Development of vertical SU-8 microneedles for transdermal drug delivery by double drawing lithography technology", Biomicrofluidics, vol. 7, no. 6, 066501, 2013.

Conference Paper

1. Tao Wang, **Hao Wang** and Chengkuo Lee,"Highly Sensitive Piezoelectric Micromachined Ultrasonic Transducer (pMUT) Operated in Air",The 11th Annual IEEE Int'l Conference on Nano/Micro Engineered & Molecular Systems, Matsushima Bay & Sendai, Japan from 17-20 April, 2016

2. **Hao Wang**, Tao Wang and Chengkuo Lee,"Self-Powered Liquid Volume Sensor Aiming at Lab-on-Chip Applications", The 11th Annual IEEE Int'l Conference on Nano/Micro Engineered & Molecular Systems, Matsushima Bay & Sendai, Japan from 17-20 April, 2016

3. **Hao Wang**, Chia-Hung Chen, Zhuolin Xiang and Chengkuo Lee, Dynamic Controlled Long-Range Convection Flow-Driven Gradient In Lab-On-Chip , The 5th International Conference on Optofluidics 2015 , Taipei, Taiwan, July 26~29, 2015.

4. Zhuolin Xiang, **Hao Wang** and Chengkuo Lee, A Disposable Drug Delivery System with Dense Vertical Microneedles Array and Finger-Driven Drug Loading and Delivery Functions, The 7th Intern. Symposium on Microchemistry and Microsystems (ISMM 2015), Kyoto, Japan,June 8-10, 2015.

5. Zhuolin Xiang, **Hao Wang**, Giorgia Pastorin, and Chengkuo Lee, Development Of A Disposable And Flexible Microneedle-Fluidic-System With Finger Driven Drug Loading And Delivery Functions, The 18th Intern. Conf. on Solid-State Sensors, Actuators and Microsystems (Transducers 2015), M4C.007, pp.89-92, Anchorage, Alaska, June 21-25, 2015.

6. **Hao Wang**, Yan Wang, Zhuolin Xiang, Ming Wang, Chia-Hung Chen and Chengkuo Lee, Chemical Gradient Generator By Using Diffusion And Convection, The 6th International Symposium on Microchemistry and Microsystems (ISMM 2014), pp. 232-233, Singapore, Jul. 29 Aug. 1, 2014.

7. **Hao Wang**, Zhuolin Xiang, Chih-Fan Hu, Giorgia Pastorin, Weileun Fang and Chengkuo Lee, Microneedle Integrated with CNT for Controlled and Selective Drug Delivery, The 6th International Symposium on Microchemistry and Microsystems (ISMM 2014), pp. 95-96, Singapore, Jul. 29 Aug. 1, 2014.

8. **Hao Wang**, Zhuolin Xiang, Chih-Fan Hu, Giorgia Pastorin, Askanksha Pant, Weileun Fang and Chengkuo Lee, Microneedle Array Integrated with Nanofilter for Selective Drug Delivery, Intern. Conf. on BioElectronics, BioSensor, BioMedical Devices, BioMEMS/NEMS and Applications 2013 (Bio4Apps 2013) &5th Sensing Biology Symposium,INV-2F-7 (Invited), Tokyo Medical and Dental University, Tokyo, Japan, Oct. 30-31, 2013.

9. **Hao Wang**, Zhuolin Xiang, Chih-Fan Hu, Aakanksha Pant, Weileun Fang, Giorgia Pastorin and Chengkuo Lee, Polymer Microneedle Array Integrated with CNT Nanofilter for Selective Drug Delivery, The 15th International Conference on Biomedical Engineering (ICMBE 2013),IFMBE Proceedings 43,pp. 872-875,Springer, Singapore, Dec

4-7, 2013.

10. **Hao Wang**, Zhuolin Xiang, Aakanksha Pant, Giorgia Pastorin, and Chengkuo Lee, Feasibility of Flexible Patch-Like Transdermal Drug Delivery Devices, the 2nd Japan-Singapore Research Exchange & ICT Farm Project, Kyushu University, Japan, Aug. 16-17, 2013.

11. Zhuolin Xiang, **Hao Wang**, Chengkuo Lee, Aakanksha Pant, Pastorin Giorgia, Integration of Dissolvable Sharp Maltose tips on SU-8 Microtubes for Transdermal Drug Delivery Application, The 5th International Symposium on Microchemistry and Microsystems (ISMM 2013), Xiamen University, China, 1-K-1, May 16-19, 2013.

12. **Hao Wang**, Zhuolin Xiang, Chih-Fan Hu, Aakanksha Pant, Giorgia Pastorin, Weileun Fang, Sylvie Alonso, and Chengkuo Lee, Stretchable Nanofilter Membrane Using Patterned Array of Vertically Grown Carbon Nanotubes, The 5th International Symposium on Microchemistry and Microsystems (ISMM 2013), Xiamen University, China, P-I-49, May 16-19, 2013. (poster)

13. Venkata Sudheer Makam, **Wang Hao**,Chengkuo Lee, and Giorgia Pastorin, Label free isolation of sample mixtures containing tumor cells and blood cells using a microfluidic device, The 5th International Symposium on Microchemistry and Microsystems (ISMM 2013), Xiamen University, China, P-I-55, May 16-19, 2013.

14. Zhuolin Xiang, **Hao Wang**, Songsong Zhang, Shih-Cheng Yen, Minkyu Je, Wei Mong Tsang, Yong-Ping Xu, Nitish V. Thakor, Dim-Lee Kwong, and Chengkuo Lee, Development of Flexible Neural Probes Using SU-8/Parylene, The 18th Annual IEEE International Conference on Nano/Micro Engineered and Molecular Systems (NEMS 2013), Suzhou, China, 1076 - 1079, Apr. 7-10, 2013.

15. Zhuolin Xiang, **Hao Wang**, Songsong Zhang, Minkyu Je, Wei Mong Tsang, Yong-Ping Xu, Shih-Cheng Yen, Nitish V. Thakor, and Chengkuo Lee, Development of polymer-based electrode probes for neural interfacing, Intern. Conf. on BioElectronics, BioSensor, BioMedical Devices, BioMEMS/NEMS and Applications 2012 (Bio4Apps 2012), PP-13, CeLS, National University of Singapore, Singapore, Nov. 19-20, 2012.

16. Zhuolin Xiang, **Hao Wang**, Chengkuo Lee, Aakansha Pant, and Giorgia Pastorin, Development of SU-8 microneedles integrated with dissolvable tips for transdermal drug delivery, International Conference on BioElectronics, BioSensor, BioMedical Devices, BioMEMS/NEMS and Applications 2012 (Bio4Apps 2012), PP-14, CeLS, National University of Singapore, Singapore, Nov. 19-20, 2012.

17. **Hao Wang**, Zhuolin Xiang, Chih-Fan Hu, Chengkuo Lee, Aakansha Pant, Weileun Fang, and Giorgia Pastorin, Development of patterned vertically grown carbon nanotubes filters for mass transportation, Intern. Conf. on BioElectronics, BioSensor, BioMedical Devices, BioMEMS/NEMS and Applications 2012 (Bio4Apps 2012), PP-15, CeLS, National University of Singapore, Singapore, Nov. 19-20, 2012.

Award

Best Paper Award recipients for 6th International Symposium on Microchemistry & Microsystems (ISMM) 2014
Hao Wang
Oral Paper Award
The winning entry is entitled "*Microneedle Array Integrated with CNT Filters for Controlled and Selective Transdermal Drug Delivery*".